

Local and Bulk Measurements in Novel Magnetically Frustrated Materials

Eric Michael Kenney II

A dissertation

submitted to the Faculty of

the Department of Physics

in partial fulfillment

of the requirements for the degree of

Doctor of Philosophy

Boston College
Morrissey College of Arts and Sciences
Graduate School

July 12th, 2022

Local and Bulk Measurements in Novel Magnetically Frustrated Materials

Eric Michael Kenney II

Advisor: Michael J. Graf, Ph.D.

Abstract

Quantum spin liquids (QSL)'s have been one of the most hotly researched areas of condensed matter physics for the past decade. Yet, science has yet to unconditionally identify any one system as harboring a QSL state. This is because QSL's are largely defined as systems whose electronic spins do not undergo a thermodynamic transition as $T \rightarrow 0$. Quantum spin liquids remain fully paramagnetic, including dynamical spin fluctuations, at $T=0$. As a result, distinguishing a QSL system from a conventionally disordered system remains an outstanding challenge.

If a system spin freezes or magnetically orders, it cannot be a QSL. In this thesis I present published experiments I have performed on QSL candidate materials. By using muon spin rotation (μ SR) and AC magnetic susceptibility I have evaluated the ground states of several candidates for the absence of long-range magnetic order and low-temperature spin-fluctuations. For the systems which order or spin-freeze, my research provided key knowledge to the field of frustrated magnetism.

The systems I studied are as follows: The geometrically frustrated systems NaYbO_2 and LiYbO_2 ; the Kitaev honeycomb systems Cu_2IrO_3 and $\text{Ag}_3\text{LiIr}_2\text{O}_6$; and the metallic kagome system KV_3Sb_5 . Each of these systems brought new physics to the field of frustrated magnetism. NaYbO_2 is a promising QSL candidate. LiYbO_2 harbors an usual form of spiral incommensurate order that has a staggered transition. Cu_2IrO_3 has charge state disorder that results in a magnetically inhomogeneous state. $\text{Ag}_3\text{LiIr}_2\text{O}_6$ illustrates the role structural disorder plays in disguising long-range magnetic order. And finally, KV_3Sb_5 isn't conventionally magnetic at all; our measurements ruled out ionic magnetism and uncovered a type-II superconductor. Our measurements on KV_3Sb_5 stimulated further research into KV_3Sb_5 and its unconventional electronic states.

Contents

1	Introduction	1
1.1	Outline of Thesis	1
1.2	References	3
2	Quantum Spin Liquids and Magnetic Frustration	5
2.1	Introduction	5
2.2	What is a Quantum Spin Liquid?	5
2.2.1	A Very Brief History of the Notion	6
2.2.2	But Really, What is a Quantum Spin Liquid?	7
2.3	The $N = 3$ Ising Triangle	9
2.4	Elementary Theories of Quantum Spin Liquids	18
2.4.1	Kitaev honeycomb Model	19
2.4.2	Observables and Predictions of the Kitaev QSL	23
2.4.3	Anderson RVB— $U(1)$ and \mathbb{Z}_2 Spin Liquids	25
2.4.4	Observables and Predictions of the RVB Model	30
2.5	Example Materials	31
2.6	Conclusions	33
2.7	Recommended Reading	34
2.8	References	35
2.9	Figures	39
3	μSR Technique	45
3.1	Introduction	45

3.2	Polarization Functions	50
3.3	Dynamics	59
3.4	Usage of μ SR in Quantum Spin Liquid research	62
3.5	Bibliography	63
3.6	Figures	64
4	Frustrated Magnetism in NaYbO_2 and LiYbO_2	69
4.1	Introduction	70
4.2	NaYbO_2	71
4.2.1	Characterization NaYbO_2	71
4.2.2	Experimental NaYbO_2	72
4.2.3	Results NaYbO_2	73
4.2.4	Discussion NaYbO_2	74
4.2.5	Theory NaYbO_2	75
4.2.6	Conclusions NaYbO_2	76
4.3	LiYbO_2	77
4.3.1	Characterization LiYbO_2	77
4.3.2	Experimental LiYbO_2	79
4.3.3	Results LiYbO_2	79
4.3.4	Discussion LiYbO_2	82
4.3.5	Model of μ SR in LiYbO_2	84
4.3.6	Persistent and Sporadic Dynamics in μ SR and LiYbO_2	87
4.4	Conclusions	89
4.5	References	90
4.6	Figures	95
5	Frustrated Magnetism in Cu_2IrO_3 and $\text{Ag}_3\text{LiIr}_2\text{O}_6$	111
5.1	Introduction	112
5.2	Cu_2IrO_3	113
5.2.1	Characterization Cu_2IrO_3	113
5.2.2	Experimental Cu_2IrO_3	115

5.2.3	Results Cu_2IrO_3	116
5.2.4	Discussion Cu_2IrO_3	118
5.3	$\text{Ag}_3\text{LiIr}_2\text{O}_6$	120
5.3.1	Characterization $\text{Ag}_3\text{LiIr}_2\text{O}_6$	120
5.3.2	Experimental $\text{Ag}_3\text{LiIr}_2\text{O}_6$	121
5.3.3	Results $\text{Ag}_3\text{LiIr}_2\text{O}_6$	122
5.3.4	Discussion $\text{Ag}_3\text{LiIr}_2\text{O}_6$	123
5.4	Conclusions	125
5.5	References	126
5.6	Figures	130
6	The Kagome Metal KV_3Sb_5: Novel Electronic States Disguised as Frustrated Magnetism	139
6.1	Introduction	139
6.2	Characterization	141
6.3	Experimental - μSR	142
6.4	Results - μSR Measurements	143
6.5	Results - μSR Calculations	144
6.6	Experimental –AC Susceptibility	147
6.7	Results – AC Susceptibility	148
6.8	Discussion	149
6.9	Conclusions	152
6.10	References	153
6.11	figures	157
7	Conclusions	163

List of Figures

2-1	Illustration of a geometric frustration for the triangular lattice	39
2-2	Example of degenerate ground-states in a triangular system	39
2-3	Illustration of the frustrated spin triangle's topology	40
2-4	Visual representation of the Kitaev honeycomb model	40
2-5	Two possible geometries of a TM-O-TM bonds for the quantum compass model	41
2-6	Examples of the structural units formed by 90° TM-O-TM bonds	41
2-7	Graphical representation of the Kitaev Model Hamiltonian	42
2-8	Theoretical thermodynamic properties of the isotropic Kitaev model	43
2-9	A graphical representation of the RVB dimer state	44
2-10	Graphical illustrations of the Kitaev ground state	44
3-1	Angular distribution of the muon decay	64
3-2	Diagram of the muon stopping process	65
3-3	Diagram of a basic μ SR setup	66
3-4	Example μ SR spectra	67
3-5	Larmor precession of the muon	68
3-6	Field dependence of the static tail under longitudinal fields	68
4-1	Crystallographic structure of NaYbO ₂	95
4-2	Neutron diffraction and inelastic scattering data for NaYbO ₂	96
4-3	High temperature bulk magnetic susceptibility and specific heat data for NaYbO ₂	97

4-4	Low temperature bulk magnetic susceptibility and specific heat data for NaYbO ₂	98
4-5	Theoretical phase diagram of the generalized nearest-neighbor spin-1/2 triangular lattice	99
4-6	Theoretical phase diagram of the anisotropic XXZ model on the triangular lattice	100
4-7	Structure of LiYbO ₂	101
4-8	Specific Heat $C(T)$ of LiYbO ₂	101
4-9	Neutron powder diffraction data for LiYbO ₂	102
4-10	Low energy inelastic neutron scattering spectra $S(Q , \hbar\omega)$ for LiYbO ₂	103
4-11	Bulk Magnetic susceptibility and magnetization for LiYbO ₂	104
4-12	Zero-field μ SR data for LiYbO ₂	105
4-13	Longitudinal-field μ SR data for LiYbO ₂	106
4-14	High-temperature μ SR data for LiYbO ₂	107
4-15	Proposed phase diagram of LiYbO ₂	108
4-16	Analysis of the J_0^2 field distribution for LiYbO ₂	109
4-17	Longitudinal field response of the J_0^2 model for LiYbO ₂	110
5-1	Structure of Cu ₂ IrO ₃	130
5-2	STEM images of Cu ₂ IrO ₃ layers	131
5-3	μ SR fit results of Cu ₂ IrO ₃	132
5-4	Electron diffraction and HAADF-STEM images of Ag ₃ LiIr ₂ O ₆	133
5-5	Short time asymmetry spectra for Ag ₃ LiIr ₂ O ₆	134
5-6	μ SR fit parameters and data for Ag ₃ LiIr ₂ O ₆	135
5-7	ALIO Longitudinal Field μ SR data	136
5-8	Specific heat C/T of ALIO	137
6-1	Crystal structure of KV ₃ Sb ₅	157
6-2	μ SR polarization spectra for KV ₃ Sb ₅	158
6-3	Temperature dependence of the Gaussian depolarization rate for KV ₃ Sb ₅	158
6-4	Bulk electronic measurements of KV ₃ Sb ₅	159

6-5	Diagrammatic representation of the orbital dipoles and local magnetic field in the kagome planes of CsV_3Sb_5	160
6-6	μSR -based phase diagram for CsV_3Sb_5	161
6-7	The normalized gaussian depolarization rate of polycrystal KV_3Sb_5 .	162

Acknowledgments

I would like to thank my thesis advisor, Prof. Michael J. Graf for the infinite patience and support he has given me over the years. The guidance, support, and opportunities he has given me is what ultimately allowed me to finish this thesis. Thank you.

I would also like to thank my mother for her unwavering support. You went far above and beyond what was expected for a mother. Thank you.

To Nancy, Sile, and Scott for all the help you provided over the years. And to Jane Carter, for her understanding and helpfulness. All of you kept the department running over the years.

To my friends in the graduate department: Thank you for making BC a fun and wonderful place to work.

And to all the rest of the professors, from Prof. Bakshi to Prof. Herczyński, I would like to thank you for all the mentoring, support, and classes you gave to all of us.

List of Publications

- [1] **E. M. Kenney**, M. M. Bordelon, C. Wang, H. Luetkens, S. D. Wilson, and M. J. Graf, “Novel magnetic ordering in LiYbO_2 probed by muon spin relaxation,” Apr. 29, 2022. arXiv: 2205.00052 [cond-mat].
- [2] F. Bahrami*, **E. M. Kenney***, C. Wang, *et al.*, “Effect of structural disorder on the Kitaev magnet $\text{Ag}_3\text{LiIr}_2\text{O}_6$,” *Physical Review B*, vol. 103, no. 9, p. 094427, Mar. 17, 2021. DOI: 10.1103/PhysRevB.103.094427.
- [3] M. M. Bordelon, C. Liu, L. Posthuma, *et al.*, “Frustrated Heisenberg $J_1 - J_2$ model within the stretched diamond lattice of LiYbO_2 ,” *Physical Review B*, vol. 103, no. 1, p. 014420, Jan. 14, 2021. DOI: 10.1103/PhysRevB.103.014420.
- [4] **E. M. Kenney**, B. R. Ortiz, C. Wang, S. D. Wilson, and M. J. Graf, “Absence of local moments in the kagome metal kv_3sb_5 as determined by muon spin spectroscopy,” *Journal of Physics: Condensed Matter*, vol. 33, no. 23, p. 235801, Jun. 9, 2021. DOI: 10.1088/1361-648X/abe8f9.
- [5] B. R. Ortiz, P. M. Sarte, E. M. Kenney, *et al.*, “Superconductivity in the \mathbb{Z}_2 kagome metal KV_3Sb_5 ,” *Physical Review Materials*, vol. 5, no. 3, p. 034801, Mar. 2, 2021. DOI: 10.1103/PhysRevMaterials.5.034801.
- [6] M. M. Bordelon, **E. Kenney**, C. Liu, *et al.*, “Field-tunable quantum disordered ground state in the triangular-lattice antiferromagnet NaYbO_2 ,” *Nature Physics*, vol. 15, no. 10, pp. 1058–1064, Oct. 2019. DOI: 10.1038/s41567-019-0594-5.
- [7] **E. M. Kenney**, C. U. Segre, W. Lafargue-Dit-Hauret, *et al.*, “Coexistence of static and dynamic magnetism in the Kitaev spin liquid material Cu_2IrO_3 ,” *Physical Review B*, vol. 100, no. 9, p. 094418, Sep. 12, 2019. DOI: 10.1103/PhysRevB.100.094418.
- [8] **E. Kenney**, A. Amato, S. R. Giblin, B. Z. Malkin, and M. J. Graf, “Suppression of M^+ depolarization by fast magnetic fluctuations at avoided level crossings for Ho^{3+} ions in CaWO_4 ,” *Physical Review B*, vol. 98, no. 13, p. 134424, Oct. 15, 2018. DOI: 10.1103/PhysRevB.98.134424.
- [9] R. F. Need, P. B. Marshall, **E. Kenney**, *et al.*, “Quasistatic antiferromagnetism in the quantum wells of $\text{SmTiO}_3/\text{SrTiO}_3$ heterostructures,” *npj Quantum Materials*, vol. 3, no. 1, p. 7, Dec. 2018. DOI: 10.1038/s41535-018-0081-8.

* Authors contributed equally.

Chapter 1

Introduction

1.1 Outline of Thesis

Magnetism is one of the oldest avenues of scientific inquiry. Thousands of years before electrical resistivity, phonon modes, or topological states were known, natural philosophers such as Thales of Miletus (640-546 B.C.) and Empedocles of Akragas (491-435 B.C.) were writing ‘papers’ on magnetism [1]. Some of the earliest scientific experiments were magnetic experiments performed by Petrus Peregrinus of Maricourt in the thirteenth century [1]. Over the past several thousand years magnets have been used for everything from navigation to medicine. One of the greatest achievements in condensed matter physics—indeed physics in its entirety—has been the systematic description and explanation of magnetism.

So perhaps it’s not surprising when I say that one of the most prolific and fertile fields of research in modern condensed physics is *frustrated magnetism*. Frustration in any system has the potential to generate a large variety of novel phases of matter. What might be surprising though is that the most exciting magnetic phenomenon to modern condensed matter physics is practically non-magnetic.

We define a non-magnetic system as one where the electronic contributions to the internal field are negligible beyond generic effects such as Landau diamagnetism or Pauli paramagnetism. A quantum spin liquid is a paramagnetic state where quantum fluctuations drive long-range magnetic order and spin fluctuations down to $T = 0$.

The quantum fluctuations also drive long-range spin-entanglement, which allows for fractional spin and charge excitations which do not obey the conventional exchange rules identical particles. Quantum spin liquids allow for the observation of chargeless $S = 1/2$ quasi-particles, known as spinons, which do not obey the fermi-exclusion principle. Such a system is incredibly attractive for study for both theoretical reasons and for technological applications.

In this thesis I review my experimental work on several distinct magnetically frustrated systems which had the potential to harbor QSL states. As an experimentalist, I specialize in μ SR (Muon Spin Rotation) and low temperature AC susceptibility ($AC\chi$) measurements, which have proven to be invaluable experimental techniques in the hunt for QSL systems. Low-temperature magnetic susceptibility is the most common way of observing a magnetic transition. μ SR is an advanced local-probe technique that uniquely allows one to probe the ground state for long-range magnetic order and magnetic fluctuations on the sub-unit-cell level of a system.

This thesis is structured as follows:

Chapter 2: I give a theory based introduction to the concept of quantum spin liquids, with an emphasis on the qualitative and experimental aspects.

Chapter 3: I describe the theory and technical aspects of μ SR measurements used in this thesis. This section is intended as an aid for readers unfamiliar with interpreting μ SR data.

Chapter 4: I discuss the $AC\chi$ and μ SR experiments I performed on the geometrically frustrated systems, $NaYbO_2$ and $LiYbO_2$. In $NaYbO_2$ my $AC\chi$ measurements uncovered an external field driven disordered phase, indicating the presence of a potential QSL-like phase down to 300 mK. In $LiYbO_2$, my μ SR measurements, in conjunction with our collaborator's neutron scattering measurements, show a spiral state that is characterized by a staggered transition of two independent long-range order parameters and low-temperature magnetic fluctuations.

Chapter 5: I discuss the $AC\chi$ and μ SR measurements I performed on the Kitaev honeycomb iridates, Cu_2IrO_3 and $Ag_3LiIr_2O_6$. The former displays charge state disorder in the Ir^{4+} ions which results in a magnetically inhomogeneous state of static

and dynamic magnetism. The latter is a system with subtle lattice defects that hide long-range magnetic order. Our μ SR measurements successfully uncovered the long-range order that disqualifies $\text{Ag}_3\text{LiIr}_2\text{O}_6$ as a QSL candidate.

Chapter 6: I discuss my $\text{AC}\chi$ and μ SR measurements on the metallic kagome system KV_3Sb_5 , as well as some of the developments in the literature since. KV_3Sb_5 was originally synthesized to be a magnetically frustrated system, and bulk susceptibility measurements seemed to confirm as much. Our μ SR measurements instead indicated a system dominated by nuclear dipole moments, where the only hint of electronic magnetism appeared in an anomalously weak temperature dependence of the depolarization rate. Our following $\text{AC}\chi$ measurements down to 300 mK showed that KV_3Sb_5 was a superconductor. Our observations of superconductivity and no spin-dipoles eventually led to the uncovering of an unusual charge density wave state characterized by orbital currents circulating about the kagome layers, which results in a weak current dipoles from the kagome layers.

Chapter 7: Finally, I discuss the conclusions one can draw from the entirety of the research presented in this thesis. My work yields substantial contributions to the field of frustrated magnetism for a wide variety of magnetically frustrated systems. My work also is invaluable in the search for quantum spin liquid candidates as it illustrates the pitfalls and complexities one encounters in interpreting data.

1.2 References

- [1] B. S. Baigrie and B. S. Baigrie, *Electricity and Magnetism: A Historical Perspective*, ser. Greenwood Guides to Great Ideas in Science. Westport, Conn.: Greenwood Press, 2007, 165 pp., ISBN: 978-0-313-33358-3.

Chapter 2

Quantum Spin Liquids and Magnetic Frustration

2.1 Introduction

In this chapter we review the basic concepts of quantum spin liquids (QSL). We only give a brief review of the concepts as necessary for this dissertation, as a full-length review can easily fill several review articles. The interested reader may consult select articles given at the end of this chapter. We focus on the essential theoretical concepts defining a QSL and their relation to experimental observations. We neglect most of the categorizations of QSL theories and the detailed experimental differences between models. Instead we focus on providing an intuitive understanding of the most common features found in QSL models.

2.2 What is a Quantum Spin Liquid?

The short-answer: A quantum spin liquid is a long-ranged disordered spin system with dynamical short-range correlations and long-ranged spin entanglement exhibiting non-trivial topology.

This is a rather modern definition, though, and quite vague. Quantum spin liquids have been investigated as a concept since the 1970's, which was before the idea of

topology became prevalent in condensed matter physics. Therefore the best way to explain what a “quantum spin liquid” is via history and examples.

2.2.1 A Very Brief History of the Notion

The term was first used to describe a “liquid-like” ground state predicted by Philip Anderson in 1973 when he applied Linus’s Pauling’s “resonating valence bond” (RVB) theory of metals to the triangular spin-1/2 antiferromagnet [1]. Anderson believed that the antiferromagnetic triangular lattice had a ground-state degeneracy that scaled exponentially with system size, roughly as 2^N . He predicted that this large-scale degeneracy in the ground state would result in novel type of correlated insulator where the ground state could be described as a “quantum liquid.” The idea was that quantum fluctuations would “melt” the ordered state, which was analogous to a solid, into a mobile fluid of valence bonds (spin singlets) down to $T = 0$. This was at a time when the ground state of any magnet was thought to be long-ranged ordered or spin-frozen. Anderson’s RVB model initially gained some interest as a theoretical concept, but ultimately languished as a theoretical curiosity until 1987 when Anderson published a second paper using his RVB model as a possible explanation for high-temperature superconductivity in La_2CuO_4 [2]. This paper provided a more robust theory and predicted exotic quasi-particle excitations while also drawing parallels to the extremely important Laughlin state predicted for the fractional quantum Hall effect [3]. Subsequent analysis found that this hypothetical “quantum spin liquid” state would host topologically non-trivial excitations with fractional spin excitations, and that the general concept could be viewed as a spin-analogue to the Laughlin state.

Interest eventually waned though, as Anderson’s original RVB model proved to be incorrect. The model was originally proposed as the ground state for the AFM Heisenberg model on a triangular lattice. The exact solution at the time was an outstanding problem in physics, and Anderson RVB model merely used heuristics and approximations to guess at the ground state. We now know the actual ground state of the triangular AFM Heisenberg lattice is the famous 120° -order state. Moreover, Anderson’s RVB model failed to provide an accurate description of superconductivity

in the cuprates, or in any other experimental system. Interest dried up by the early 2000's.

“Quantum spin liquids” as a concept came back in force in 2006 when Alexei Kitaev published a 110 page *tour-de-force* describing anyonic excitations and topological band structures—along with a host of other exotic properties that tantalized experimentalists and theorists alike [4]. Kitaev had created his own “Kitaev honeycomb model” that consisted of bond-frustrated $S = 1/2$ spins on a 2D honeycomb lattice. And unlike Anderson, Kitaev solved his model exactly. Kitaev’s honeycomb model predicted an exotic Laughlin-like spin-state with exotic anyonic spin excitations, topological band structures, dynamic spin correlations at $T = 0$, and quantum spin entanglement over macroscopic length scales. He even suggested a practical application: the spin excitations could be used to build a quantum computer. Interest in QSL’s exploded overnight.

The search for QSL’s has been healthy ever since. The theoretical description and definition of what a QSL is has been continuously developed by a stream of theoretical papers on the subject. QSL states have now been identified in a large number of numerical models, though the number of analytically solvable models like Kitaev’s is still extremely limited. Thankfully for Anderson, many of the numerical QSL models rely on recycled RVB concepts, so the RVB model is still relevant [5]. The result is a zoo of theoretical QSL states. The literature in the past ten years is filled with various sorts of esoteric models each describing what may be QSL state, all with their own properties. And experimentalists are out there, making new materials and measuring them to see if they can spot a QSL. So, what is our goal?

Our goal is to find a quantum spin liquid in a real material: Find a QSL, prove that it is a QSL, and study it.

2.2.2 But Really, What is a Quantum Spin Liquid?

Of course, to prove quantum spin liquids exist we need to have a more precise definition beyond the vague notion of a “quantum mechanically non-trivial disordered spin state” given above. We need an example.

The simplest example of a QSL system is the antiferromagnetic (AFM) 2D triangular Ising net,

$$\mathcal{H} = J \sum_{\langle ij \rangle}^N S_i^z S_j^z \quad J > 0.$$

Each spin bond can either be parallel or antiparallel. For AFM coupling, the energy of the system is minimized when all spins are antiparallel. But, as shown in figure 2-1, this is geometrically impossible on the triangular lattice; some spins must be forced parallel which maximizes their interaction energies. Moreover, the choice of which spins to align is arbitrary. As a result the system has macroscopic entropy at $T = 0$. For N spins the ground state entropy is [6]:

$$S(T = 0) \cong 0.3383 N k_B$$

The ground state degeneracy scales roughly as $e^{NK_B/3}$ with system size! Each of these ground states are connected via series of zero-cost spin swap operations (figure 2-2). Therefore the ground state's entire phase space is meaningfully accessible due to quantum spin fluctuations at $T = 0$. Since all degenerate states are accessible, there is no spontaneous symmetry breaking at $T = 0$. The spins do not freeze into a particular configuration like in a disordered spin-frozen state, because there are no energy barriers to prevent transitions between degenerate states. Thus, the system constantly fluctuates between superpositions of the $\sim e^{N/3}$ ground states at $T = 0$. This is distinct from the usual ordered or frozen states one expects at $T = 0$.

This state is a rudimentary quantum spin liquid state. Specifically, the system is a quantum correlated paramagnet, as there are dynamical short-range correlations between the spins. Quantum fluctuations prevent spin-freezing and instead they allow for dynamical short-range spin correlations down to $T = 0$. The presence of dynamical short-range correlations, no long-range correlations, and rotational symmetry is similar to the properties of a physical liquid. And like a physical liquid, the phase transition is generally not a well-defined transition that can be modeled using Landau

theory.¹ Hence, it is a “quantum spin liquid.”

More generally, modern QSL models have exotic properties that can be used for technological applications, or to advance our theoretical understanding of macroscopic quantum phases. Most QSL’s are expected to host some form of anyon quasiparticle excitations, some form of long-range entanglement, finite entropy and fluctuations at $T = 0$, and a symmetry preserving phase transition outside the description of Landau phase theory. The specific details, though, vary for each model.

We’ll define these ideas more fully as needed. The rest of this chapter is devoted to describing modern QSL theories and materials. But first: I’d like to take a few pages to analyze the $N = 3$ Ising triangle.

2.3 The $N = 3$ Ising Triangle

If you attend a talk on quantum spin liquids or magnetic frustration, there is a good chance you’ll see a figure similar to figure 2-1. It is the famous three spins one-halfs arranged in a triangle with antiferromagnetic Ising interactions. This figure is usually is meant as a simple short-hand that illustrates the spin frustration that underlies quantum spin liquid states. Yet, despite its ubiquity in the field, it’s surprisingly difficult to find any explicit solutions to the Ising triangle. Strictly speaking, the Ising triangle is periodic Ising chain with $N = 3$, and the periodic Ising chain has been solved for arbitrary N using second quantization and quasi-particle descriptions. But the sophisticated mathematical machinery used for arbitrarily sized Ising chains and other related models is inappropriate for a simple $N = 3$ system that can be easily solved using mundane methods and lacks the number of particles to make quasi-particle descriptions meaningful.

It is also inappropriate for an experimental dissertation to go over in detail the

¹Physical liquids do not have a conventional thermodynamic transition at temperatures and pressures above the critical point. The phase boundary vanishes and the gas and liquid phases become an indistinct ‘fluid’ that allows one to continuously move from a liquid to gas—and vice-versa—without crossing a thermodynamic transition. Spin liquids are similar to physical liquids in that the transition behavior and broken symmetries of the high-temperature paramagnetic states and low-temperature QSL states parallel the thermodynamic behavior of a gas-to-liquid transition.

sophisticated theory behind most QSL theories. The Ising triangle, though, is just right in its difficulty. Obviously, $N = 3$ is too small to show the collective behavior, such as quasi-particle excitations. That said, the Ising triangle does exhibit many of the fundamental properties required for a QSL phase, and can be considered as a kind of conceptual building block.

Consider a triangular lattice of $N = 3$ spin-1/2's with antiferromagnetic Ising couplings J . For simplicity, we ignore external fields. The Hamiltonian is given as:

$$\mathcal{H} = J \sum_{\langle ij \rangle}^{N=3} S_i^z S_j^z \quad J > 0, \quad (2.3.1)$$

where $\langle ij \rangle$ indicates a summation over nearest neighbor spins. Since $J > 0$, each spin-pair contributes $J/4$ if the spins are parallel, and $-J/4$ if the spins are antiparallel. Normally, the minimum possible value for equation 2.3.1 is achieved when all spins are antiparallel to their neighbors. But, because of the geometry of the problem, only two interactions can have their energy minimized; there is always one interaction with it's energy maximized.

To start, we'll attempt to write the eigenstates in terms of the direct product basis for three spins:

$$|\psi\rangle = \begin{cases} |\uparrow\uparrow\uparrow\rangle & |\downarrow\downarrow\downarrow\rangle \\ |\uparrow\downarrow\uparrow\rangle & |\downarrow\uparrow\downarrow\rangle \\ |\uparrow\uparrow\downarrow\rangle & |\downarrow\downarrow\uparrow\rangle \\ |\downarrow\uparrow\uparrow\rangle & |\uparrow\downarrow\downarrow\rangle \end{cases} \quad (2.3.2)$$

Each state is simply the direct product of three independent spin-1/2 states. (i.e. $|\uparrow\downarrow\uparrow\rangle \equiv |\uparrow\rangle_1 \otimes |\downarrow\rangle_2 \otimes |\uparrow\rangle_3$ with the usual matrix representation $|\uparrow\rangle = \begin{pmatrix} 1 \\ 0 \end{pmatrix}$, $|\downarrow\rangle = \begin{pmatrix} 0 \\ 1 \end{pmatrix}$)

We also define the usual spin operators for the three-spin states:

$$\begin{aligned}
\mathbf{S} &= \mathbf{S}_1 + \mathbf{S}_2 + \mathbf{S}_3 \\
S^z &= S_1^z + S_2^z + S_3^z \\
S^2 &= S_1^2 + S_2^2 + S_3^2 + 2\mathbf{S}_1 \cdot \mathbf{S}_2 + 2\mathbf{S}_1 \cdot \mathbf{S}_3 + 2\mathbf{S}_2 \cdot \mathbf{S}_3 \\
\mathbf{S}^+ &= \mathbf{S}_1^+ + \mathbf{S}_2^+ + \mathbf{S}_3^+ \\
\mathbf{S}^- &= \mathbf{S}_1^- + \mathbf{S}_2^- + \mathbf{S}_3^-
\end{aligned} \tag{2.3.3}$$

\mathbf{S}^+ and \mathbf{S}^- are the raising and lowering operators, and \mathbf{S} , S^z , S^2 are the usual spin operators.

It is easily seen that the product basis in 2.3.2 is already an eigenbasis of \mathcal{H} with eigenvalues of $3/4J$ and $-J/4$. The $E = 3J/4$ is two-fold degenerate with respect to the ferromagnetic states $|\uparrow\uparrow\uparrow\rangle$ and $|\downarrow\downarrow\downarrow\rangle$, and six-fold degenerate with respect to frustrated states, as expected.

At this point we might be tempted to simply write down the most general ground state $|\psi_0\rangle$ of this system using our intuition. Since the system is symmetric with respect to all three spins, we expect each frustrated state (for a given S^z) contribute equally.

Thus,

$$\begin{aligned}
|\psi_0\rangle &= \frac{1}{\sqrt{3}}(|\uparrow\uparrow\downarrow\rangle + |\uparrow\downarrow\uparrow\rangle + |\downarrow\uparrow\uparrow\rangle) \quad \text{for } S^z = 1/2 \\
&\quad \text{or,} \\
|\psi_0\rangle &= \frac{1}{\sqrt{3}}(|\downarrow\downarrow\uparrow\rangle + |\downarrow\uparrow\downarrow\rangle + |\uparrow\downarrow\downarrow\rangle) \quad \text{for } S^z = -1/2.
\end{aligned} \tag{2.3.4}$$

Our intuition isn't wrong here; these are the proper ground states of the system. Some care is needed though, since there's a bit more to these states than our physical intuition tells us. For example, the basis in 2.3.2 cannot be the proper basis for our system because it is non-symmetric.

Since we're dealing with half-integer spins, the wave-functions describing our spins—including position—must be antisymmetric under particle exchange.

$\Psi(S_1, S_2) = -\Psi(S_2, S_1)$. Any states which do not satisfy this condition are physically forbidden by fermi exclusion. Therefore we need to construct the correct basis for the problem from direct product basis.

The traditional way of constructing an antisymmetric basis for a system of spins is to introduce the spatial wave function. In general, the wave function of a spin system can be written as

$$\Psi(\vec{\mathbf{r}}_1 \dots \vec{\mathbf{r}}_N, S_1 \dots S_N) \phi(\vec{\mathbf{r}}_1 \dots \vec{\mathbf{r}}_N) \chi(S_1 \dots S_N) \quad (2.3.5)$$

where $\phi(\vec{\mathbf{r}})$ is the position wave function, and $\chi(\mathbf{S})$ is the spin-state. For example, this is how one rescues the triplet states in the non-interacting two spin-1/2 problem.²

Notice that this form requires the spin-state to be wholly symmetric and the spatial function to be wholly anti-symmetric, or vice-versa. Our direct product basis is neither wholly symmetric nor anti-symmetric under exchange, therefore we need to construct set of wholly symmetric and anti-symmetric eigenstates from our current basis in order for our states to be physical.³

Luckily, any combination of degenerate eigenstates yields another eigenstate. The question becomes how to construct a new basis that's both (anti)symmetric and orthonormal. A few approaches exist, but a bit of physical consideration let's us derive the correct basis without guessing. The Hamiltonian is clearly invariant under spin swaps; exchanging one spin with another in the triangle does not affect the energy in any of the direct product states. Therefore, the eigenstates of any spin-swap operator should also be eigenstates of the Hamiltonian. We define a three-way spin-swap operator as follows:

²See any elementary Quantum Mechanics textbook.

³An additional note: The physicality of a spatial wave function here is questionable for two reasons: One: our particles are confined to discrete lattice positions. And two: The Ising model is a simplification of the Heisenberg model, which in turn is a parameterization of the exchange problem in the first place. The coupling constant J is dependent on the position functions. This places constraints on what we can ask the spatial function to do, since J is a constant. We insist that the real-space wave-function needs to be identical for all three spins, with only the lattice site positions differentiating them.

Let \hat{P}_{ij} be an operator that swaps the i th and j th spins on the state $|ijk\rangle$:

$$\hat{P}_{ij} |ijk\rangle = \pm |jik\rangle. \quad (2.3.6)$$

We construct a three way swapping operator as

$$\hat{P} = \frac{1}{3}(\hat{P}_{12} + \hat{P}_{23} + \hat{P}_{13}). \quad (2.3.7)$$

This three way operator takes any direct product state and executes the three possible spin-swaps:

$$\hat{P} |ijk\rangle = \frac{1}{3} |jik\rangle + \frac{1}{3} |kji\rangle + \frac{1}{3} |ikj\rangle. \quad (2.3.8)$$

The eigenvectors of this state are then invariant under arbitrary spin-exchange to within a sign, and therefore either wholly symmetric or anti-symmetric.

The matrix representation of P can be found with some tedious—but simple—algebra:

$$\hat{P} = \frac{1}{3} \begin{bmatrix} 3 & 0 & 0 & 0 & 0 & 0 & 0 & 0 \\ 0 & 1 & 1 & 0 & 1 & 0 & 0 & 0 \\ 0 & 1 & 1 & 0 & 1 & 0 & 0 & 0 \\ 0 & 0 & 0 & 1 & 0 & 1 & 1 & 0 \\ 0 & 1 & 1 & 0 & 1 & 0 & 0 & 0 \\ 0 & 0 & 0 & 1 & 0 & 1 & 1 & 0 \\ 0 & 0 & 0 & 1 & 0 & 1 & 1 & 0 \\ 0 & 0 & 0 & 0 & 0 & 0 & 0 & 3 \end{bmatrix} \quad (2.3.9)$$

Finding the eigenvalues and eigenvectors of this matrix possesses no difficulty outside of patience. This matrix has two unique eigenvalues, each four-fold degenerate: $\lambda = \{1, 1, 1, 1, 0, 0, 0, 0\}$ The orthonormal basis is as follows:

$$\begin{aligned}
& \lambda = 1 \\
& \begin{array}{cc}
|\uparrow\uparrow\uparrow\rangle & |\downarrow\downarrow\downarrow\rangle \\
\frac{1}{\sqrt{3}}(|\uparrow\uparrow\downarrow\rangle + |\uparrow\downarrow\uparrow\rangle + |\downarrow\uparrow\uparrow\rangle) & \frac{1}{\sqrt{3}}(|\downarrow\downarrow\uparrow\rangle + |\downarrow\uparrow\downarrow\rangle + |\uparrow\downarrow\downarrow\rangle)
\end{array}
\end{aligned}$$

$$\begin{aligned}
& \lambda = 0 \\
& \begin{array}{cc}
\frac{1}{\sqrt{2}}(|\uparrow\downarrow\uparrow\rangle - |\uparrow\uparrow\downarrow\rangle) & \frac{1}{\sqrt{2}}(|\downarrow\uparrow\downarrow\rangle - |\uparrow\downarrow\downarrow\rangle) \\
\frac{1}{\sqrt{2}}(|\downarrow\uparrow\uparrow\rangle - |\uparrow\uparrow\downarrow\rangle) & \frac{1}{\sqrt{2}}(|\downarrow\downarrow\uparrow\rangle - |\uparrow\downarrow\downarrow\rangle)
\end{array} \tag{2.3.10}
\end{aligned}$$

The first set of eigenvectors with $\lambda = 1$ are exactly what we wanted: They're a set of fully symmetric eigenstates to the Hamiltonian. On the other hand, while the second set with eigenvalues of $\lambda = 0$ do technically satisfy the condition $\hat{P}|\phi\rangle \pm |\phi\rangle$. While this satisfies the condition we imposed, four of the states are clearly not symmetric.

The reason that we end up with four non-symmetric states is because there are no other linearly independent choices for symmetric or antisymmetric states. As a general mathematical fact, if the number of unique particle states for a single particle is less than the total number of particles, then it is impossible to form fully antisymmetric states due to repetition of quantum numbers [7]. For spin-1/2, this occurs when $N \geq 3$. Therefore only four linearly independent states are possible, and the remaining states are annihilated by \hat{P}

Physically, this means that four of our six-fold degenerate ground states are physically forbidden by symmetry, and the overall Hilbert space is reduced from a dimension of eight to four. The remaining states are wholly symmetric and therefore can be repaired using an antisymmetric spatial wave function. I.e.:

$$|\Psi\rangle = \psi(\vec{\mathbf{r}}_1, \vec{\mathbf{r}}_2, \vec{\mathbf{r}}_3)\chi(\mathbf{S}_1, \mathbf{S}_2, \mathbf{S}_3) \tag{2.3.11}$$

$\chi(S_1, S_2, S_3)$ is any spin state formed by our allowed basis, while the antisymmetric position wave-function is defined as:

$$\psi(\vec{\mathbf{r}}_1, \vec{\mathbf{r}}_2, \vec{\mathbf{r}}_3) = \frac{1}{\sqrt{6}} \sum_{i,j,k} \epsilon_{ijk} \phi(\vec{\mathbf{r}}_i, \vec{\mathbf{R}}_1) \phi(\vec{\mathbf{r}}_j, \vec{\mathbf{R}}_2) \phi(\vec{\mathbf{r}}_k, \vec{\mathbf{R}}_3) \quad (2.3.12)$$

Here ϵ_{ijk} is the chevy-levita symbol, while $\psi(\vec{\mathbf{r}}_i, \vec{\mathbf{R}}_a)$ is the spatial wavefunction of spin i , with site position $\vec{\mathbf{R}}_a$

The end result is that the proper basis for the Ising Triangle only has a total of four states, with only two being physically unique due to spin-inversion-symmetry

$$|S_1 S_2 S_3\rangle = \begin{cases} |\uparrow\uparrow\uparrow\rangle & |\downarrow\downarrow\downarrow\rangle \\ \frac{1}{\sqrt{3}}(|\uparrow\uparrow\downarrow\rangle + |\uparrow\downarrow\uparrow\rangle + |\downarrow\uparrow\uparrow\rangle) & \frac{1}{\sqrt{3}}(|\downarrow\downarrow\uparrow\rangle + |\downarrow\uparrow\downarrow\rangle + |\uparrow\downarrow\downarrow\rangle) \end{cases} \quad (2.3.13)$$

These are the ground states are the states we guessed at all the way back in equation 2.3.4! Now we ask what happens when we apply an external field:

Let

$$\mathcal{H} = J \sum_{\langle ij \rangle}^N S_i^z S_j^z - \sum_i \mu S_i^z B \quad (2.3.14)$$

where B is an external magnetic field along the z -axis and μ is the effective moment. The field dependent term clearly commutes with the Hamiltonian H in general. Therefore the eigenstates in both (2.3.4) and (2.3.13) remain eigenstates and the above derivation is largely unchanged. The only difference is that the external field removes all the degeneracies of the states listed in (2.3.13), and that $|\uparrow\uparrow\uparrow\rangle$ will become the ground state when $B > \frac{J}{\mu}$. Thus, the zero-field solution is stable for sufficiently small fields, and we are justified in ignoring the degeneracies in (2.3.13). Next, we apply the spin operators on our states.

Regardless of field, acting the composite spin operators S^z and \mathbf{S}^2 (eq. 2.3.4) on these states yields $S = 3/2$ for all four states. The ground states, despite their appearance, are high-spin states. The $|\uparrow\uparrow\uparrow\rangle$ and $|\downarrow\downarrow\downarrow\rangle$ states are $S^z = 3/2$, as expected, while two ground states are $S^z = 1/2$, $S^z = -1/2$ for the two-spin up and two-spin

down states, respectively. Unsurprisingly then, the following is true:

$$\begin{aligned}
S^- |\uparrow\uparrow\uparrow\rangle &\rightarrow |\uparrow\uparrow\downarrow\rangle + |\uparrow\downarrow\uparrow\rangle + |\downarrow\uparrow\uparrow\rangle \\
S^+ |\downarrow\downarrow\downarrow\rangle &\rightarrow |\downarrow\downarrow\uparrow\rangle + |\downarrow\uparrow\downarrow\rangle + |\uparrow\downarrow\downarrow\rangle \\
S^- (|\uparrow\uparrow\downarrow\rangle + |\uparrow\downarrow\uparrow\rangle + |\downarrow\uparrow\uparrow\rangle) &\rightarrow |\downarrow\downarrow\uparrow\rangle + |\downarrow\uparrow\downarrow\rangle + |\uparrow\downarrow\downarrow\rangle
\end{aligned} \tag{2.3.15}$$

All the physically allowable states in the Ising-triangle belong to a single spin quartet. The Ising triangle behaves like a spin-3/2 particle.

We now discuss the implications of our derivation so far and how they relate to the fundamental properties of a QSL:

1: The ground-state is entangled as a result of symmetry constraints. By definition, any state that cannot be represented as a direct-product state of the individual spins is entangled. This can be confirmed by calculating the Von Neumann entropy⁴ for an individual spin as

$$S_A = -\text{Tr}[\rho_A \ln \rho_A] = \ln \left[\frac{3}{\sqrt[3]{4}} \right] \cong 0.637 > 0,$$

where ρ_A is the reduced density matrix of $|\psi_0\rangle$ relative to spin ‘A’.

Many-particle entanglement is a fundamental requirement for QSLs. Entanglement over the bulk of a material is what allows for the exotic quasiparticle excitations known as “anyons” to exist. Anyons are spin excitations that have fractionalized charge or spin numbers. Consequently, they are neither fermions nor bosons, but instead obey non-trivial mutual exchange statistics. Many-particle entanglement is a requirement for anyons to exist, since spin excitations in a simple product state simply result in $\Delta S = \pm 1$ spin flips.

2: The ground-state is protected from local spin component measurements on $\vec{S}_i = (S_i^x, S_i^y, S_i^z)$ by symmetry requirements. A quick application of a spin operator shows that $S_i^z |\psi_0\rangle \neq |\psi_0\rangle$ and results in a non-symmetric wave-function, which is

⁴The Von Neumann entropy is a measure of entanglement. $S_A = 0$ for non-entangled states, and $S_A = \ln N$ for a maximally entangled state with Hilbert Space dimension N . Alternatively, one can calculate that $|\psi_0\rangle$ has a Schmidt number of 2 under Schmidt decomposition.

forbidden by symmetry. More specifically, a measurement of S_i^z can only collapse $|\psi_0\rangle$ to either $\frac{1}{\sqrt{2}}(|\uparrow\rangle_i(|\downarrow\uparrow\rangle + |\uparrow\downarrow\rangle))$ or $|\downarrow\rangle_i|\uparrow\uparrow\rangle$, which are not valid states.

Protection from local spin operators is another key aspect of quantum spin-liquids. The anyonic excitations described above cannot be created by local spin operators. Instead, they are created as infinite product of local operators (in the $N \rightarrow \infty$ limit) acting on the system as a whole. Correspondingly, anyons are non-local excitations. Note that anyons are created in pairs which themselves are long-ranged entangled over the bulk of the material. This is one of the key properties of QSL's for technological applications (i.e. quantum computers), and requires long-range spin-entanglement that's protected from local spin excitations, just as we see in the spin-triangle.

3: The entangled state is topological. Obviously, we don't mean topological in the sense of band-structure or Chern numbers. Instead, we mean topological in the original sense that the physicist Michael Berry introduced used when he first introduced topology as a way to think about physical systems [8]. A topological system is any system which there exists a quantity that is non-trivially invariant under adiabatic manipulation of \mathcal{H} [8]. For example, the phases of spins moving under a magnetic field (Berry Curvature) and the Aharonov-Bohm effect were examples Berry gave.

The $N = 3$ triangle can be thought of as topological in two different ways. The first is the inversion of spin under periodic exchange of electrons. Figure 2-3 shows what happens when one moves an electron in a closed loop along a conventional $N = 4$ square and the $N = 3$ triangle. The end-state is identical to the initial state in the frustrated square, as expected. In the $N = 3$ triangle, the spin flips and the end state is different from the initial state. Therefore there is a finite Berry curvature and the system is topological.

Alternatively, one can take the entanglement entropy of the observable states to be the invariant. The entanglement entropy (Von Neumann entropy) is invariant under adiabatic changes to B , J , and $\vec{\mu}$, for $\mu B < J$. Above this, the ground state transitions to the ferromagnetic state $|\uparrow\uparrow\uparrow\rangle$ with Von Neumann entropy $S = 0$.

In the $N \rightarrow \infty$ limit, the limited concept of topology used here gives rise to the

more conventional definitions of topology, where the long-range entanglement of the triangular net is protected by topological invariants. The problems of topology and entanglement in QSL's are, in many respects, one and the same, so much of the theory on QSL's can be recast into the language of topology.

What is missing from our example is the emergence of collective phenomena that can only be seen in the many-body problem when $N \gg 3$. In that sense, we've separated out the fundamental properties of the ground state due to magnetic frustration from the emergent properties due to statistical mechanics. QSL states are built on these building blocks, and thanks to these building blocks we expect to see exotic collective phenomena such as fractional spin-excitations, spin-charge separation, flux vortices of the underlying topology, and so on. The exact details, though, depend on the underlying models themselves.

A quantum spin liquid isn't a unique phase of spins, like a simple ferromagnet or paramagnet is. Rather, it is an entire classification of spin ground states that are characterized by macroscopic spin entanglement resulting from the microscopic spin frustration we see here.

2.4 Elementary Theories of Quantum Spin Liquids

A quantum spin liquid (QSL) is any magnetic phase of matter where the spins are dynamically short-range correlated and do not undergo a conventional thermodynamic transition to a lower-symmetry state as $T \rightarrow 0$. Instead, quantum fluctuations 'melt' the thermodynamic spin-lattice and allow the spins to remain in a 'liquid-like' quantum-paramagnet state. The dynamic spin correlations are short-ranged, and there exist fractionalized spin-1/2 excitations known as spinons due to ground-state entanglement. The exact properties of a QSL depend on several factors, including the dimensionality of the spin lattice, and the exact mechanism of spin frustration. Most QSL's are grouped into one of three families, depending on either the model or the mathematical symmetries obeyed by the quasi-particles.

The three primary types of quantum spin liquids one encounters in the literature

are:

- Kitaev Spin Liquids
- $U(1)$ (RVB) Spin Liquids
- \mathbb{Z}_2 (RVB) Spin Liquids

In the following sections we'll discuss the models underlying these classifications and some of their properties.

2.4.1 Kitaev honeycomb Model

The Kitaev honeycomb model is an exactly solvable model proposed by Kitaev in 2005 [4]. The Kitaev model consists of the following spin-1/2 Hamiltonian on a 2D honeycomb lattice:

$$\mathcal{H} = -J_x \sum_{x \text{ bond}} \sigma_i^x \sigma_j^x - J_y \sum_{y \text{ bond}} \sigma_i^y \sigma_j^y - J_z \sum_{z \text{ bond}} \sigma_i^z \sigma_j^z \quad (2.4.1)$$

$$0 \leq |J_x|, |J_y|, |J_z| \leq 1$$

where each ‘bond’ is a nearest-neighbor spin interaction defined by its orientation. See figure 2-4. At first glance, the Kitaev model looks like an anisotropic Heisenberg model. Except, the Kitaev model is neither antiferromagnetic nor geometrically frustrated. It is a bond-frustrated model. The spin interactions J_α can all be ferromagnetic ($J_\alpha \geq 0$) if desired, and the honeycomb lattice can easily be populated with AFM spins without frustration. A closer inspection reveals that the Kitaev model is actually somewhere in-between the Heisenberg and Ising models.

Each individual spin sees an overall three-dimensional ‘Heisenberg-like’ interaction with its environment. At the same time, each term is an Ising-like interaction with one of three neighboring spins. The magnetic frustration is a result of each spin being ‘pulled’ in three orthogonal directions—despite being a 2D lattice. In particular, the fact that σ_x , σ_y and σ_z are all incompatible observables forces an individual spin to take on a mixed state to minimize its energy in eq. 2.4.1. In turn every spin is forced

to take on a mixed state to minimize the Hamiltonian, and the result is a highly entangled ground state with no long-range disorder. I.e. a QSL.

This assumes that such a Hamiltonian is physically possible, which seems implausible at first glance, given the symmetry of the honeycomb lattice. In fact, the Kitaev model is formally a compass model which for years lacked a physical realization for quantum spins [9], [10]. The Kitaev model is realizable in certain iridium and ruthenium compounds, particularly the oxides, thanks to spin-orbit coupling (SOC) [11], [12]. The conditions are rather specific: One requires a magnetic ion with a d^5 spin configuration, an effective angular momentum of $l = 1$ and an octahedral coordination that yields a low-spin t_{2g} ground state with a Kramer’s degeneracy [10]. This results in an effective spin-1/2 ion. Strong SOC mixes the $J = L_z = 0$ and $L_z = 1$ orbital states with the effective spin-1/2 states, resulting in so-called ”isospin” states.⁵ The effective exchange Hamiltonian for nearest neighbors (NN) becomes:

$$H_{ij} \sim J_1(\vec{\mathbf{S}}_i \cdot \vec{\mathbf{S}}_j) + J_2(\vec{\mathbf{S}}_i \cdot \vec{\mathbf{r}}_{ij})(\vec{\mathbf{r}}_{ij} \cdot \vec{\mathbf{S}}_j) \quad (2.4.2)$$

where $\vec{\mathbf{r}}_{ij}$ is the unit vector along a given bond- ij . For edge-sharing octahedra with a 90° bond angle, the A-C-A (A=Anion, C=Cation) superexchange paths along the top and bottom routes destructively interfere and cancel out the isotropic portions of the exchange Hamiltonian, and instead result in—with some simplification—a purely anisotropic exchange interaction that depends on the real-space bond directions:

$$H_{ij}^{(\gamma)} = -JS_i^\gamma S_j^\gamma \quad (2.4.3)$$

where $\gamma = (x, y, z)$ labels the bonds by its real-space direction. The simplest example of this arrangement is that of edge-sharing octahedra where the anions form a square lattice (figure 2-5). For other geometries, such as the IrO_6 octahedra which form the Ir^{4+} Honeycombs in A_2IrO_3 , the overall result still holds if the lattice can be broken down into 90° oriented superexchange pathways along oxygen cations. In

⁵”Isospin” is a reference to the spin-like mechanics of meson formation. Structurally, the states are the same.

these cases the exchange interaction over each bond remains writeable in cartesian form $H_{ij}^{(\gamma)} = -JS_i^\gamma S_j^\gamma$ while the orbitals themselves may point along non-orthogonal directions, as seen in figure 2-6. In other words: the neighboring spin-interactions are orthogonal even if the bond directions are not.

The number of ions which can satisfy these conditions in realizable materials are limited. Currently research has focused on magnetic iridium (Ir^{4+}) and Ruthenium ($\text{Ru}^{3+}/\text{Ru}^{4+}$) ions. Prominent examples are LiYbO_2 , NaYbO_2 , Cu_2IrO_3 , $\text{H}_3\text{LiIr}_2\text{O}_6$, and $\alpha\text{-RuCl}_3$ [13], [14]. Notice the emphasis on iridium oxides; iridium naturally has much stronger SOC than ruthenium. Progress on alternative Kitaev compounds has been slow, though they do exist. Cobalt-oxides are currently one avenue that is being explored [15].

Now that we know that the Kitaev honeycomb model is plausible in real systems, what does its solution look like? The method Kitaev published is mathematically sophisticated and highly non-trivial. But we can outline some key details and results.

The Kitaev Hamiltonian in eq. (2.3.13) can be rewritten in terms of Majorana fermion operators using the language of second quantization. Specifically, if the standard annihilation and creation operators for a fermion in state k are defined as a_k and a_k^\dagger , then one can construction Majorana operators as

$$b_{2k-1} = a_k + a_k^\dagger, \quad b_{2k} = \frac{a_k - a_k^\dagger}{i}. \quad (2.4.4)$$

These Majorana operators satisfy the following relations:

$$\begin{aligned} b_j &= b_j^\dagger \\ \{b_j b_l\} &= 0 \quad \text{if } l \neq j. \end{aligned} \quad (2.4.5)$$

The first relation confirms that the Majorana operator is Hermitian (i.e. observable⁶) while the third is the anti-commutator relation defining fermions in second-quantization. The Majorana operators can be interpreted as the creation and annihilation operators for a set of quasi-particles analogous to Majorana fermions; fermions

who are their own antiparticles (i.e. $b_j = b_j^\dagger$). More accurately, these operators represent Majorana zero modes (MZM), which are zero-energy excitations of the ground-state wave-function that do not necessarily obey Boson-Fermi statistics despite the quasi-particle description [16].

Using a set of four Majorana operators, plus a fair bit of technical detail, one can simplify the original Hamiltonian into a single NN sum over "Majorana spin" interactions [10]:

$$H(A) = \frac{i}{4} \sum_{\langle j,k \rangle} \hat{A}_{jk} c_j c_k \quad (2.4.6)$$

The term $c_j c_k$ is the spin-spin operator corresponding to a set of NN Majorana fermions, analogous to the $\sigma_i^{(\gamma)} \sigma_j^{(\gamma)}$ terms in the original Hamiltonian. The factor \hat{A}_{jk} is a matrix which happens to commute with the original Hamiltonian.

This simplified Hamiltonian allows one to solve for the eigenstates of the Kitaev model in terms of Majorana fermion states. Each individual spin in the electron picture is broken up into four Majorana quasiparticles, b^x, b^y, b^z, c , relative to the bond directions (figure 2-7). This can be further simplified into two quasiparticle excitations; spinons and vortex excitations.

The spin excitations are 'spinons', which are non-interacting $S = 1/2$ Majorana quasiparticles with have zero electric charge. This is as opposed to magnons which are $S = 1$ bosonic excitations. The vortex excitations, sometimes called 'flux-excitations' or "visions," are quasi-particle analogues to magnetic flux excitations in superconductors. They affect the phase of the spinon wave-functions over closed loops. Both excitations are considered anyons, whose wave functions are not limited to being symmetric or anti-symmetric under particle exchange.

The exact nature of the excitations depends on the ratios of J_x, J_y , and J_z . Amazingly, the ground-state energy is independent of the signs of the spin-interactions, so model works for both ferro and anti-ferromagnetic systems. Note though, the

⁶The standard creation and annihilation operators are not Hermitian, and therefore not observable. The observable for a_k and a_k^\dagger is the occupation number operator, $n_k = a_k a_k^\dagger$. The identity $b_j = b_j^\dagger$ implies that the quasi-particles excitations are individually observable, which ties into their potential usage to hold qubits in quantum computers [17].

AFM kitaev model is considered to be more stable at finite temperatures [12]. For $J_x \cong J_y \cong J_z$, the spinon excitations of the system are gapless. For $|J_i| \leq |J_j| + |J_k|$, $i = (x, y, z)$ the excitations are gapped. The vortex excitations are gapped in both regions. In the gapless region, the spinons acquire an energy gap given sufficient magnetic fields. Once gapped, these spinons obey non-Abelian statistics, which is potentially useful for designing quantum computers.

But is it a quantum spin liquid? Yes. Shortly after Kitaev's original paper, Baskaran, Mandal, and Shankar [18] showed that the dynamical spin-correlations in the ground state are identically zero beyond NN separation. In other words, at $T = 0$ are dynamically short-ranged correlated, which defines a quantum spin liquid. Furthermore, the mere presence of spinon excitations confirms that the system is long-range spin entangled. This is because an elementary spin excitation, such as a magnon, must have integer spin due to angular momentum selection rules ($\Delta S = 1$). Spinons are created by splitting–fractionalizing–an $S=1$ magnon into two deconfined $S = 1/2$ spinons. Spinons can only exist as well-defined quasi-particles in the presence of long-range spin-entanglement, which preserves the $\Delta S = 1$ condition while also allowing the excitation to be observed as two spatially independent $S = 1/2$ particles [5], [11].

2.4.2 Observables and Predictions of the Kitaev QSL

Next, we seek to understand the observable properties of the Kitaev QSL. For such a physically exotic phase of matter, it is surprisingly difficult to observe the unique properties of a QSL. A true QSL phase is not described by Landau 2nd order transition theory, and therefore does not have a well-defined thermodynamic transition or latent heat [13]. The spinon excitations have zero electric charge, and therefore cannot be directly detected by conventional electronic measurements. Magnetically, the spinons are similar to dilute, non-interacting, magnetic impurities, and are primarily coupled to the vortex excitations. Thus, despite being an exotic magnetic phase of matter, the bulk magnetism of a QSL is nearly impossible to distinguish from a quantum paramagnet using traditional techniques.

Predictions do exist. The simplest consequence of the QSL state is a possible quantization of thermal transport due to chiral edge-states. The spinons, by virtue of being well-defined topological quasi-particles, can form a ‘fermi-like’ surface with a Chern number of ± 1 [11]. This guarantees chiral edge states—spinon currents—exist along the surface of the material. This causes a quantized contribution to the thermal transport similar the quantized resistance in the integer quantum Hall effect [4].

At finite temperatures, the spinon and vortex excitations are expected to appear at different temperature scales, T_H and T_L [11]. This is referred to as thermal fraction-ization. At $T \gtrsim T_H$, the system behaves as a conventional, frustrated, paramagnet. Between $T_L \lesssim T \lesssim T_H$, the system enters an intermediate ‘unconventional paramagnet’ state as spinons begin forming. Finally, below $T \lesssim T_L$, the system crosses over to a QSL state as vortex excitations begin to localize. Physically, these temperatures are set from the density of states of the spinons, and the energy gap of the vortex ex-citations. Experimentally, this results in a broad ‘two-peak’ structure in the specific heat (figure 2-8). Such structures frequently appear as a result of magnetic impurities or other phase transitions which occur frequently in frustrated materials. Thus, this structure is usually treated as an encouraging sign, rather than a definitive signature of a QSL.

The presence of exotic spin excitations can also, in theory, be probed by scattering techniques, such as neutron or Raman scattering. Neutron Scattering in particular has been widely employed due to its ability to detect long-range magnetic order and spin-excitations. The inelastic neutron scattering (INS) spectra of a QSL is thought to be a broad featureless spectra. The intensity of the spectra, and fine details, change as the temperature is lowered through the T_L and T_H energy scales. Of course, there are many reasons why a material may have a bland excitation spectra [14] hence INS or similar scattering data normally cannot prove that a QSL state exists.

Magnetically, a Kitaev system acts as like quantum (correlated) paramagnet [12]. For simplicity, take $J_x = J_y = J_z = J$. At high temperatures the system is paramag-netic, with a bulk susceptibility of $\chi_{DC} \sim \frac{1}{T}$. For $T \sim J$, $\chi_{DC} \sim \frac{1}{4T \mp J}$. Between T_L and T_H a peak appears: for $J > 0$ (FM), $T_p \simeq 0.02J$, and for $J < 0$ (AFM),

$T \simeq 0.1J$. Finally, as $T \rightarrow 0$, the susceptibility continues to decrease and approaches a non-zero value. The paramagnetic behavior is similar to what is seen in spin glasses, spin-freezing, and magnetic impurities.

2.4.3 Anderson RVB— $U(1)$ and \mathbb{Z}_2 Spin Liquids

Next, we briefly review the properties of RVB-based models. These are variational models used for numerical computations of geometrically frustrated systems. Anderson’s original RVB models for triangular lattices and unconventional superconductivity turned out to be incorrect. The triangular Heisenberg AFM has a 120° -order ground state, while superconductivity in the cuprates is still not fully understood. That said, the basic premise of RVB states is physically plausible and the large body of theory behind them is valid; one just needs a system that actually has an RVB ground-state. As a result, Anderson’s RVB theory has a third life as the basis for variational techniques on geometrically frustrated QSL systems. These are numerical theories which use the superconducting RVB states from Anderson’s theory of RVB superconductivity to construct wave-functions for modern variational theory calculations. We now outline the basic idea based on the review article by Zhou [5].

We consider the ground state of a geometrically frustrated magnet. Similar to the original RVB model we assume that the ground state is highly degenerate and that each degenerate state can be described as a set of coupled spin dimers (figure 2-10). As a further ansatz, we assume that the ground state to be a sum over all possible dimer configurations:

$$\begin{aligned} |\Psi_{\text{RVB}}\rangle &= \sum_{\{(ij)_1 \dots (ij)_n\}} a_{ij}^1 |\psi_{ij}\rangle_1 \otimes a_{ij}^2 |\psi_{ij}\rangle_2 \otimes \dots \otimes a_{ij}^n |\psi_{ij}\rangle_n \\ &= \sum_{(i_1 j_1 \dots i_n j_n)} a_{(i_1 j_1 \dots i_n j_n)} |(i_1 j_1) \dots (i_n j_n)\rangle, \end{aligned} \quad (2.4.7)$$

with $|\psi_{ij}\rangle_k$ being the k th labeled dimer state between spins i and j . Explicitly,

$$|\psi_{ij}\rangle = \frac{1}{\sqrt{2}}(|\uparrow_i \downarrow_j\rangle - |\downarrow_i \uparrow_j\rangle) \quad (2.4.8)$$

Each term in equation 2.4.7 is a tensor product of all dimers states in a given micro-state, each with a weight $a_{(i_1 j_1 \dots i_n j_n)}$ that acts as our variational parameter.

For an infinitely large system the number of possible configurations extends to infinity, making the equation intractable. But, based on Anderson's prior attempts to apply RVB theory to the cuprates, the BCS wave-functions are natural candidates for a variational theory of frustrated magnetism. We construct the variational RVB states using Gutzwiller projected (P_G)⁷ BCS states as our basis:

$$\begin{aligned} |\Psi_{\text{RVB}}\rangle &= P_G |\Psi_{\text{BCS}}\rangle \\ |\Psi_{\text{BCS}}\rangle &= \prod_k (u_{\mathbf{k}} + v_{\mathbf{k}} c_{\mathbf{k}\uparrow}^\dagger c_{-\mathbf{k}\downarrow}^\dagger) |0\rangle \end{aligned} \quad (2.4.9)$$

$c_{\mathbf{k}\uparrow}^\dagger$ and $c_{-\mathbf{k}\downarrow}^\dagger$ are the electron creation operators, while $u_{\mathbf{k}}$ and $v_{\mathbf{k}}$ are numerical coefficients to be determined. Note: The Gutzwiller projected BCS states are not equivalent to standard BCS states. Conventional superconducting BCS theory allows for each lattice site to host 0, 1, or 2, electrons while RVB theory only allows lattices sites to host 0 or 1 electrons. The Gutzwiller projection eliminates the double occupation states and allows us to express the problem in terms of $u_{\mathbf{k}}$ and $v_{\mathbf{k}}$.

The process of determining $u_{\mathbf{k}}$ and $v_{\mathbf{k}}$ is rather complicated and, surprisingly, introduces much of the physics that differentiates different QSL states by their symmetries. We give only the briefest of outlines for the ensuing steps.

The coefficients $u_{\mathbf{k}}$ and $v_{\mathbf{k}}$ for a superconductor are determined through a set of equations known as the Bogoliubov-de-Gennes equations, which are a set of self-consistent equations obtained through a mean-field approximation of the BCS Hamiltonian, followed by a Bogoliubov transformation⁸. If we were analyzing BCS theory, we would take the BSC Hamiltonian, H_{BCS} , and perform a standard mean-field approximation written out in second-quantization notation. We then would perform a Bogoliubov transformation on the Hamiltonian, yielding our final MF BCS Hamiltonian, $H_{\text{BCS}}^{\text{MF}}$. We then diagonalize $H_{\text{BCS}}^{\text{MF}}$, which due to the specific of the Bogoliubov

⁷The Gutzwiller projection is a technique frequently used to construct wave-functions for variational theories. The theoretical details fall outside the scope of this work.

⁸Again, the details of this transformation fall out of the scope of this work.

transformation, implicitly solves for $u_{\mathbf{k}}$ and $v_{\mathbf{k}}$ in the form of self-consistent equations known as the Bogoliubov-de-Gennes (BdG) equations.

Determining $u_{\mathbf{k}}$ and $v_{\mathbf{k}}$ for an RVB theory follows more or less the same procedure, but with additional complications. The first complication is that we are not working with native BCS states, but a Gutzwiller projection of BCS states. The second complication is that RVB theory assumes localized spins on lattice sites which allows for only single- or zero-occupancy on a given site, while BCS theory allows for 0, 1, or 2 occupancy on a site. Therefore we have the condition of

$$\sum_a f_{ia}^\dagger f_{ia} = 1, \quad (2.4.10)$$

where f_{ia}^\dagger and f_{ia} are the second-quantization fermion creation and annihilation operators, respectively. Here $a = \{\uparrow, \downarrow\}$ is the spin index, and i is the site index.

The third complication is that we do not necessarily start with the standard BCS Hamiltonian. Instead we start with a spin Hamiltonian. For example, the nearest neighbor Heisenberg Hamiltonian:

$$H = J \sum_{\langle i,j \rangle} \vec{\mathbf{S}}_i \cdot \vec{\mathbf{S}}_j. \quad (2.4.11)$$

These differences from the standard BCS theory of superconductors have important ramifications—and complicate the algebra involved substantially. It is well beyond the scope of this experimental dissertation to delve any further into the technical aspects of RVB models. Rather, we refer the interested reader to the excellent review article by Zhou, Kanoda, and Ig [5]. For our purposes, we are interested in the gauge redundancy from the above process.

The above process of determining $u_{\mathbf{k}}$ and $v_{\mathbf{k}}$ contains a mean-field approximation, which makes the final BCS states implicitly mean-field states. Equation 2.4.9 can be written equivalently as $|\Psi_{\text{RVB}}\rangle = P_G |\Psi_{\text{MF}}\rangle$. The usage of a mean-field wave-function results in a redundancy in our representation of $|\Psi_{\text{RVB}}\rangle$ where multiple mean-field states correspond to the same RVB state after Gutzwiller projection. This results in

a gauge invariance in our representation of the individual spin-states forming the RVB states, and this gauge invariance plays a key-role in describing low-energy excitations.

For example, lets say we wanted to represent the spin operators in terms of second-quantization fermion operators $\{f_{ia}\}$, where i is the site index and a is the spin index ($a = \{\uparrow, \downarrow\}$). Because we solved for the RVB states by a MF approximation to the BCS states and then followed up with a Gutzwiller projection, the following gauge transformation is valid:

$$f_{ia} \rightarrow f'_{ia} = e^{i\theta(i)} f_{ia} \quad (2.4.12)$$

Formally, this is the definition of a $U(1)$ gauge symmetry. Note that traditional BCS theory breaks $U(1)$ symmetry due to being particle-nonconserving. Here, the ‘symmetry’ is a byproduct of our approximate representation of our variational states. This symmetry can be expanded upon further by considering particle-hole symmetries which allows one to write the spin-operator in such a way that it is invariant under $SU(2)$ gauge transformations.

Note though, that the MF Hamiltonian obtained in constructing the RVB states has a local $SU(2)$ gauge structure inherited from the $SU(2)$ symmetry of the spins. Additionally, the usage of a mean-field Hamiltonian $H_{\text{BCS}}^{\text{MF}}$ introduces several mean-field parameters for each possible QSL state. The exact MF parameters, and the exact MF Hamiltonian depend on your chosen representation—so for brevity we omit the equations—but the combination of the global $U(1)$, local $SU(2)$, and the freedom in choosing MF parameters places limits on the possible irreducible symmetry groups the system satisfies. It can be shown that there are only three plausible gauge symmetries, dependent on the MF parameters, that a RVB QSL may satisfy: $U(1)$, $SU(2)$, and \mathbb{Z}_2 .

Physically, low-energy spin-fluctuations will naturally inherit the gauge symmetries of the system via the spin-operators. The existence of gauge symmetry is due to mathematical redundancies in how we represent our RVB states, but they gain physicality due to the constraints imposed by the MF-parameters and the general $SU(2)$ symmetry of spins. Low-energy fluctuations in the ground state correspond to

the exotic quasi-particle excitations that we're interested in. Thus, RVB QSL's—and similar— can be categorized by the 'gauge symmetries' of their low-energy excitations near $T = 0$.

Each type of QSL is physically distinct. $SU(2)$ systems are considered physically unstable due to permitting a large number of gapless fluctuations. They're usually ignored as a possibility. $U(1)$ systems features gapless excitations with a quasi-particle fermi-surface. Theoretically, these surfaces frequently feature Dirac cones. \mathbb{Z}_2 systems inherently have non-trivial topology and feature spinon quasi-particles along with vortex excitations—known as "visions"—that impart Berry curvature onto spinons for anyonic statistics. These are very similar to Kitaev systems, so-much-so that the Kitaev QSL is often referred to as a \mathbb{Z}_2 QSL. In general, the classification scheme of $U(1)$ and \mathbb{Z}_2 is likely valid for a large variety of potential QLS systems, regardless of derivation.

2.4.4 Observables and Predictions of the RVB Model

Obtaining firm theoretical predictions for a numerical theory can be quite challenging due to the non-analytic nature of the problem. Nonetheless, there exist several basic predictions and observables for most QSL states. Both the $U(1)$ and \mathbb{Z}_2 QSL states host spinons as their low-energy quasiparticle excitations.

$U(1)$ QSL's feature gapless spinon excitations, similar to a metal. These spinons are not anyons; they are fermions [5]. Correspondingly, $U(1)$ QSL's are not necessarily topological. Here, the topology is defined by a chern-number in the spinon band structure. Just as with electrons, dirac cones can appear in spinon band-structures resulting in chargeless dirac fermions. More generally, $U(1)$ spin liquids can be modeled as fermi spin-liquids [5]. In particular, there are two simple experimental signatures researchers are looking for: $U(1)$ QSL's have been predicted to host gapped, fractionalized charge excitations in addition to spinons. These charge excitations give rise to signature low temperature AC conductivities of the form $\sigma_{AC}(\omega) \sim \omega^\alpha$, ($\alpha = 2, \sim 3.33$, for $U(1)$ and Dirac $U(1)$, respectively). Similarly, specific heat at low temperatures is expected have a $C \sim T^{2/3}$ contribution to specific heat due to quasi-particle motion. That said: These signatures are relatively weak relative to phonon contributions and only occur at extremely low temperatures. Experimental observation has proven difficult as a result.

\mathbb{Z}_2 states are considered to be more stable than $U(1)$, and are expected to be easier to observe in nature [5]. In \mathbb{Z}_2 models, the electron-spin correlations decay exponentially, while in $U(1)$ the correlations decay as a power-law. \mathbb{Z}_2 QSL's have gapped spinon excitations, which opens them up significantly to scattering techniques. The spinon excitations in \mathbb{Z}_2 models are generically anyonic, and correspondingly \mathbb{Z}_2 states are inherently topological. This is because the \mathbb{Z}_2 states generically host 'gauge flux-vortex-excitations,' which are usually referred to as visions. Visions are a QSL \mathbb{Z}_2 'gauge' analogue of the vortices in type-II superconductors. Unlike magnetic vortices though, the visions are vortices which flip the signs of interaction bonds. If that sounds similar to the Kitaev vortex excitations, that's because it is! Many of

the basic results from the Kitaev model translate to \mathbb{Z}_2 RVB liquids, including the "double-peak" structures in the specific heat due to fractionalization. Note though, they're not identical. For example, the Kitaev model has a gapless region in its phase diagram, and that's the region of interest in the Kitaev model.

Outside of these differences, the bulk properties of RVB and Kitaev systems are similar. They all are correlated paramagnets with fractionalized spin excitations, and they all lack traditional signatures of a thermodynamic transitions.

2.5 Example Materials

Next, we discuss seminal materials in the field of quantum spin liquids. This section is meant to give the reader a flavor of what QSL candidate materials look like in experiments. First, we give a brief review of the most famous QSL system, Herbertsmithite $\text{ZnCu}_3(\text{OH})_6\text{Cl}_2$. Then, we discuss the Kitaev material $\alpha\text{-RuCl}_3$.

Herbertsmithite

The 2D kagome system Herbertsmithite $\text{ZnCu}_3(\text{OH})_6\text{Cl}_2$ and its extended family $\text{Zn}_x\text{Cu}_{4-x}(\text{OH})_6\text{Cl}_2$, has been studied extensively since as a QSL candidate since 2005 [19], [20]. It is considered a paradigm for candidate materials, and it rarely goes without mention in review articles. Entire review articles have been dedicated to it. For now, we simply list several notable attributes and results.

High-temperature magnetic susceptibility gives an antiferromagnetic Curie-Wiess temperature of 300 K . Low-temperature magnetic susceptibility measurements show no indication of ordering or freezing down to 50 mK, giving Herbertsmithite a frustration factor of $f > 6000$. Of course, Herbertsmithite was eventually found to suffer from lattice defects in the form of Cu/Zn sites mixing outside of the kagome plan, and these defects could easily replicate the low-temperature susceptibility. Such issues are common in QSL materials due to the complications of a real system, and the relatively featureless behavior. Muon Spin Rotation (μSR) experiments confirm that there is no magnetic order down to 20 mK, but strangely show a lack of an internal

field at all.⁹

Low temperature specific heat measurements yield a $C_V \sim T^{1.3}$ contribution to the specific heat from the kagome lattice, though the kagome lattices includes Cu2+ site defects which contribute to the specific heat [21]. Prior measurements yielded values as low as $C \sim T^{2/3}$ [22]. Herbertsmithite has been predicted to have a power-law dependence of $C \sim T^\alpha$ where, depending on the paper and applied magnetic field: $\alpha = 2$ or $\alpha(k_B T \ll \mu_0 B) = 1$ [22], or in other models,¹⁰ $\alpha = 2/3$ [23].

Optical conductivity shows a power law of $\sigma(\omega) \sim \omega^2$ [24], which has been predicted for a $U(1)$ Dirac Spin liquids [25] due to virtual charge excitations. Neutron scattering experiments intending to probe the quasi-particle excitation spectrum find a broad-continuum and rules out an excitation gap above to 0.1 meV. Neutron scattering also shows the presence of short-range correlations. All of these properties are consistent with QSL theory, but are also consistent with simpler explanations. A broad excitation spectrum in neutron scattering can easily be due to structural or magnetic impurities, and short-range correlations are found in spin-glassy systems.

α -RuCl₃

α -RuCl₃ is one of the examples of a Kitaev system that doesn't rely on Ir⁴⁺ to achieve frustrated $S_{\text{eff}} = 1/2$. Ruthenium is shifted one row left and one period up from Ir; Ruthenium's 4d orbitals are significantly less affected by SOC than the 5d orbitals of Ir⁴⁺. Moreover, α -RuCl₃ forms Ru³⁺ which has its own ion physics under crystal electric fields (CEF) different from Ir⁴⁺. Yet, the Ru³⁺ ions in α -RuCl₃ form a two-dimensional honeycomb planes that are octahedrally coordinated to Cl with nearly 90° bond angles. The nearly ideal cubic geometry of the CEF allows the SOC effect to win out and create a Kitaev system, similar to the iridates. The result is that α -RuCl₃ is one of the more chemically unique QSL systems. It is also one of the earliest systems that have been heavily studied.

Pure α -RuCl₃ is proximate to a QSL phase under "ambient" conditions. With

⁹Nuclear dipole fields and the like excluded.

¹⁰Clearly, specific heat is not a reliable measure of a QSL.

zero-field, zero-pressure, no doping, or other parameter tuning, α - RuCl_3 zig-zag orders at 8 K with an effective moment of approximately $0.4\mu_B$. The long-range magnetic order can be suppressed by magnetic fields. Magnetization and specific heat show a field-induced transition at 7.5 T, implying a nearby quantum critical point. Neutron diffraction confirm that the transition is to a magnetically disordered states. NMR measurements, which probe spin-excitations through the spin relaxation rate, show $1/T_1 \sim T^3$, which suggests a gapless, Dirac-like, QSL. Thermal conductivity measurements have also been performed and consistent with the presence of Majorana edge modes, though not definitive.

Optical conductivity under applied fields shows a conductivity peak in the region near where one would expect crossover behavior due to quasi-particle fractionalization. That is, T_L . Raman spectra of the scattering intensity shows a peak as a function of ω that qualitatively agrees with Quantum Monte Carlo (QMC) calculations, while failing to fit to spectra calculated using the Bose-Einstein distribution, which usually works well for conventional magnets. Other techniques, such as magnetic torque and ESR have been performed as well. α - RuCl_3 is well studied and listing the results of all experiments lies outside the scope of this paper.

2.6 Conclusions

Quantum spin liquids (QSL)'s are highly non-trivial disordered magnetic phases. QSL's are not conventional thermodynamic phases, and are not described by Landau second order phase transition theory. Classically, one expects a spin frozen state, such as a spin-ice or long-range order at $T = 0$. In a QSL, quantum fluctuations "melt" such a frozen state into a 'liquid' like state at $T = 0$ that has non-vanishing short-range dynamical correlations at $T = 0$.

These states arise from macroscopically sized ground-state degeneracies that result in a non-zero classical entropy at $T = 0$, seemingly in violation of the second law of thermodynamics. This macroscopic entropy results in a phase which features long-range spin entanglement over macroscopic distances, similar to the cooper-pairs of a

superconductor. Correspondingly, we expect exotic spin excitations and physics from a QSL.

QSL's are expected to host, at a minimum, fraction spin and flux excitations that exhibit unconventional anyon statistics under exchange. Other exotic excitations, such as charge fractionalization, are also possible. These exotic states are expected to host anyonic spin excitations which may have technological applications, such as in quantum computers. Understanding QSL states will also advance our knowledge of quantum mechanics and magnetic frustration.

There are many models predicting QSL's, and many systems that may potentially harbor QSLs, but detection is difficult. From the perspective of bulk probes, a QSL appears to be a correlated or quantum paramagnet. In a sense, that is not incorrect. A true test of a QSL would be the long-range entanglement of spins, except there are currently no experimental techniques which can detect long-range entanglement directly. Instead we must rely on a collection of techniques which indirectly probe the QSL phase and form a mosaic of properties consistent with QSL phases.

2.7 Recommended Reading

The interested reader may find the following resources useful:

For a general review of quantum spin liquids:

J. Knolle and R. Moessner, "A Field Guide to Spin Liquids," *Annual Review of Condensed Matter Physics*, vol. 10, no. 1, pp. 451–472, Mar. 10, 2019. DOI: [10.1146/annurev-conmatphys-031218-013401](https://doi.org/10.1146/annurev-conmatphys-031218-013401)

Y. Zhou, K. Kanoda, and T.-K. Ng, "Quantum spin liquid states," *Reviews of Modern Physics*, vol. 89, no. 2, p. 025 003, Apr. 18, 2017. DOI: [10.1103/RevModPhys.89.025003](https://doi.org/10.1103/RevModPhys.89.025003)

For reviews of the Kitaev model:

A. Kitaev, "Anyons in an exactly solved model and beyond," *Annals of Physics*, vol. 321, no. 1, pp. 2–111, 2006. DOI: [10.1016/j.aop.2005.10.005](https://doi.org/10.1016/j.aop.2005.10.005)

Y. Motome and J. Nasu, “Hunting Majorana Fermions in Kitaev Magnets,” *Journal of the Physical Society of Japan*, vol. 89, no. 1, p. 012002, Jan. 15, 2020. DOI: 10.7566/JPSJ.89.012002

For fractionalization and quasiparticles:

M. Hermanns, I. Kimchi, and J. Knolle, “Physics of the Kitaev Model: Fractionalization, Dynamic Correlations, and Material Connections,” *Annual Review of Condensed Matter Physics*, vol. 9, no. 1, pp. 17–33, Mar. 10, 2018. DOI: 10.1146/annurev-conmatphys-033117-053934

2.8 References

- [1] P. Anderson, “Resonating valence bonds: A new kind of insulator?” *Materials Research Bulletin*, vol. 8, no. 2, pp. 153–160, Feb. 1973. DOI: 10.1016/0025-5408(73)90167-0.
- [2] —, “The Resonating Valence Bond State in $\text{La}_2(\text{CuO})_4$ and Superconductivity,” *Science*, vol. 235, no. 4793, pp. 1196–1198, Mar. 6, 1987. DOI: 10.1126/science.235.4793.1196.
- [3] V. Kalmeyer and R. B. Laughlin, “Equivalence of the resonating-valence-bond and fractional quantum Hall states,” *Physical Review Letters*, vol. 59, no. 18, pp. 2095–2098, Nov. 2, 1987. DOI: 10.1103/PhysRevLett.59.2095.
- [4] A. Kitaev, “Anyons in an exactly solved model and beyond,” *Annals of Physics*, vol. 321, no. 1, pp. 2–111, 2006. DOI: 10.1016/j.aop.2005.10.005.
- [5] Y. Zhou, K. Kanoda, and T.-K. Ng, “Quantum spin liquid states,” *Reviews of Modern Physics*, vol. 89, no. 2, p. 025003, Apr. 18, 2017. DOI: 10.1103/RevModPhys.89.025003.
- [6] G. H. Wannier, “Antiferromagnetism. The Triangular Ising Net,” *Physical Review*, vol. 79, no. 2, pp. 357–364, Jul. 15, 1950. DOI: 10.1103/PhysRev.79.357.
- [7] J. J. Sakurai and J. Napolitano, *Modern Quantum Mechanics*, 2nd ed. Boston: Addison-Wesley, 2011, 550 pp., ISBN: 978-0-8053-8291-4.

- [8] M. V. Berry, “Quantal phase factors accompanying adiabatic changes,” *Proceedings of the Royal Society of London. A. Mathematical and Physical Sciences*, vol. 392, no. 1802, pp. 45–57, Mar. 8, 1984. DOI: 10.1098/rspa.1984.0023.
- [9] Z. Nussinov and J. van den Brink, “Compass models: Theory and physical motivations,” *Reviews of Modern Physics*, vol. 87, no. 1, pp. 1–59, Jan. 12, 2015. DOI: 10.1103/RevModPhys.87.1.
- [10] G. Jackeli and G. Khaliullin, “Mott Insulators in the Strong Spin-Orbit Coupling Limit: From Heisenberg to a Quantum Compass and Kitaev Models,” *Physical Review Letters*, vol. 102, no. 1, p. 017205, Jan. 6, 2009. DOI: 10.1103/PhysRevLett.102.017205.
- [11] M. Hermanns, I. Kimchi, and J. Knolle, “Physics of the Kitaev Model: Fractionalization, Dynamic Correlations, and Material Connections,” *Annual Review of Condensed Matter Physics*, vol. 9, no. 1, pp. 17–33, Mar. 10, 2018. DOI: 10.1146/annurev-conmatphys-033117-053934.
- [12] Y. Motome and J. Nasu, “Hunting Majorana Fermions in Kitaev Magnets,” *Journal of the Physical Society of Japan*, vol. 89, no. 1, p. 012002, Jan. 15, 2020. DOI: 10.7566/JPSJ.89.012002.
- [13] C. Broholm, R. J. Cava, S. A. Kivelson, D. G. Nocera, M. R. Norman, and T. Senthil, “Quantum spin liquids,” *Science*, vol. 367, no. 6475, p. 0668, Jan. 17, 2020. DOI: 10.1126/science.aay0668.
- [14] J. Knolle and R. Moessner, “A Field Guide to Spin Liquids,” *Annual Review of Condensed Matter Physics*, vol. 10, no. 1, pp. 451–472, Mar. 10, 2019. DOI: 10.1146/annurev-conmatphys-031218-013401.
- [15] C. Kim, H.-S. Kim, and J.-G. Park, “Spin-orbital entangled state and realization of Kitaev physics in 3d cobalt compounds: A progress report,” *Journal of Physics: Condensed Matter*, vol. 34, no. 2, p. 023001, Jan. 12, 2022. DOI: 10.1088/1361-648X/ac2d5d.

- [16] R. M. Lutchyn, E. P. a. M. Bakkers, L. P. Kouwenhoven, P. Krogstrup, C. M. Marcus, and Y. Oreg, “Majorana zero modes in superconductor–semiconductor heterostructures,” *Nature Reviews Materials*, vol. 3, no. 5, pp. 52–68, 5 May 2018. DOI: 10.1038/s41578-018-0003-1.
- [17] S. D. Sarma, M. Freedman, and C. Nayak, “Majorana zero modes and topological quantum computation,” *npj Quantum Information*, vol. 1, no. 1, p. 15 001, Dec. 8, 2015. DOI: 10.1038/npjqi.2015.1.
- [18] G. Baskaran, S. Mandal, and R. Shankar, “Exact Results for Spin Dynamics and Fractionalization in the Kitaev Model,” *Physical Review Letters*, vol. 98, no. 24, p. 247 201, Jun. 11, 2007. DOI: 10.1103/PhysRevLett.98.247201.
- [19] M. P. Shores, E. A. Nytko, B. M. Bartlett, and D. G. Nocera, “A Structurally Perfect $S = 1/2$ Kagomé Antiferromagnet,” *Journal of the American Chemical Society*, vol. 127, no. 39, pp. 13 462–13 463, Oct. 1, 2005. DOI: 10.1021/ja053891p.
- [20] M. R. Norman, “Colloquium: Herbertsmithite and the search for the quantum spin liquid,” *Reviews of Modern Physics*, vol. 88, no. 4, p. 041 002, Dec. 2, 2016. DOI: 10.1103/RevModPhys.88.041002.
- [21] M. A. de Vries, K. V. Kamenev, W. A. Kockelmann, J. Sanchez-Benitez, and A. Harrison, “Magnetic Ground State of an Experimental $S = 1/2$ Kagome Antiferromagnet,” *Physical Review Letters*, vol. 100, no. 15, p. 157 205, Apr. 17, 2008. DOI: 10.1103/PhysRevLett.100.157205.
- [22] Y. Ran, M. Hermele, P. A. Lee, and X.-G. Wen, “Projected-Wave-Function Study of the Spin-1/2 Heisenberg Model on the Kagomé Lattice,” *Physical Review Letters*, vol. 98, no. 11, p. 117 205, Mar. 16, 2007. DOI: 10.1103/PhysRevLett.98.117205.
- [23] O. I. Motrunich, “Variational study of triangular lattice spin-1/2 model with ring exchanges and spin liquid state in κ -(BEDT–TTF)₂Cu₂(CN)₃,” *Physical Review B*, vol. 72, no. 4, p. 045 105, Jul. 5, 2005. DOI: 10.1103/PhysRevB.72.045105.

- [24] V. R. Shaginyan, V. A. Stephanovich, A. Z. Msezane, *et al.*, “Theoretical and experimental developments in quantum spin liquid in geometrically frustrated magnets: A review,” *Journal of Materials Science*, vol. 55, no. 6, pp. 2257–2290, Feb. 2020. DOI: 10.1007/s10853-019-04128-w.
- [25] A. C. Potter, T. Senthil, and P. A. Lee, “Mechanisms for sub-gap optical conductivity in Herbertsmithite,” *Physical Review B*, vol. 87, no. 24, p. 245 106, Jun. 11, 2013. DOI: 10.1103/PhysRevB.87.245106.

2.9 Figures

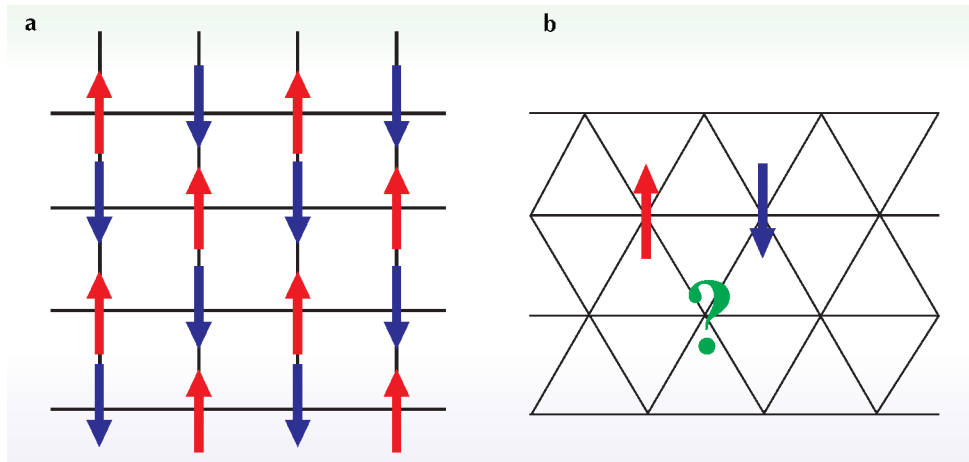


Figure 2-1: Illustration of a geometric frustration for the triangular lattice. (a) A square lattice where all antiferromagnetic interactions can be minimized simultaneously. (b) A triangular lattice where the spin-interactions cannot all be simultaneously minimized. Given a set of three neighboring spins, only two sets of interactions can be anti-aligned. Figure is adapted from “Geometrical Frustration,” by R. Moessner and A. Ramirez, 2006, *Physics Today*, 59(2), 24–29.

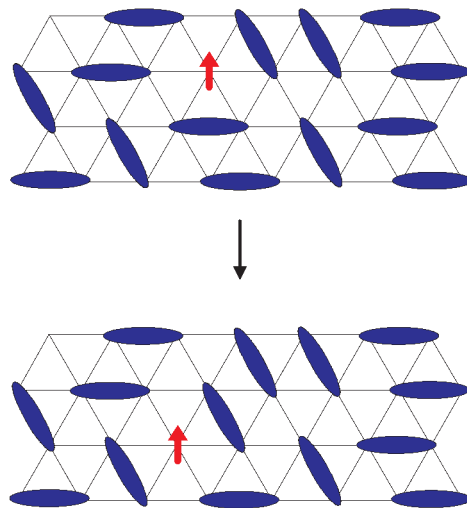


Figure 2-2: Example of degenerate ground-states in a triangular system. In this figure the ground state is, equivalently, represented in terms of anti-aligned spin pairs (blue-ovals) individual unpaired spins (red arrows). In this representation the unpaired spins are spin excitations. This figure is reproduced from “Quantum Spin Liquid States,” by Z. Yi, K. Kanoda, and T. Ng, “2017, *Reviews of Modern Physics*, 89(2):025003.

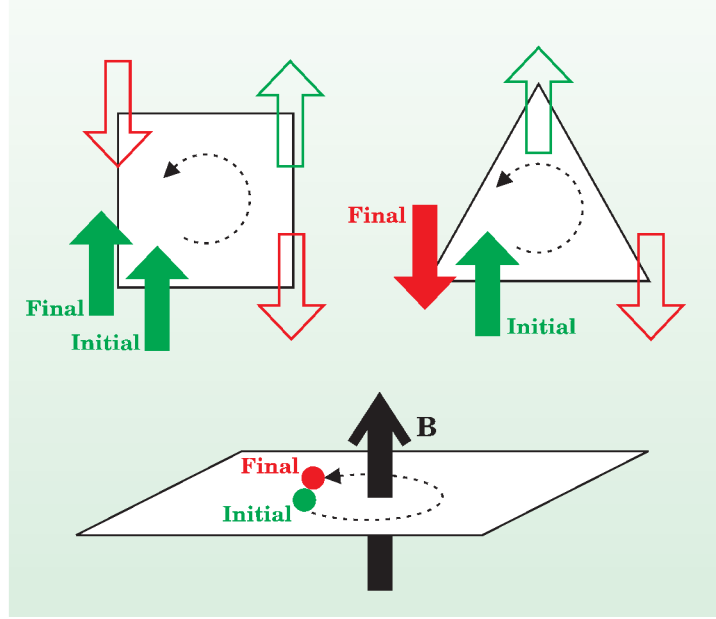


Figure 2-3: A diagrammatic illustration of the topology inherent to the spin triangle due to frustration. Moving an electron around the sites of an AFM square results in a final-state identical to the initial state—as expected. Moving an electron around the sites of a frustrated triangle results in spin-flip. This is a basic example of non-trivial topology. For the $N = 3$ triangle, this can be understood as a variation of the Aharonov-Bohm effect. Figure is reproduced from “Geometrical Frustration,” by R. Moessner and A. Ramirez, 2006, *Physics Today*, 59(2), 24–29.

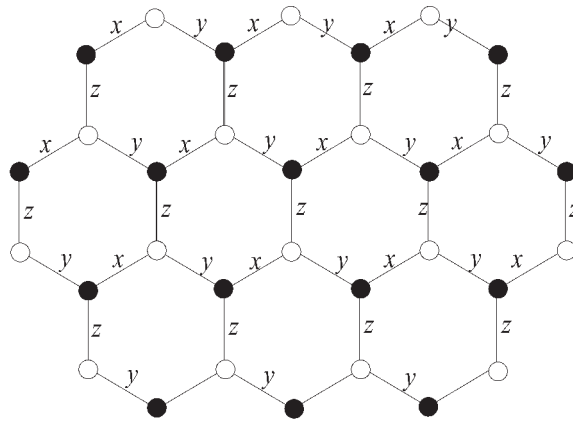


Figure 2-4: Visual representation of the Kitaev honeycomb model. x , y , and z represent each of the three spin interactions, J_x , J_y , and J_z . Reproduced from “Quantum Spin Liquid States,” by Z. Yi, K. Kanoda, and T. Ng, “ 2017, *Reviews of Modern Physics*, 89(2):025003.

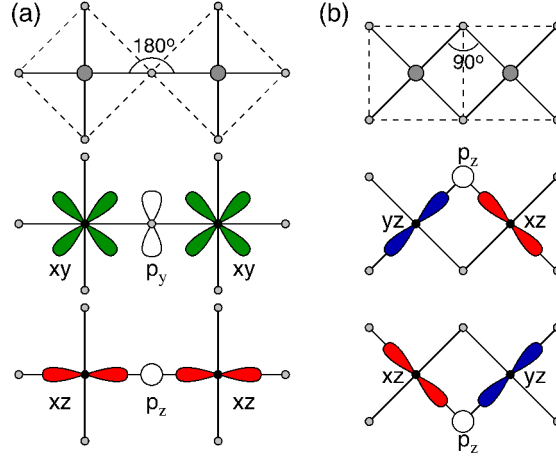


Figure 2-5: Figure and caption reproduced from “Mott Insulators in the Strong Spin-Orbit Coupling Limit: From Heisenberg to a Quantum Compass and Kitaev Models” by G. Jackeli and G. Khaliullin, 2009. *Phys. Rev. Lett.* 102:017205.

Two possible geometries of a TM-O-TM bond with corresponding orbitals active along these bonds. The large (small) dots stand for the transition metal (oxygen) ions. (a) A 180° -bond formed by corner-shared octahedra, and (b) a 90° -bond formed by edge-sharing octahedra.

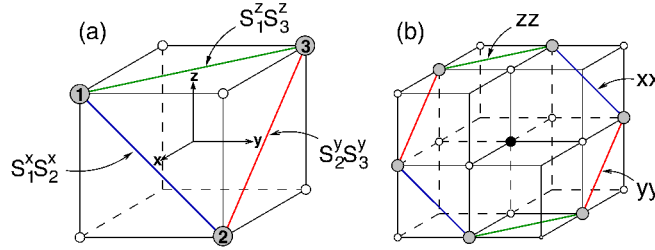


Figure 2-6: Figure and caption reproduced from “Mott Insulators in the Strong Spin-Orbit Coupling Limit: From Heisenberg to a Quantum Compass and Kitaev Models” by G. Jackeli and G. Khaliullin, 2009. *Phys. Rev. Lett.* 102:017205.

Examples of the structural units formed by 90° TM-O-TM bonds and corresponding spin-coupling patterns. Gray circles stand for magnetic ions, and small open circles denote oxygen sites. (a) Triangular unit cell of ABO_2 -type layered compounds, periodic sequence of this unit forms a triangular lattice of magnetic ions. The model (see original text) on this structure is a realization of a quantum compass model on a triangular lattice: e.g., on a bond 1-2, laying perpendicular to x -axis, the interaction is $S_1^x S_2^x$. (b) Hexagonal unit cell of A_2BO_3 -type layered compound, in which magnetic ions (B-sites) form a honeycomb lattice. (Black dot: nonmagnetic A-site). On an xx -bond, the interaction is $S_i^x S_j^x$, etc. For this structure, the model is identical to the Kitaev model.”

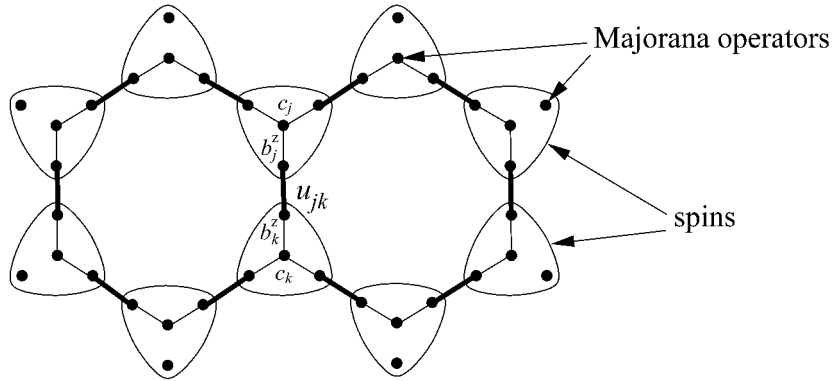


Figure 2-7: Graphical representation of the Kitaev Model Hamiltonian using the Majorana representation. Each spin operator \vec{S}_i is decomposed into four Majorana operators b_j^x , b_j^y , b_j^z , and c_j , with neighboring spins i, k interacting an effective coupling u_{jk} (see text). Reproduced from “Anyons in an Exactly Solved Model and Beyond,” by A. Kitaev, 2006. *Annals of Physics* 321(1): 2–111.

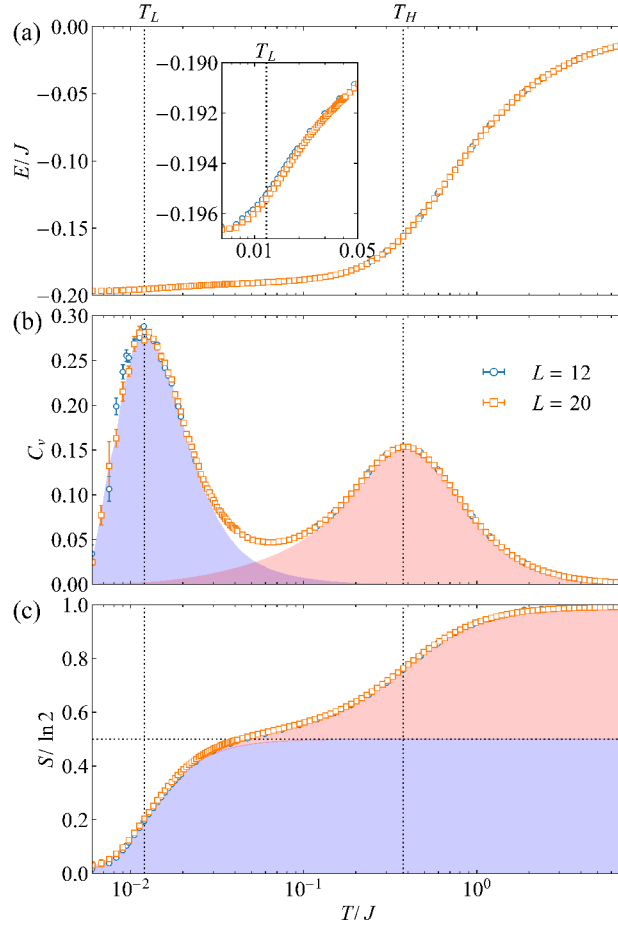


Figure 2-8: Theoretical temperature dependence of the internal energy, specific heat, and entropy, for the Kitaev model with isotropic coupling $J_x = J_y = J_z$. The specific heat shows, on a horizontal log scale, two peaks at characteristic temperatures T_H and T_L . These broad peaks are due to the formation of spinon and flux excitations appearing over two different temperature regimes. Figures are calculated using Quantum Monte Carlo. Further details can be found in the original publication. Reproduced from “Hunting Majorana Fermions in Kitaev Magnets,” by M. Yukiotoshi, and J. Nasu, 2020. *Journal of the Physical Society of Japan* 89(1): 012002.

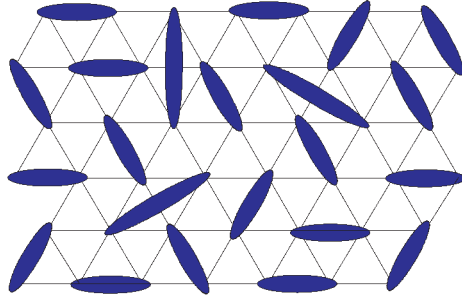


Figure 2-9: A graphical representation of the RVB dimer state. Each blue oval represents a pair of lattice spins coupled together in a spin-1/2 singlet state. Spin pairs do not need to be nearest-neighbors, as shown in the figure. This figure is reproduced from “Quantum Spin Liquid States,” by Z. Yi, K. Kanoda, and T. Ng, “2017. *Reviews of Modern Physics*, 89(2):025003.

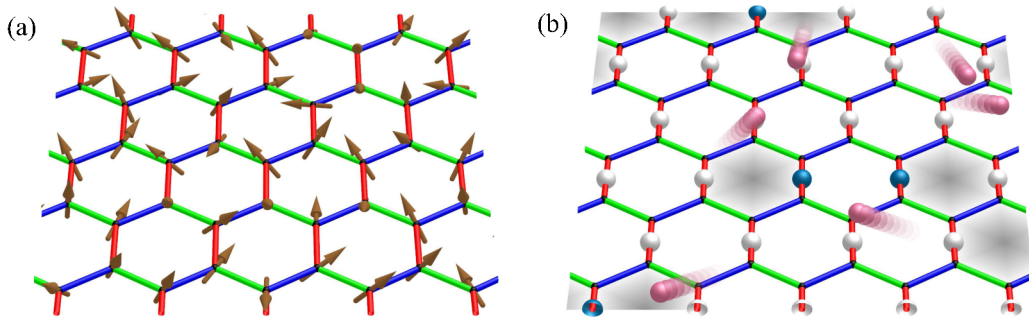


Figure 2-10: Graphical illustration of the Kitaev ground state in (a) the spin representation and (b) the Majorana representation. Red spheres represent spinon excitations. The white and blue spheres represent vortex excitations with quantum numbers ± 1 , respectively. The spinons do not interact directly, but rather interact via non-trivial exchange statistics as they travel around vortex excitations, similar to how an electron gains a phase as it travels around a magnetic field in the Aharonov-Bohm effect. The quantum number of the vortex excitation dictates how the phase of the spinon excitation changes. Reproduced from “Hunting Majorana Fermions in Kitaev Magnets,” by M. Yukiotoshi, and J. Nasu, 2020. *Journal of the Physical Society of Japan* 89(1): 012002.

Chapter 3

μ SR Technique

3.1 Introduction

Muon Spin Rotation, Relaxation, and Resonance (μ SR) is the set of experimental techniques core to this thesis. It is a local-probe probe technique that allows one to characterize the internal field of just about any condensed matter system. μ SR is used extensively in this thesis and in this section I cover the basic theory.

The muon is an unstable sub-atomic particle belonging to the lepton family. The lepton family consists of the electron, muon, and tau particles, along with their corresponding neutrinos. The muon is about 207 times heavier than the electron and has a lifetime of 2.2 μ s. It is nearly identical to the electron otherwise. The muon is a fundamental point-particle with identical spin and electric charge to the electron. The muon comes with a positively charged antiparticle (μ^+). Correspondingly, most of the physics of electrons (and positrons) translates to the muon by simply swapping the muon's mass for that of the electron's.

Most beamlines produce muons via pion (π) decays:

$$\pi^+ \rightarrow \mu^+ + \nu_\mu \tag{3.1.1a}$$

$$\pi^- \rightarrow \mu^- + \bar{\nu}_\mu \tag{3.1.1b}$$

This decay is special because neutrino parity violation ensures that the resulting

muon beam is spin polarized. Neutrinos (ν) and anti-neutrinos ($\bar{\nu}$) all have either right-handed or left-handed helicity, respectively, meaning that their spin is always observed parallel or anti-parallel to their linear momenta.¹ Momentum conservation in the π rest-frame dictates that the muon spin must also be parallel or anti-parallel to the muon's momentum. Therefore the resulting beam of muons is virtually 100 % spin-polarized.

The spin polarization of a muon ensemble can be measured through the weak decay process:

$$\mu^+ \rightarrow e^+ + \nu_e + \bar{\nu}_\mu \quad (3.1.2a)$$

$$\mu^- \rightarrow e^- + \bar{\nu}_e + \nu_\mu \quad (3.1.2b)$$

This decay process famously breaks parity conservation due to the helicity of the neutrinos. The spin of the emitted positron (or electron) is preferentially emitted towards (away) the direction of the muon spin, as shown in figure 3-1. The polarization of the muon ensemble can be deduced by projecting the decay direction along the forward/back directions. Integrating over the distribution reveals that the positron/electron has a 2/3rd probability of decaying at a forward angle, and 1/3rd probability of decaying backwards. Therefore the muon polarization can be deduced by recording the direction of emitted electrons or positrons, which can easily be done using scintillators.

Negative muons act like heavy electrons; this is useful for elemental analysis but is not normally used in conventional μ SR. Instead, most experiments use the positive muon, μ^+ , which behaves like an idealized, light-weight, proton. When implanted into a solid material, the positive muon undergoes a rapid stopping process that preserves the initial muon polarization. Depending on the band-structure of the system, the

¹This is a relativistic effect due to the extremely small mass of the neutrino and the fact they're always observed at ultra-relativistic velocities. Therefore neutrino helicity is functionally independent of reference frame.

muon will usually stop at an interstitial site in the unit cell or form a hydrogen bond.

The process is shown in figure 3-2. The bulk of the implantation process happens on the order of nano-seconds, which negligible compared to the $2.2\ \mu\text{s}$ lifetime of the muon. The muon first sheds kinetic energy via particle collisions. Then, the μ^+ may capture electrons, forming “muonium,” as it continues to slow. The muon will rapidly capture and discard electrons until it nears its minimum energy and stops. From here, what happens depends on the band-structure and elemental composition of the material.

In insulators, the muon may capture an electron and form a hydrogen like quasi-atom known as “muonium”. Muonium behaves like a hydrogen impurity, so the details reflect the physics of hydrogen impurities. This is often employed to study semiconductors. Not all muons may form muonium in an insulator; muons can also fail to capture electrons and instead stop at an interstitial site as described below.

In metals, the muon is unable to form muonium due to the Korringa effect, where conduction electrons screen the muon. The muon, being a point charge, will instead find an electrostatic minimum to stop at. This is usually an interstitial site near an anion in the unit cell, and it is usually a point of high symmetry. A notable exception to this is the oxides, where the muon usually stops approximately $1\ \text{\AA}$ away from an oxygen anion in both metal and insulating oxides. In some materials there may be multiple stopping sites, or even muonium formation in the case of a bad metal or poor insulator. In these cases, the total signal is the sum of the individual signals from each stopping site. This makes μSR a volumetric probe. The volumetric aspect makes μSR useful for studying inhomogenous systems, as the signal is not a weighted average over the bulk.

The simplest use of the muon spin is to measure magnetic field distributions using Larmor precession. Like the electron, the muon undergoes rotation at a fixed angle θ about a magnetic field vector with frequency $f = \frac{\gamma_\mu}{2\pi}|B|$, where γ_μ is the muon gyromagnetic ratio. $\gamma_\mu/2\pi = 13.55\ \text{kHz Oe}^{-1}$. This is an easily detectable frequency range that turns the muon into an exquisitely sensitive magnetometer. The orientation and strength of a single-valued magnetic field can easily be measured from

the amplitude of spin precession and the frequency rotational frequency.

This is the same exact principle as NMR (Nuclear Magnetic Resonance). In NMR one uses RF-field pulses to spin-polarize a small fraction of atomic nuclei whose spins then depolarize according to the internal distribution of magnetic fields and other spin-relaxation processes. In μ SR we instead implant our spins—in the form of muons—directly into the system, and then measure the polarization as a function of time.

μ SR complements other probes quite well due to its unique properties. It is a local probe of the magnetic field that achieves nearly perfect spin polarization without applied magnetic fields. It is sensitive to internal fields as small as 0.1 Oe, and is sensitive to magnetic fluctuations in the range of 10×10^{-10} s to 10×10^{-3} s, depending on the size of the internal fields. Additionally, it is uniquely sensitive to long-range magnetic order.

μ SR experiments are performed at dedicated facilities located around the globe. At the time of writing, there are four facilities capable of performing μ SR:

- Paul Scherrer Institute (PSI) (Villigen, Switzerland)
- The ISIS facility at the Appleton Rutherford Lab (Oxfordshire, England)
- TRIUMF (Vancouver, Canada)
- J-PARC (Tokai, Japan)

The μ SR work in this thesis was performed at PSI and ISIS.

The basic setup for a μ SR experiment is shown in figure 3-3. The sample to be probed is placed between a pair of positron detectors (scintillators). Muons are directed into the sample by the beamline. As muons enter the sample, a timer starts. The muon precesses about the local field in the sample for some time t and then decays into a positron and neutrino pair. The emitted positrons are then detected by the forward and back detectors, and the number of counts on each scintillator is binned relative to the elapsed time t . The result is a pair of histograms, shown in

figure 3-4. The histograms are related to the projected polarization $P_z(t)$ of the muon ensemble as follows:

$$N_F(t) = N_0 \exp(-t/\tau_\mu) \star [1 + a_0 P_z(t)] \quad (3.1.3a)$$

$$N_B(t) = N_0 \exp(-t/\tau_\mu) \star [1 - a_0 P_z(t)] \quad (3.1.3b)$$

N_0 is the number of detected positrons (i.e. muons), $\tau_\mu = 2.2 \mu\text{s}$ is the muon time constant, $P_z(t)$ is the polarization of the muon ensemble projected onto the forward-back detector axis, which we take as the z -axis, and a_0 is an experimental parameter known as the “initial asymmetry.”

The normalization constant N_0 and the exponential decay can be removed by taking the normalized difference between the two:

$$A(t) = \frac{N_F(t) - N_B(t)}{N_F(t) + N_B(t)} = a_0 P_z(t) \quad (3.1.4)$$

$A(t)$ is known as the asymmetry. It is directly proportional to the polarization of the muon ensemble though the initial asymmetry a_0 , which we see now is simply a normalization constant. The value of a_0 is determined by the probability of a positron decaying towards or away from its spin; as previously discussed, this is a 2 : 1 ratio, so the initial asymmetry’s theoretically maximum value is 1/3. Additionally, it is also an experimental parameter that is a function of the detector efficiency and alignment. In practice, the maximum possible value of a_0 is roughly 24 % to 27 %.

The asymmetry of a signal is additive. If muons hit both the sample and the sample holder, one sees a signal with a background contribution:

$$A(t) = A_z(t) + A_{\text{BK}}(t) = a_0(1 - f_{\text{BK}})P_z(t) + a_0 f_{\text{BK}}P_{\text{BK}}(t) \quad (3.1.5)$$

where f_{BK} is the number of detected muons arising from the background (in this case the sample holder), and $P_{\text{BK}}(t)$ is the background polarization. Alternatively, it is possible that some fraction of the muons depolarize faster than the experimental time

resolution and give a zero-signal. In this case, the observed asymmetry is:

$$A(t) = A_z(t) + A_{\text{fast}}(t) = a_0(1 - f_{\text{fast}})P_z(t) \quad (3.1.6)$$

Therefore the observed initial asymmetry may be less than $\sim 25\%$. If a_0 is significantly smaller than 25% , it is known as missing asymmetry and it is treated as an indication that some fraction of the muons are rapidly depolarizing—usually either due to muonium in insulators, or strong magnetism in metals.

3.2 Polarization Functions

μ SR measurements yield the polarization $P(t)$. The polarization can be found by using first principle quantum theory, or by working with semi-classical field distributions. The quantum approach is necessary in systems for which the muon forms muonium by capturing an electron or bonding to the lattice. Since muonium is not relevant for the research presented in this thesis, the quantum theory will not be discussed. Instead, we describe the semi-classical theory of μ SR, which is used for modelling most magnetic systems.

The magnetic spins $\vec{\mathbf{S}}_i$ in a system gives rise to an internal field $\mathbf{B}_{\text{loc}}(\vec{\mathbf{r}})$. For simplicity, we consider the static case where \mathbf{B}_{loc} has no time dependence. When a μ^+ comes to rest in a sample, it will come to rest at one (or more) energetically favorable stopping sites within the unit cell. An individual muon senses its local field, \mathbf{B}_{loc} through Larmor precession (figure 3-5) with angular frequency ω_μ . In an ideal lattice with perfect long-range magnetic order, all muons at a given stopping site will see the same local field and rotate at the same frequency resulting in a sinusoidal polarization $P(t) \sim \cos(\gamma_\mu B_{\text{loc}} t)$. In a real system each muon senses a slightly different local field, which results in spin precession at a different frequency and angle, resulting in a gradual depolarization similar to $T2$ relaxation in NMR. Therefore, we can describe the depolarization of a μ SR signal using a field-distribution method.

Let the muon be initially polarized along the z -axis, and let a given stopping site have a local field distribution $D(\mathbf{B}_{\text{loc}})$. The polarization along the z -axis, in both

cartesian and spherical coordinates, is:

$$P_z(t) = \int \left\{ \left(\frac{B_{\text{loc}}^Z}{B_{\text{loc}}} \right)^2 + \left[1 - \left(\frac{B_{\text{loc}}^Z}{B_{\text{loc}}} \right)^2 \right] \right\} D(\mathbf{B}_{\text{loc}}) dB_{\text{loc}}^X dB_{\text{loc}}^Y dB_{\text{loc}}^Z \quad (3.2.1a)$$

$$P_z(t) = \int \left\{ \cos^2(\theta) + \sin^2(\theta) \right\} D(\mathbf{B}_{\text{loc}}) \star B_{\text{loc}}^2 \sin(\theta) dB_{\text{loc}} d\theta d\phi \quad (3.2.1b)$$

where θ is the polar angle of the local field \mathbf{B}_{loc} and $D(\mathbf{B}_{\text{loc}})$ is the time-independent field distribution seen by the muon ensemble. The polarization function for most elementary magnets can be derived from equations 3.2.1. We will now discuss the fundamental field distributions used in μSR .

Single Field Distribution (Dirac Delta)

Let the muon probe a single field B_0 . The distribution is a Dirac delta distribution: $D(\mathbf{B}_{\text{loc}}; B_0) = \delta^3(\mathbf{B}_{\text{loc}} - B_0)$. The polarization function can easily be read off:

$$P_z(t) = \cos^2(\theta) + \sin^2(\theta) \cos(\gamma_\mu B_0 t) \quad (3.2.2)$$

where θ is the angle the internal field B_0 makes with the z -axis (i.e. the initial muon polarization). This is nothing more than simple Larmor precession.

For a polycrystalline system, we need to average over the field for all possible grain orientations (θ, ϕ) , which yields:

$$P_z(t) = \frac{1}{3} + \frac{2}{3} \cos(\gamma_\mu B_0 t) \quad (3.2.3)$$

Oscillations are seen in simple LRO ordered magnets. If the magnetic unit cell of a LRO system is identical to the crystallographic unit cell, then each stopping site in the unit cell has a well-defined magnetic field for the muons to precess about. Therefore oscillations are a tell-tale sign of long-range magnetic order in μSR . Depolarization of the signal occurs due to magnetic disorder, as will be described next.

Isotropic Gaussian Distribution

Let the components of \mathbf{B}_{loc} be isotropically distributed using a Gaussian distribution with variance Δ_G :

$$\begin{aligned} D(\mathbf{B}_{\text{loc}}) &= D^X(\mathbf{B}_{\text{loc}}^X)D^Y(\mathbf{B}_{\text{loc}}^Y)D^Z(\mathbf{B}_{\text{loc}}^Z) \\ &= \left(\frac{1}{\sqrt{2\pi\Delta_G}}\right)^3 e^{-\frac{1}{2}\left(\frac{B_{\text{loc}}^X}{\Delta_G}\right)^2} e^{-\frac{1}{2}\left(\frac{B_{\text{loc}}^Y}{\Delta_G}\right)^2} e^{-\frac{1}{2}\left(\frac{B_{\text{loc}}^Z}{\Delta_G}\right)^2} \end{aligned} \quad (3.2.4)$$

The resulting polarization function is the famous ‘‘Kubo-Toyabe Function’’:

$$P_z(2) = \frac{1}{3} + \frac{2}{3}(1 - \gamma_\mu^2 \Delta_G^2 t^2) e^{-\frac{\gamma_\mu^2 \Delta_G^2 t^2}{2}} \quad (3.2.5)$$

Note that this function is valid for both single-crystals and polycrystals.

The Kubo-Toyabe function, to good approximation, represents the depolarization arising from densely packed, randomly oriented spins, such as from a frozen paramagnet. The Kubo-Toyabe function is ubiquitous in μSR due to the presence of nuclear dipole moments. Most atomic nuclei have a small magnetic dipole moment that gives rise to a weak background depolarization. For elements with large moments, such as lithium or vanadium, the internal field variances Δ_G can reach up to several Oe, which is easily detectable by μSR . In particular, we often talk about the depolarization rate $\sigma = \gamma_\mu \Delta_G$ which can reach upwards of 1.5 MHz in some cases. More frequently though, nuclear depolarization is closer to 0.1 MHz~0.2 MHz.

Isotropic Lorentzian Distribution

Next, we consider an isotropic Lorentzian distribution with characteristic width Δ_L :

$$D(\mathbf{B}_{\text{loc}}) = \frac{1}{\pi^2} \frac{\Delta_L}{(\Delta_L^2 + B_{\text{loc}}^2)} \quad (3.2.6)$$

The resulting depolarization is an exponential Kubo-Toyabe function:

$$P_z(t) = \frac{1}{3} + \frac{2}{3}(1 - \gamma_\mu \Delta_L t)e^{-\gamma_\mu \Delta_L t} \quad (3.2.7)$$

This field distribution corresponds to the dilute limit of randomly oriented, static, spins. For example, dilute magnetic impurities at low temperature, which freeze into a random, uncorrelated, configuration. Again, we see the famous: “One-third” tail of a static isotropic field distribution. The form here is almost identical to the Gaussian case, except for the power of the terms $\gamma_\mu \Delta_L t$. The general result then, for isotropic, randomly oriented, frozen, spins in a lattice is then as follows:

$$P_z(t) = \frac{1}{3} + \frac{2}{3}(1 - (\sigma t)^\beta)e^{-(\sigma t)^\beta} \quad (3.2.8)$$

where β is a mathematical parameter that depends on the density of the spins, and σ is a characteristic depolarization rate that is proportional to the internal field distribution width. In practice, the exponential can be taken as 2 or 1 unless one is purposefully performing an experiment with large concentrations of impurity spins.

Note that the 1/3 tail appears again. We can show that this is a generic feature of isotropic systems. Let the field distribution $D(B_{\text{loc}})$ be an isotropic field distribution. By definition, and isotropic distribution has no (θ, ϕ) dependence. Therefore equation 3.2.1b simplifies to

$$P_z(t) = \frac{1}{3} + \frac{2}{3} \int_0^\infty 4\pi D(B_{\text{loc}}) B_{\text{loc}}^2 \cos(\gamma_\mu B_{\text{loc}} t) dB_{\text{loc}} \quad (3.2.9a)$$

$$P_z(t) = \frac{1}{3} + \frac{2}{3} \int_0^\infty D_m(B_{\text{loc}}) \cos(\gamma_\mu B_{\text{loc}} t) dB_{\text{loc}} \quad (3.2.9b)$$

$4\pi D(\mathbf{B}_{\text{loc}}) B_{\text{loc}}^2 = D_m(\mathbf{B}_{\text{loc}})$ is the distribution of the magnitude of the local field. It is sometimes referred to as the distribution of the modulus of \mathbf{B}_{loc} . Isotropic field distributions always contain a 1/3 tail—unless the local field distribution is time-dependent, which will be discussed shortly.

So far we have not explicitly included the effect of external fields in our polarization functions. In particular, most of the above distributions yield an average field of zero. We can explicitly include the applied field in the local field distribution $D(\mathbf{B}_{\text{loc}})$. This can be useful for numerical calculations. Or, we can solve for applied field polarization functions separately.

Transverse Fields

Let us apply a magnetic field, \mathbf{B}_{ext} normal to the initial polarization vector and detector axis. For definiteness, let \mathbf{B}_{ext} be along the x -axis. This is known as a “transverse field measurement.” The local field seen by the muon is then the sum of the external field we’ve applied and the internal field inherent to the sample:

$$\mathbf{B}_{\text{loc}} = \mathbf{B}_{\text{ext}} + \mathbf{B}_{\text{int}} \quad (3.2.10)$$

For simplicity, we assume that the internal field distribution is independent of the external field. In this case, the distribution is a function of \mathbf{B}_{int} , and so we can write the local field distribution as $D(\mathbf{B}_{\text{loc}} - \mathbf{B}_{\text{ext}})$. Equation 3.2.1 becomes

$$P_{\text{TF}}(t) = \int \left(\frac{B_{\text{loc}}^Z}{|\mathbf{B}_{\text{loc}} - \mathbf{B}_{\text{ext}}|} \right)^2 + \left[1 - \left(\frac{B_{\text{loc}}^Z}{|\mathbf{B}_{\text{loc}} - \mathbf{B}_{\text{ext}}|} \right)^2 \right] \cos(\gamma_{\mu} |\mathbf{B}_{\text{loc}} - \mathbf{B}_{\text{ext}}| t) D(\mathbf{B}_{\text{loc}} - \mathbf{B}_{\text{ext}}) dB_{\text{loc}}^X dB_{\text{loc}}^Y dB_{\text{loc}}^Z \quad (3.2.11)$$

where $|\mathbf{B}_{\text{loc}} - \mathbf{B}_{\text{ext}}| = \sqrt{(B_{\text{loc}}^X - B_{\text{ext}})^2 + (B_{\text{loc}}^Y)^2 + (B_{\text{loc}}^Z)^2}$, and we label the polarization function P_{TF} for clarity.

In the high-field limit $B_{\text{TF}} \gg \mathbf{B}_{\text{int}}$, the above simplifies to:

$$P_{\text{TF}}(t) \approx \left[\int_{-\infty}^{\infty} D^Z(B_{\text{int}}^Z) \cos(\gamma_{\mu} B_{\text{int}}^Z t) dB_{\text{int}}^Z \right] \cos(\gamma_{\mu} B_{\text{ext}} t) \quad (3.2.12)$$

where D^Z is the field-distribution for the z-component of the internal field.² Thus, in the high-field limit, the “transverse field polarization” function is a cosine oscillation about zero polarization with angular frequency $\gamma_{\mu} B_{\text{ext}}$, multiplied by a depolarizing

envelope dependent only on the one-dimension field distribution along $\hat{\mathbf{x}}$.

For a Gaussian distribution, one obtains a Gaussian depolarization:

$$P_{\text{TF}}(t) = e^{-\frac{\gamma_{\mu}^2 \Delta_G^2 t^2}{2}} \cos(\gamma_{\mu} B_{\text{ext}} t) \quad (3.2.13)$$

For the Lorentzian distribution, one obtains an exponential (or Lorentzian) decay:

$$P_{\text{TF}}(t) = e^{-\gamma_{\mu} \Delta_L t} \cos(\gamma_{\mu} B_{\text{ext}} t) \quad (3.2.14)$$

And, for the generalized randomly oriented spin-frozen case:

$$P_{\text{TF}}(t) = e^{-(\sigma t)^{\beta}} \cos(\gamma_{\mu} B_{\text{ext}} t) \quad (3.2.15)$$

where $e^{-(\sigma t)^{\beta}}$ is often referred to as the ‘‘Stretched exponential function.’’

For a single field, the approximation above isn’t necessary and one can easily write down

$$P_{\text{TF}}(t) = \cos^2(\theta) + \sin^2(\theta) \cos(\gamma_{\mu} B_{\text{loc}} t) \quad (3.2.16)$$

where $B_{\text{loc}} = \sqrt{(B^X + B_{\text{ext}})^2 + (B^Y)^2 + (B^Z)^2}$ and $\theta = \cos^{-1}(B_{\text{loc}}^Z / B_{\text{loc}})$. The polycrystal case is obtained by averaging (θ, ϕ) over a 4π solid angle. The interested reader may consult any dedicated textbook on the subject for more details.

We see that there are several unique advantages to the transverse field function compared to the zero-field case. There is no ‘‘tail’’ in the transverse field case—transverse field measurements are routinely used for data calibration for this reason. The depolarization is also simplified, yielding simple decay envelopes. Additionally, only magnetic disorder along the external field axis contributes to the depolarization. This makes the TF configuration ideal for anisotropic systems and orientation depen-

² $D(\mathbf{B}_{\text{loc}})$ is a vector distribution, while $D^Z(\mathbf{B}_{\text{loc}}^Z)$ is a component distribution. In simple cases, $D(\mathbf{B}_{\text{loc}}) = D^X(\mathbf{B}_{\text{loc}}^X) D^Y(\mathbf{B}_{\text{loc}}^Y) D^Z(\mathbf{B}_{\text{loc}}^Z)$. Therefore we use D^{α} for clarity.

dent measurements. The trade-off is, off course, is that one needs to either know the sample's field response, or assume that the local susceptibility of the system is linear.

Longitudinal Fields

Applying the field parallel to the initial spin-polarization and measurement axis is known as a “longitudinal field” (LF) measurement. Unlike the transverse case, the longitudinal case has little in the way of simplifications like equation 3.2.12. Instead, LF polarization functions tend to be non-analytic. That said, LF have some predictable properties that can be extremely useful.

Referring back to equation 3.2.3, the amplitude of the oscillations for a single field depend on the angle the local field makes with the muon spin. If the field is parallel to the muon spin, then no precession occurs. Therefore if the longitudinal field is much greater than the internal fields, $B_{\text{LF}} \gg \mathbf{B}_{\text{int}}$, the longitudinal field depolarization function asymptotically approaches $P_{\text{LF}}(t) \approx 1$, and the muon's polarization is decoupled from the internal magnetic disorder.

As an example, for a single field magnet with an internal field with magnitude B_0 and angle θ_0 . The polarization function is identical to function 3.2.16, except now $\mathbf{B}_{\text{loc}} = \sqrt{(B^X)^2 + (B^Y)^2 + (B^Z + B_{\text{ext}})^2}$. The non-oscillating tail can be solved for terms of B_0 and θ_0 . Letting $\mathbf{B}_{\text{ext}} \equiv \mathbf{B}_{\text{ext}}/B_0$

$$f_{\text{tail}} = \frac{(\cos \theta_0 + B_{\text{ext}})^2}{\sin^2 \theta_0 + (\cos \theta_0 + b_{\text{ext}})^2} \quad (3.2.17)$$

Surprisingly, an analytical formula exists for the polycrystal case:

$$f_{\text{tail, powder}} = \frac{3}{4} - \frac{1}{4b_{\text{ext}}^2} + \frac{(b_{\text{ext}}^2 - 1)^2}{16b_{\text{ext}}^3} \ln \left[\frac{(b_{\text{ext}} + 1)^2}{(b_{\text{ext}} - 1)^2} \right] \quad (3.2.18)$$

In both equations, one sees that oscillation amplitude is suppressed by longitudinal fields.

In practice, most internal field distributions have field dependencies similar to figure 3-6. Thus, longitudinal fields allow one to estimate the magnitude of the

internal fields in a sample, even when no oscillations are present and or the analytical form of the depolarization is unknown.

This assumes that the local fields are static. So far we've ignored the possibility of spin-fluctuations, muon site-hopping, or other dynamical processes that may depolarize the muon besides a static field distribution. While dynamics will be discussed in more detail later, it is worth noting here that the longitudinal field function is highly sensitive to dynamical processes. In most cases, the presence of dynamical processes will severely reduce the efficacy of longitudinal fields for lifting the tail. Moreover, dynamical processes will introduce an exponential decay into the LF tail that cannot be fully suppressed by longitudinal fields.

Thus, longitudinal fields truly excel at estimating and measuring dynamical processes, such as spin-lattice relaxation rates. As a rule of thumb, a static depolarization should be near-fully suppressed when $B_{\text{LF}} \gtrsim 10 \sigma / \gamma_{\mu}$, where σ is the characteristic depolarization rate associated with a given polarization function. The energy scales associated with most dynamical processes are much higher than the Zeeman energy associated with an LF field, so for most dynamical systems one will require fields of 10x to 100x, higher, or more, to suppress the depolarization. Therefore in a typical μSR experiment, one will usually take at least a few LF spectra in order to test for appreciable dynamics, and to estimate the internal field strength if the system is static.

Combination of Fields

Usually the local field distribution is best described as multiple independent field distributions. For example, a realistic ordered magnet can often be modeled as a single field distribution (Dirac delta) due to the long-range order, superimposed onto a Gaussian distribution due to random imperfections in LRO spin orientation. Or, sometimes you might have two species of spins, such as lattice spins and impurity spins. Either way, if the two field distributions are statistically independent, the net

field distribution is the convolution of the two:

$$D(\mathbf{B}_{\text{loc}}) = D_1 * D_2(\mathbf{B}_{\text{loc}}) \equiv \int D_1(\mathbf{B}'_{\text{loc}}) D_2(\mathbf{B}_{\text{loc}} - \mathbf{B}'_{\text{loc}}) d^3\mathbf{B}'_{\text{loc}} \quad (3.2.19)$$

In general, convolutions tend to be tricky to perform—especially for vector distributions. In special cases we can avoid calculating the convolution altogether. For high-transverse field measurements, equation 3.2.12 has the form of a Fourier Cosine transform.

$$F_c[f](\alpha) \equiv \frac{1}{\pi} \int_{-\infty}^{\infty} f(x) \cos(\alpha x) \quad (3.2.20)$$

By identifying equation 3.2.12 as a convolution, we can use the convolution theorem:

$$F_c[f * g] = F_c[f] \cdot F_c[g] \quad (3.2.21)$$

The Fourier transform of the convolution product is simply the product of the two individual Fourier transforms. Therefore for high-transverse fields, the polarization function of two statistically independent field sources:

$$P_{\text{TF}}(t) = P_{\text{TF},1}(t) P_{\text{TF},2}(t) \cos(\gamma_{\mu} B_{\text{ext}} t) \quad (3.2.22)$$

where $P_{\text{TF},1/2}(t)$ are the transverse field depolarization functions. For example, let us have a magnetically disordered lattice with nuclear dipole moments. The TF polarization function is:

$$P_{\text{TF}}(t) = e^{-\frac{\gamma_{\mu}^2 \Delta_e^2 t^2}{2}} e^{-\frac{\gamma_{\mu}^2 \Delta_N^2 t^2}{2}} \cos(\gamma_{\mu} B_{\text{ext}} t) = e^{-\frac{(\Delta_e^2 + \Delta_N^2) \gamma_{\mu}^2 t^2}{2}} \cos(\gamma_{\mu} B_{\text{ext}} t) \quad (3.2.23)$$

Two Gaussian depolarizations combine into a single Gaussian depolarization with depolarization rate $\gamma_{\mu}(\Delta_e^2 + \Delta_N^2) = \gamma_{\mu} \Delta^2$, where Δ_N is the nuclear contribution, and Δ_e is the electronic contribution.

Another example: For the case of a static disordered lattice with dilute static

impurities, one obtains

$$P_{\text{TF}}(t) = e^{-\frac{\gamma_{\mu}^2 \Delta^2 t^2}{2} + \gamma_{\mu} \lambda t} \cos(\gamma_{\mu} B_{\text{ext}} t) \quad (3.2.24)$$

Similarly, the isotropic zero-field equation in equation 3.2.9b also is a Fourier Cosine transform, except distribution is of the magnitude of \mathbf{B}_{loc} instead of $D^Z(B_{\text{int}}^Z)$. For the Gaussian and Gaussian + Lorentzian cases, the results can be easily written down by the reader.

3.3 Dynamics

As the final topic, we discuss dynamical processes. So far we've assumed that the local field distribution $D(\mathbf{B}_{\text{loc}})$ is independent of t . This is never truly the case in a real system though. Spin fluctuations, site hopping, spin-lattice relaxation, and other more exotic processes can cause the local field to fluctuate over the muon-lifetime. Such processes are collectively referred to 'dynamics' in μSR .

Strictly speaking, how one deals with dynamics mathematically depends on the details of the process. Thankfully, most dynamical processes in μSR are well-described by the 'strong-collision' model of μSR . In this model, each muon in the ensemble may randomly resample the static internal field distribution $D(\mathbf{B}_{\text{loc}})$ with an ensemble average rate ν . The polarization function can be derived as:

$$P(t) = P^{\text{stat}}(t)e^{-\nu t} + \nu \int_0^t P(t-t')P^{\text{stat}}(t')e^{-\nu t'} dt' \quad (3.3.1)$$

where $P^{\text{stat}}(t)$ is the static depolarization function when $\nu = 0$. Notice that $P(t)$ appears on both sides of this equation. This is an implicit equation, which is generally not tractable by itself. It can be simplified though by using a Laplace transform:

$$P(s) = \frac{P^{\text{stat}}(s + \nu)}{1 - \nu P^{\text{stat}}(s + \nu)} \quad (3.3.2)$$

The equation is no longer implicit, but now we have to deal with multiple Laplace

transforms. It only explicitly depends on ν , which is a characteristic fluctuation rate from the assumption of a hard-collision model, and P^{stat} . Since P^{stat} is a physical observable, this means that most dynamical processes have generic effects on the polarization spectra of a system, regardless of the underlying microscopic details. The only conditions are that the resampling process has to be sufficiently faster than the resampling rate ν , and that the resampling of D must be sufficiently uniform.

We now provide some basic results for different regimes of ν . For definiteness, we consider the isotropic Gaussian distribution in equation 3.2.4, which gives asymptotic solutions.

In the "fast-fluctuation limit" $\nu \gg \gamma_\mu \Delta_G$:

$$P_Z(t) \approx \exp\left(-2\gamma_\mu^2 \Delta_G^2 \frac{t}{\nu}\right) \quad (3.3.3)$$

If the dynamics are sufficiently fast, the polarization function changes from the Gaussian Kubo toyabe function in equation 3.3.7 to an exponential function, with a depolarization rate proportional to Δ_G^2/t . Thus, rapid fluctuations suppress depolarization by a temporal averaging of the internal field distribution seen by the muon ensemble. Interestingly, an exponential decay is also what's seen for dilute magnetic impurities

For dilute magnetic impurities, the field distribution is Lorentzian and the polarization function becomes

$$P_Z(t) \approx \exp\left(-2\sqrt{\gamma_\mu^2 \Delta_G^2 \frac{t}{\nu}}\right) \quad (3.3.4)$$

which is known as the root-exponential function. Thus, for rapid fluctuations one sees the elimination of the 'static 1/3 tail,' and a reduction to $P_Z(t) \approx \exp(-(\sigma t)^\beta)$ where $\beta \sim 1/2$ to 1. To distinguish between a dynamical Gaussian and a static Lorentzian in the slow depolarization limit, (where $P(t \rightarrow \infty)$ is not captured by the spectra) one can apply an LF field. For $\nu \gg \gamma_\mu \Delta_G$ the Gaussian distribution yields:

$$P_{\text{LF}}(t) \approx \exp \left(-2\gamma_{\mu}^2 \Delta_G^2 \frac{\nu}{\gamma_{\mu}^2 B_{\text{ext}}^2 + \nu^2} t \right) \quad (3.3.5)$$

The depolarization remains exponential with no tail if the fluctuations are sufficiently fast. Also, the depolarization rate scales as $\sim 1/B_{\text{ext}}^2$ in the extreme dynamical case, when the depolarization rate is independent of B_{ext} in the static case.³

In the Quasi-static limit ($\nu \rightarrow 0$), the Gaussian distribution yields a modified Kubo-Toyabe function:

$$\frac{1}{3} e^{-\frac{2}{3}\nu t} + \frac{2}{3} (1 - \gamma_{\mu}^2 \Delta_G^2 t^2) e^{-\frac{\gamma_{\mu}^2 \Delta_G^2 t^2}{2}} \quad (3.3.6)$$

Interestingly, in the slow fluctuation limit the static depolarization function is unaffected by the fluctuations. Rather, slow dynamics results in a slow exponential decay of the $1/3$ tail that only depends on ν . In practice, the rate is usually around $\sim 0.1 \mu\text{s}^{-1}$ to $0.01 \mu\text{s}^{-1}$ in experiments. This is actually a generic feature of dynamics. For any polarization function in the quasi-static limit,

$$P(t) = (1 - f_{\text{tail}}) G^{\text{osc.}}(t) + f_{\text{tail}} e^{-\alpha \nu t} \quad (3.3.7)$$

where $G^{\text{osc.}}(t)$ is the oscillation or decay of the function in the static case, and f_{tail} is the tail fraction which equals $1/3$ for the isotropic case, and α is a numerical constant that equals $2/3$ for the isotropic case.

Notice that the slow depolarizations of the tail towards zero does not depend on field. Since a longitudinal field measurement is a form of a static field distribution in of itself, and the above does not rely on the distribution being isotropic. Equation 3.2.1 applies just as well in the LF case. So, in the quasi-static limit, one observes a static depolarization function with a slowly decaying tail. Under LF fields, the decay is approximately field independent.

Thus, we see that μSR is highly sensitive to any dynamical process that affects

³In the static case only the amplitude of the decay changes while the rate remains the same.

the local field of the muon site, and that the effect is highly generic. Moreover, the LF technique can distinguish between static and dynamic systems, and measure characteristic dynamical rates. This ability is one of the reasons why μ SR is prized in the field of frustrated magnetism, as it is a highly sensitive probe of local magnetic fluctuations, and can discriminate between spin-frozen and dynamical ground states.

3.4 Usage of μ SR in Quantum Spin Liquid research

μ SR's sensitivity to magnetic disorder and dynamics on the unit-cell level makes it an excellent probe to search for QSL's. Long-range magnetic order and spin-freezing are both easily discernable through routine μ SR measurements, which can reveal critical information that can be missed by other probes such as neutron scattering or magnetic susceptibility. It is standard practice to measure any promising QSL system with muons to confirm that the ground state is a potential QSL state.

The caveat is that μ SR cannot prove that a system is a QSL; μ SR can only prove if a system isn't a QSL. This is because the muon cannot probe long-range entanglement directly, and that entanglement is the defining feature that distinguishes a QSL from a correlated paramagnet.

That said: To my knowledge, there has never been a detailed theory of μ SR in QSL systems despite its widespread use. My understanding is that evaluating the polarization function of the muon in the QSL state is a highly non-trivial task. Obviously, the semi-classic field distribution method would be insufficient, and one would need to use fully quantum methods to evaluate the polarization function. Given that most QSL theories are numerical, with the few analytical theories having highly non-trivial solutions, finding $P(t)$ would be quite difficult.

Yet, μ SR is widely employed anyways because there are still generic observations one expects given the broad details. At heart, QSL's are paramagnets with a paramagnetic magnetic susceptibility. Paramagnets, correlated or otherwise, have simple spectra. One expects an exponential depolarization in the fast-fluctuation limit. If the quantum fluctuations are too slow for this, there are analytic approximations

for both the intermediate and slow fluctuation limits. Moreover, the characteristic fluctuation rate can be measured directly in multiple ways using both longitudinal and zero-field measurements. Note that Inelastic neutron scattering measurements and similar scattering techniques measure excitations; they do not measure not fluctuations directly. Additionally, the curvature and shape of the polarization function also gives information about the source of the depolarization; densely packed spins yield different shapes than dilute impurity spins.

Thus, μ SR can easily rule out systems that appear to be QSL's by other probes. If a spectra shows any form of oscillation, it is not a QSL. If it has a root-square depolarization or a Gaussian depolarization, it is not a QSL. If LF measurements show a lack of appreciable dynamics, it is not a QSL. For a system to be a QSL, the spectra needs to correspond to densely packed magnetic moments with some level of dynamics, and short-range correlations at most. And if a system is not a QSL, then μ SR will yield useful information about what the ground state is and its transition. Incommensurate long-range order yields spectra distinct from commensurate order. Spin glasses, spin-ice, and spin-frozen systems have differing spectra. Meanwhile, μ SR is sensitive enough to observe critical slowing, which can assist in diagnosing a thermodynamic transition if necessary. Thus, μ SR not only can rule out or elevate a QSL candidate, but it can also play a crucial role in explaining why a system fails to be a QSL.

3.5 Bibliography

- Le Yaouanc, A., De Réotier, P.D., 2010. *Muon spin rotation, relaxation, and resonance: applications to condensed matter*. Oxford University Press, Oxford.
- Lee, S.L., Kilcoyne, S.H., Cywinski, R. (Eds.), 1999. *Muon science: muons in physics, chemistry, and materials*. Scottish Universities Summer School in Physics & Institute of Physics Pub, Philadelphia, PA.
- Nagamine, K., 2003. *Introductory muon science*. Cambridge University Press, Cambridge; New York.

Schenck, A., 1985. *Muon spin rotation spectroscopy: principles and applications in solid state physics*. A. Hilger, Bristol; Boston.

3.6 Figures

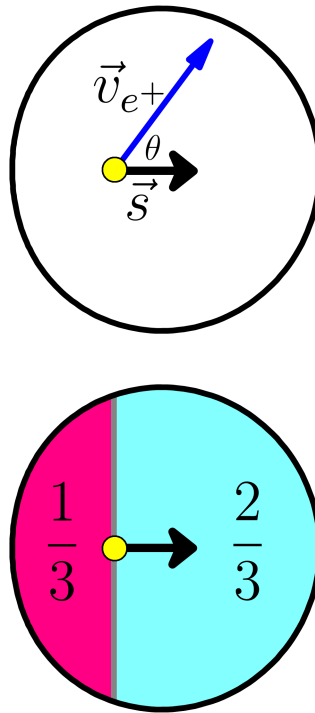


Figure 3-1: The emission angle of the positron in the muon's weak-decay reaction $\mu^+ \rightarrow e^+ + \nu_e + \bar{\nu}_\mu$ follows a cosine function: $P(\theta) d\theta \sim 1 + 1/3 \cos \theta d\theta$. This equation assumes that the muon is at rest before decay, and it is averaged over the positron emission's energy spectra. Integrating over the distribution reveals that the positron's final velocity \vec{v}_{e^+} has a 2/3 probability of emitting towards the muon spin \vec{S} direction points, and a 1/3 probability of emitting away from the spin direction.

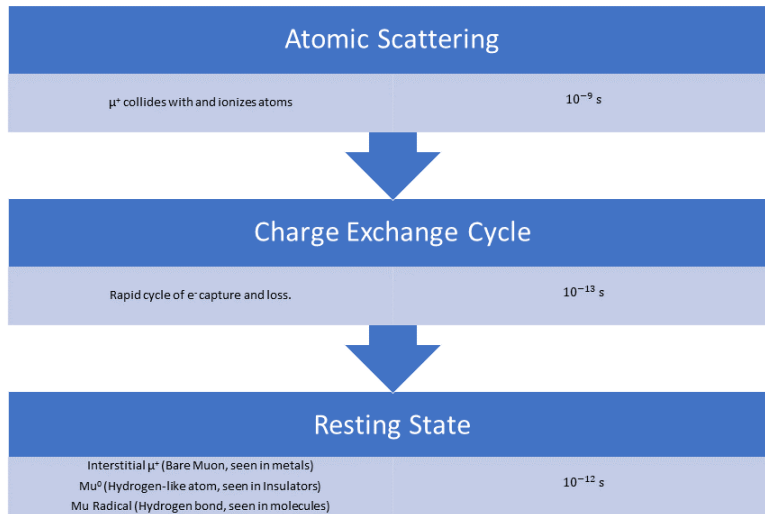


Figure 3-2: Diagram of the muon stopping process. When the muon first enters a sample, it rapidly slows down due to ionizing collisions with atoms, a process which occurs on the order of 1×10^{-9} s. Once the muon is moving too slowly to ionize atoms, it sheds further energy by rapidly capturing and releasing electrons. This is a fast process on the order of 1×10^{-13} s. Once the charge cycle ends, the muon rapidly comes to rest in one of several configurations. In metals, the muon is unable to capture an electron permanently due to shielding from the conduction electrons, and instead behaves as a bare muon which settles into an interstitial lattice site. In insulators, the muon instead tends to capture an electron and form the quasi-element "muonium" (Mu^0). In molecular systems, the muon acts as a hydrogen radical and forms H-bonds with the molecule. In some systems, a combination of final states may occur where some fraction of the muons stop at an interstitial site while another fraction may form muonium or bond with the lattice.

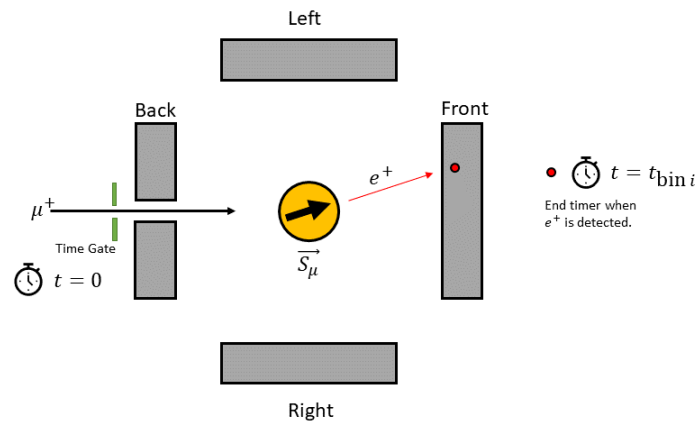


Figure 3-3: Diagram illustrating a basic μ SR setup. A beam of spin-polarized muons enters the system—often through a hole in the backwards detector. The muons implant into the sample, where their spins either undergo Larmor precession or depolarize. After some time passes, individual muons decay into positrons, which preferentially emit along the spin-direction. The positron is detected by pairs of scintillators surrounding the sample. A time gate records when the muon (or muons) enter the sample, and the scintillator records when the positron is detected. The detection events are recorded and binned according to the elapsed time between entry and exit.

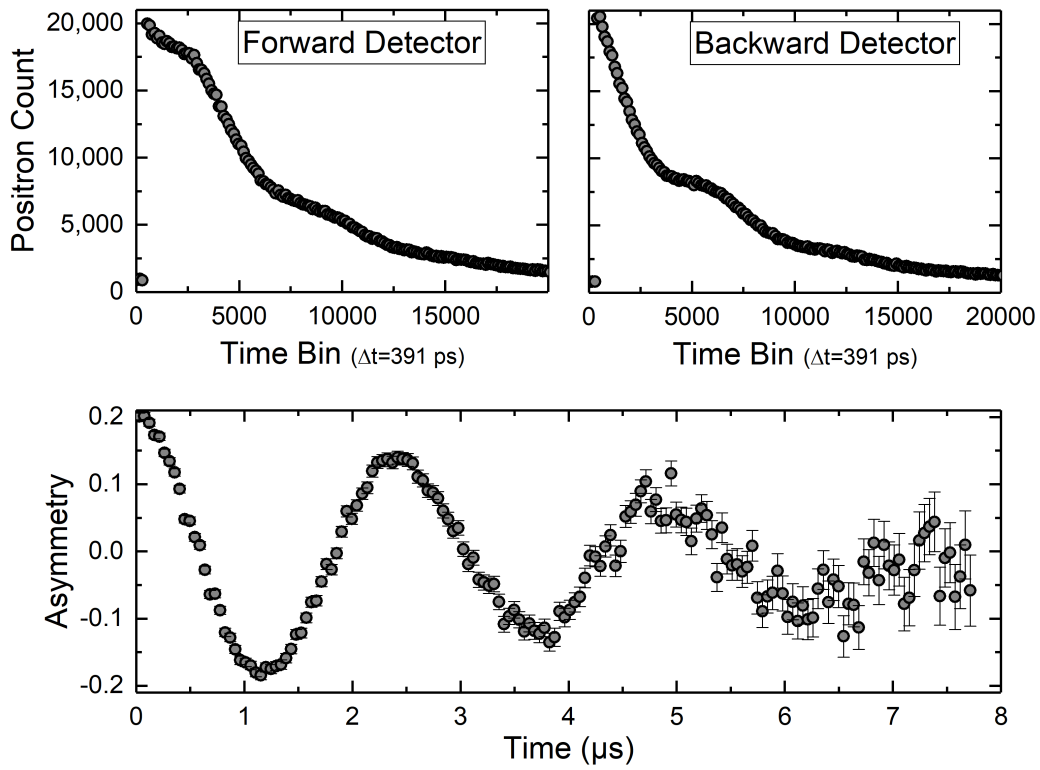


Figure 3-4: Example μ SR spectra. (Top) Histograms of a Forward-Back pair showing positron counts as a function of time for a paramagnetic system with 0 Oe transverse field (TF) applied. Bin width is 1 ps. The exponential decay is a result of the 2.2 μ s muon lifetime (Bottom) The two histograms above combined into a single asymmetry spectra. The asymmetry is proportional to the polarization of the muon assemble.

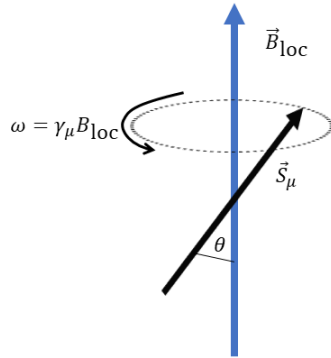


Figure 3-5: The muon precesses about the local field with angular frequency $\omega = \gamma_\mu \mathbf{B}_{\text{loc}}$.

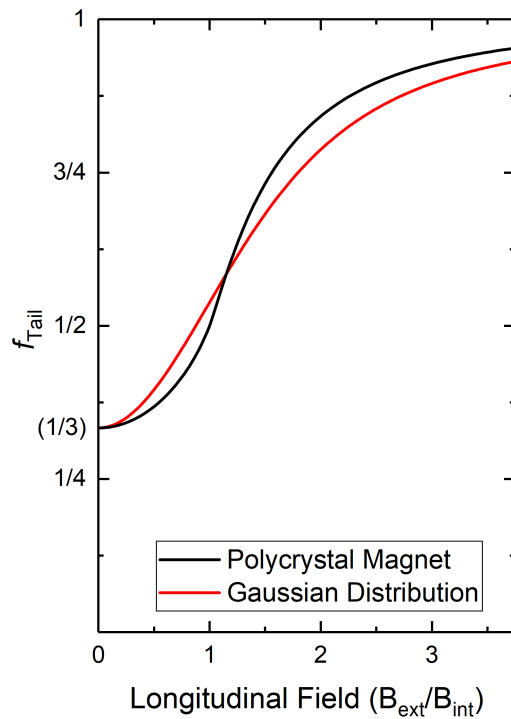


Figure 3-6: Field dependence of the static tail under longitudinal fields. The black line shows the dependence of a long-range ordered polycrystal with a single field. The red line shows the field dependence of an isotropic Gaussian distribution.

Chapter 4

Frustrated Magnetism in NaYbO_2 and LiYbO_2

Key Publications

*Field-Tunable Quantum Disordered Ground State in the
triangular-lattice antiferromagnet NaYbO_2
Nature Physics, Oct. 2019.*

*Frustrated Heisenberg $J_1 - J_2$ Model within the stretched diamond Lattice of LiYbO
Physical Review B, Jan. 2021.*

*Novel magnetic ordering in LiYbO_2 probed by muon spin relaxation
Manuscript under review (Physical Review B)*

4.1 Introduction

Finding geometrically frustrated $S = 1/2$ systems is one of the largest hurdles in studying quantum spin liquids (QSL). Spin-1/2 naturally maximizes the effects of the quantum fluctuations which disrupt traditional long-ranged ordered states into disordered QSL states [1], [2]. As the spin approaches the classical $S \rightarrow \infty$ limit [3], the system either magnetically orders [2] or becomes a classical spin liquid [4]. For certain geometries, such as the triangular lattice, it may not be possible to realize a QSL state for $S > 1/2$ [1].

The first generation of QSL candidates were typically complicated systems with many atoms per unit cell and complex electron interactions. For example, the first highly promising QSL candidate was the kagome system Herbertsmithite, $\text{ZnCu}_3(\text{OH})_6\text{Cl}_2$ [5]. For triangular lattices, researchers relied on organic molecular magnets [3] such as κ -(BEDT-TTF) $_2\text{Cu}_2(\text{CN})_3$ and $\text{EtMe}_3\text{Sb}[\text{Pd}(\text{dmit})_2]_2$ both of which have dozens of atoms per unit cell, and effective spins spread over molecular structures. The materials used in the first generation of QSL research frequently suffered from higher-order interaction effects, structural distortions, and in some cases, ambiguous data [3], [6]–[8]. The need for simple inorganic spin-1/2 structures was clear. And so our collaborators, the Wilson Group in Santa Barbara, synthesized NaYbO_2 and LiYbO_2 as potential QSL systems.

The AYbO_2 ($A = \text{Alkali}$) family forms a variety of magnetically frustrated structures, such as the layered triangular lattice in NaYbO_2 (figure 4-1) or the three-dimensional diamond structure of LiYbO_2 (figure 4-7). In these systems Yb is octahedrally coordinated with Oxygen, forming Yb^{3+} valence states with $J_{\text{eff}} = 1/2$ due to a combination of spin-orbit coupling and crystal field splitting [9]–[11]. Therefore the AYbO_2 allows a systematic study of several frustrated geometries with effective spin-1/2 by changing the Alkaline atom used.

In this chapter we describe our measurements on NaYbO_2 and LiYbO_2 which were performed in collaboration with the Wilson Group [9], [11]. In NaYbO_2 we use AC magnetic susceptibility to uncover a magnetic field induced quantum critical

point in a system that does not order or freeze down to 50 mK. For LiYbO_2 , we used AC susceptibility [11] and μSR to characterize the local internal field of an unusual “phase-disordered” bipartite helical system. For both systems we present a simplified version of the models used to analyze these systems. For their models, we compare our results with theoretical expectations. Additionally, I propose a toy model for interpreting LiYbO_2 ’s μSR data between 450 mK and 1.1 K.

The effects of our research in this chapter are clear. Within two years we have received over 100 citations of our work on NaYbO_2 . For LiYbO_2 , one manuscript has been published while another is still under review. To my knowledge our theory of μSR in LiYbO_2 is original and represents a new contribution to the field of μSR analysis.

4.2 NaYbO_2

4.2.1 Characterization NaYbO_2

Our AC magnetic susceptibility measurements were complimented by several measurements performed by our collaborators, including specific heat and neutron diffraction. We briefly discuss these results which can be found in more detail in our original publication [9].

Powder neutron diffraction was used to refine both the magnetic and crystalline structures of NaYbO_2 and to check Na ion stoichiometry. NaYbO_2 forms a layered system as shown in figure 4-1. The Na sites in NaYbO_2 are fully occupied and are stoichiometric to within 1% resolution. No super-lattice reflections are observed in zero-field at 330 mK (figure 4-2a). Superlattice reflections appear at 5 T corresponding to an ordering wave vector of $q = (1/3, 1/3, 0)$ (figure 4-2b). Fits to this data yields a spin-canted “up-up-down” structure, to be discussed below, with moment $\mu_{\text{eff}} = 1.36(10)\mu_{\text{B}}$ (figure 4-2c).

Inelastic Neutron Scattering (INS) was also performed to characterize low-level magnetic excitations. Figure 4-2d shows diffuse INS spectra in zero-field (67 mK)

and 5 T (74 mK). In zero-field excitations are centered about $q = (1/3, 1/3, 0)$, while in the 5 T ordered state we see the spectra weight shifted into a flat band at 1 meV. This flat band of spin excitations is confirmed by the linear spin-wave calculations performed by our collaborators, shown in figure 4-2f.

Our collaborators took specific heat measurements from 40 K to 80 mK (figure 4-4,c-d). The high-temperature data shows broad features consistent with the paramagnetic signal from our magnetic susceptibility measurements. The zero-field low-temperature data shows a broad ‘two-peak’ structure that’s associated with QSL candidates due to charge or quasi-particle fractionalization [12]. In applied field, the specific heat develops a sharp peak at 1 K and 5 T, which is consistent with the magnetic transition observed by neutron scattering. Interestingly, this peak vanishes at 9 T, and the broad double-structure returns, which suggests re-entrant disorder. A re-entrant disordered state implies competing mechanisms of magnetic frustration.

4.2.2 Experimental NaYbO₂

Samples of NaYbO₂ consisted of pressed powder prepared by the Wilson Group of UC Santa Barbara. The sample was roughly rectangular and measured approximately 5.6 mm × 2.4 mm × 1.6 mm, and weighed 98.0 mg. We performed AC susceptibility measurements using a hand-wound AC susceptometer placed inside a Janis Cryogenics 3He system. Measurements were primarily performed with an excitation frequency of 711.4 Hz and a drive field of roughly 0.1 Oe. The susceptometer was calibrated against data taken in our Quantum Design MPMS3 system, which also provided magnetic susceptibility data in the 2 K to 300 K range. Frequency dependent zero-field AC magnetic susceptibility (χ_{AC}) measurements were performed by collaborators in a PPMS dilution fridge insert between the range 4 K and 50 mK. They measured χ_{AC} at an excitation of 1 Oe and a frequency range between 1 kHz and 10 kHz. Figure 4-3b Inset shows virtually no frequency dependence in χ_{AC} , which confirms that NaYbO₂ is not a spin-glassy system.

NaYbO₂ is air-sensitive and our experimental methods required temporary exposure to atmosphere. To ensure sample quality, magnetic susceptibility measurements

were first performed on samples at Wilson Lab using their Quantum Devices MPMS3, and then remeasured again at Graf Lab using our MPMS3 system. Samples were measured both before and after the experiment in order to confirm that the sample did not degrade during the experiment. Additionally, neutron diffraction measurements performed by Wilson Lab showed that reference samples were stoichiometric within 1% of resolution.

4.2.3 Results NaYbO₂

High temperature magnetic AC susceptibility (figure 4-3a) shows paramagnetic, Curie-Wiess-like (CW) behavior from 300 K to 2 K. We fit the data between 2 K and 100 K to

$$\frac{1}{\chi - \chi_0} = \left(\frac{C}{T - \Theta_{CW}} \right)^{-1}. \quad (4.2.1)$$

Note that Θ_{CW} is, in principle, temperature dependent for highly correlated systems such as spin-liquids and spin-ices due to extended spin-spin interactions (such as non-local topology [13]). With that caveat, we observe Curie-Wiess like behavior down to 330 mK, (figure 4-3b). Fits between 20 K and 100 K yields $\Theta_{CW} = -10.3(8)$ K, while between 1 K and 4 K yields $\Theta_{CW} = -0.45(4)$ K. We estimate the magnetic moment to be $\mu_{\text{eff}} = 2.63(8) \mu_B$. The inset shows frequency dependent ZF data taken by our collaborators [9]. The lack of a clear frequency dependence over three orders of magnitude confirms that the system is not a spin-glass [14]. The lack of a glassy state or any obvious magnetic transitions, combined with the apparent onset of long-range spin correlations seen from $\Theta_{CW}(T)$ imply that NaYbO₂ exists in correlated, yet disordered and non-spin frozen state at 300 mK — such as a potential QSL state.

The application of a DC magnetic field between $0.1 \text{ T} < H < 2 \text{ T}$ quickly suppresses χ' (figure 4-3b). A broad peak indicating spin-freezing appears at 0.2 T. Notably, these peak's curvature inflection points (as opposed to the peaks themselves) are roughly linear with field H and match the expected Zeeman splitting,

$\Delta E = 2g_{\text{ave}}J_{\text{eff}}\mu_B H$, where $g_{\text{ave}} = 3.03$, $J_{\text{eff}} = 1/2$, and $\Delta E \rightarrow k_B T$. The flattening of χ' at $H = 2$ T is due to the response of spin-frozen moments balancing out the response of free moments—such as impurities. We can estimate the ‘free-spin’ fraction as 7% to 14% [9], which suggests that in zero-field a sizeable fraction of independent ‘paramagnetic’ spins coexist within the quantum-disordered state (figure 4-3b Inset).

χ' in figure 4-4 shows that larger magnetic fields $3 \text{ T} < H < 7 \text{ T}$. χ' suddenly increases at 3 T, before sharply decreasing again at 4 T and 5 T. This corresponds well with the long-range order observed with neutrons. Above 5 T, χ' gradually increases till $H \sim 6$ T, and is nearly field independent at 7 T. Field-dependent data at 330 mK shows the trend more clearly with a peak at almost exactly 3 T, followed by a second feature near 6 T or 7 T.

The enhancement of χ' at 3 T is due to the system crossing the phase boundary of a quantum critical point near 3 T, uncovered thanks to these measurements. From neutron scattering we know that the system enters a long-ranged ordered state. Our collaborator’s neutron measurements show an “up-up-down” spin order (figure 4-2) with propagation vector $q = (1/3, 1/3, 0)$, $q = (0, 0, 0)$. Higher-field scattering data is unavailable, but at 6 T and 7 T we believe that the system approaches a second phase-boundary for a quantum paramagnet phase, based on our magnetic susceptibility measurements and our collaborator’s specific heat measurements (figure 4-4).

4.2.4 Discussion NaYbO₂

Magnetic susceptibility measurements of NaYbO₂ show a heavily frustrated system ($f > 200$) and a lack of zero-field spin ordering or freezing down to 50 mK. We observe a quantum critical point through field-induced long-range order. The disordered state of NaYbO₂ appears to be re-entrant with field, based on the plateau in $\chi'(H)$ near 6 T. Re-entrant disorder would imply that there are two competing sources of magnetic frustration in NaYbO₂. The spins in the ordered phase are canted and the planes appear to be ferromagnetically ordered along the c-axis. The combination of spin canting and interplane ordering indicates that interlayer interactions between are strong and frustrated, which reinforces the idea that spins in NaYbO₂ see competing

sources of magnetic frustration, with one of the sources being interplanar frustration. As such, 2D models cannot fully explain the magnetism in NaYbO₂ and 3D models incorporating interplane interactions are needed.

4.2.5 Theory NaYbO₂

The triangular Yb³⁺ systems have been well-studied theoretically. The large spin-orbit coupling in Yb³⁺ (SOC) results in anisotropic, bond-dependent, exchange interactions along the triangular lattice. Each bond-site follows a *R3m* space-group symmetry, therefore by symmetry considerations we can write down the most generic possible Hamiltonian [15] compatible with the lattice symmetry:

$$\mathcal{H}_{XXZ} = J \sum_{\langle ij \rangle} (S_i^x S_j^x + S_i^y S_j^y + \Delta S_i^z S_j^z) \quad (4.2.2a)$$

$$\mathcal{H}_{bd} = \sum_{\langle ij \rangle} 2J_{\pm\pm} (\cos \tilde{\varphi}[x, y]_{ij} - \sin \tilde{\varphi}\{x, y\}_{ij}) + J_{z\pm} (\cos \tilde{\varphi}\{x, y\}_{ij} - \sin \tilde{\varphi}[x, y]_{ij}) \quad (4.2.2b)$$

Eq. 4.2.2a is a straightforward Heisenberg *XXZ* model with an anisotropy parameter¹ $0 \leq \Delta \leq 1$, where the anisotropy results from spin-orbit coupling in Yb. The second, more complicated term, is the “bond-dependent”² containing more complicated anisotropies arising from spin-orbit coupling (SOC). Our notation here represents the bond angles as $\tilde{\varphi} = \{0, -2\pi/3, 2\pi/3\}$, while $[x, y]_{ij} = S_i^x S_j^x - S_i^y S_j^y$ and $\{x, y\}_{ij} = S_i^x S_j^y + S_i^y S_j^x$. We note that \mathcal{H}_{bd} physically represents an anisotropic compass model arising from SOC [15].

This Hamiltonian has a rich zero-field phase-diagram, as shown in figure 4-5 [15]. For various values of Δ , $J_{z\pm}/J$ and $J_{\pm\pm}/J$, the system hosts various types of long-range order, including ferromagnetic order, stripe-order, 120° antiferromagnetic order, and a potential spin-liquid phase.

The long-range magnetic order observed in 5 T fields can be explained through a

¹ $\Delta = 0$ corresponds to zero anisotropy and reduces \mathcal{H}_{XXZ} to a Heisenberg *XY* model.

²The bond dependent term allows for the interactions to differ along different bond directions, similar to the Kitaev Honeycomb model.

simpler Heisenberg XXZ model, which occurs as a special case of the above model. Specifically, taking $J_{\pm\pm}, J_{z\pm} = 0$ is equivalent to shutting off nearest neighbor interplanar interactions. Following ref. [16], we take:

$$\mathcal{H}_{XXZ} = \sum_{\langle ij \rangle} J(S_i^x S_j^x + S_i^y S_j^y) + J_z S_i^z S_j^z \quad (4.2.3)$$

where $J_z = \Delta \cdot J$. This model has been studied on the triangular lattice for applied fields with $B \parallel \hat{c}$, and for moderate magnetic fields displays a canted "up-up-down" structure, similar to what we observed in neutron scattering (figure 4-6) [16]. Notably, the triangular XXZ model is not frustrated in its ground state and is predicted to undergo long-range magnetic order in the entirety of its phase diagram. Correspondingly, we deduce that the interplanar interactions allowed by the $R3m$ symmetry — the \mathcal{H}_{bd} term from equation 4.2.2b—play a key role in frustrating the spins and preventing long-range magnetic order at low fields.

One particularly interesting aspect predicted by ref. [16]’s numerical calculations is that the spin-liquid state evolves out of a 120° AFM ground state for large values of Δ . This state occurs, as shown in the phase diagram, for small values of $J_{\pm\pm}/J$ and moderate $J_{z\pm}/J$, which is consistent with the observation of field-induced canted up-up-down order, as predicted by the simpler XXZ theory. What makes this interesting is that the 120° state causes most of the interplanar and anisotropic terms to drop out of the relevant energy states for the Hamiltonian, which causes the energy of the 2D Hamiltonian to become invariant under $U(1)$ symmetry (See Supplemental material of ref. [9]). This results in the interplanar interactions becoming frustrated, and this is unique to the 120° state compared to the other types of order predicted. Thus, it appears that NaYbO_2 maintains disorder through a frustration between competing phases of in-plane long-range order and out-of-plane long range order.

4.2.6 Conclusions NaYbO_2

NaYbO_2 is the first inorganic $J_{\text{eff}} = 1/2$ triangular systems that may reasonably host a QSL state. Prior inorganic compounds, such as $\text{Ba}_3\text{CoSb}_2\text{O}_9$ [17], [18] or NaTiO_3 [19],

[20] either magnetically order or deform at low temperatures. NaYbO_2 , on the other hand, shows paramagnetic behavior down to 50 mK and has a frustration factor of over 200. At the time of publication, the best triangular system were the organic compounds which are complicated molecular magnets that contain dozens of atoms per-unit cell [21], [22]. Additionally, we find that interplanar interactions play a role in stabilizing disorder by frustrating spins in a way that competes with frustration due to the triangular geometry. Thus NaYbO_2 gives us an unusual platform to study magnetic frustration in triangular systems through the tuning of a competing interplanar interaction that takes the system from 2D frustration to 3D frustration. We speculate that by tuning the strength of interplane frustration that we may be able to study the transition from the 2D limit to the 3D limit of potential QSL candidate.

4.3 LiYbO_2

4.3.1 Characterization LiYbO_2

In addition to our magnetic susceptibility and μSR measurements, our collaborators extensively characterized the chemical, electric, and magnetic structure of LiYbO_2 . For brevity, we do not discuss all of these results and instead direct the interested reader to the original paper [11]. Here we describe the characterizations that are key to interpreting our magnetic susceptibility and μSR results.

X-ray diffraction measurements show that the Yb ions form a stretched diamond structure, as shown in figure 4-7. The structure is bipartite, meaning that it can be decomposed into two structurally equivalent sublattices. The exchange interactions between nearest neighbors between sublattices and within sublattices differ, and we label them as J_1 and J_2 , respectively.

Heat capacity (figure 4-8) shows two sharp anomalies at 0.45 K and 1.13 K, which are preceded by a broad peak near 2 K. The broad peak is indicative of magnetic short-range correlations, while the two other peaks are magnetic ordering transitions (see below). The lower transition, T_1 , is noticeably suppressed by 3 T fields and is

absent at 5 T and 9 T. The upper transition T_2 is enhanced by applied fields with the entropy release increasing with field.

Neutron diffraction on polycrystals (figure 4-9) identifies the transitions observed in heat-capacity as a bipartite incommensurate spiral order.

Below 450 mK the system orders with two degenerate ordering vectors $k = (0.384, \pm 0.384, 0)$. Fits to the spectra yield a bipartite helical structure where the two sublattices of the diamond structure both order independently with the above k vector, but a 0.58π phase offset between equivalent sites. An illustration is shown in figure 4-9. The minimum correlation length is estimated at 364 Å

Between 450 mK and 1.1 K the system enters an intermediate state characterized by the same ordering vector $k = (0.384, \pm 0.384, 0)$, but with reductions to the reflection peak at $|Q| = 1.2 \text{ \AA}^{-1}$. The minimum correlation length is estimated at 364 Å. This data can be fitted by either assuming a random phase difference between the Yb^{3+} sublattices. Whether this is the result of the phase being random between individual sample grains, or random within individual crystals due to quasi-long range order is unclear. It is possible that other models may more accurately capture the data.

Below 450 mK with $H = 3 \text{ T}$, the system commensurately orders with $k = (1/3, \pm 1/3, 0)$, but with an otherwise similar helical structure. The phase difference between sublattice is 0.42π in this phase.

Low-energy Inelastic Neutron Scattering between 36 mK and 1.1 K shows low-energy fluctuations with a bandwidth of roughly 1 meV (figure 4-10). The spectra changes little with applied fields, even after the ordering transition at 3 T. At 36 mK and 10 K the system transitions into a field-polarized state and magnetic fluctuations are suppressed.

4.3.2 Experimental LiYbO₂

Samples of LiYbO₂ consisted of pressed powder prepared by the Wilson Group of UC Santa Barbara. The sample was a non-rectangular fragment and measured approximately 3.7 mm × 4.9 mm × 1.9 mm, and weighed 50.25(5) mg. We performed AC susceptibility measurements using a hand-wound susceptometer placed inside a Janis Cryogenics 3He system. The experimental setup for these measurements was the same as for NaYbO₂, which is described in detail above.

Additionally, we also performed μ SR measurements on LiYbO₂ (paper under review). For μ SR, the sample consisted of a polycrystalline powder pressed into a disc 1 cm in diameter and 2 mm thick. μ SR measurements were taken at the Paul Scherrer Institute (PSI) using the Dolly and General Purpose Spectrometer (GPS) detectors. The sample was first measured in GPS down to 1.5 K using a gas-flow cryostat; the sample was mounted on a ‘fork’ sample-holder using Kapton tape to minimize the background. The sample was then measured in Dolly using an Oxford Heliox 3He Insert to measure to 280 mK. The sample in Dolly was mounted to a Silver sample holder to maximize thermalization. In both detectors, the experiments were performed in longitudinal polarization mode in order to maximize the zero-field (ZF) and longitudinal field (LF) signals. Data was analyzed using the MuSRFit software suite [23].

4.3.3 Results LiYbO₂

Magnetic Susceptibility

Figure 4-11 shows high-temperature Curie-Weiss fits to the DC magnetic susceptibility between $20 < T < 100$ K.

$$\frac{1}{\chi - \chi_0} = \left(\frac{C}{T - \Theta_{CW}} \right)^{-1}. \quad (4.3.1)$$

We obtain $C = 0.94 \text{ emu K mol}^{-1}$, $\Theta_{CW} = -3.4 \text{ K}$, and $\chi_0 = 0.0070 \text{ emu}^{-1} \text{ mol}^{-1}$. From this we extract an effective moment of $\mu_{\text{eff}} = 2.74 \mu_B$. The deviation of the

Curie-Weiss fit near 100 K is due to Van Vleck susceptibility from the CEF splitting the $\text{Yb} = 7/2$ manifold, as opposed to a temperature dependent $\Theta_{\text{CW}}(T)$ as in NaYbO_2 . Low temperature susceptibility shows a peak near 1.3 K and what appears to be an upturn at 0.45 K. These signatures are consistent with the heat capacity measurements taken by our collaborators which show sharp features at 0.45 K and 1.1 K.

Muon Spin Rotation

Based on our neutron scattering results, we expect to see spontaneous muon oscillations in zero applied field due to the long-range magnetic order, and we expect a dynamical response due to the persistent 1 meV spin fluctuations seen in Inelastic Neutron scattering (INS). The low-temperature spectra (figure 4-12) show no signs of oscillations, though weak dynamical processes are present. Both spectrometers show a temperature independent initial asymmetry of $a_0 \approx 0.21$. No missing asymmetry is observed, which rules out the possibility of fast depolarization outside PSI's time resolution. This is confirmed by high resolution data (figure 4-12 Inset). The weak dynamics is confirmed by the slow decay of the 1/3 tail to zero for the spectra at all temperatures.

We fit the spectra to the following phenomenological function:

$$A(t) = a_0(1 - f_\lambda)e^{-\frac{\sigma^2 t^2}{2}} + f_\lambda e^{-\lambda t} \quad (4.3.2)$$

The gaussian term captures the fast depolarization from frozen Yb^{3+} moments while $e^{-\lambda t}$ represents the quasi-static limit of dynamical decay due to the weak spin fluctuations observed in INS.

Figure 4-13 shows the temperature dependence of the spectra below 2 K. The gaussian rate σ shows a broad transition starting at 1.1 K, while we see a sharp transition in λ and f_λ with weak temperature dependence above or below T_N . The rise in λ immediately above T_N corresponds with the onset of short-range correlations seen in neutron scattering. The observed temperature agrees well with neutron scattering and our magnetic susceptibility measurements. The sharp drop of f_λ to 1/3

is consistent with a thermodynamic transition from a paramagnetic state to a LRO ordered state in a polycrystal, as opposed to a gradual spin-freezing process. The tail decays as a weak exponential depolarization with $\lambda \cong 0.25 \mu\text{s}^{-1}$, which is suggestive of magnetic fluctuations in the ordered state. The rate is in the quasi-static limit. The Gaussian depolarization with rate $\sigma \cong 45 \mu\text{s}^{-1}$ indicates a highly magnetic ground state that is characterized by frozen spins or long-range magnetic order. The lack of spontaneous oscillations in the asymmetry spectra tells us that the system is either long-range disordered, or that the precessional frequency of the muon is too fast to be detected.

Figure 4-13 shows the longitudinal field response in the ordered phase. We expect the internal field to be, at minimum, on the order of $\gamma_\mu \sigma \approx 500 \text{ Oe}$ for a spin frozen system, and up to several orders of magnitude more for a LRO system. Therefore we expect little decoupling from an applied field of $B_{LF} = 50 \text{ Oe}$ and for full decoupling near $B_{LF} \sim 5000 \text{ Oe}$ if the system is not LRO. In the slow fluctuation limit we expect the exponential depolarization rate λ to be field independent. We instead observe the opposite, with a very large response to 50 Oe, significant decoupling through 800 Oe, and a very strong suppression of λ .

The high temperature LF spectra (figure 4-14) on the other hand agree with conventional expectations. The high-temperature spectra are fit to

$$P(t) = \text{GKT}(\sigma_N t, B_{LF}) e^{-\lambda T} \quad (4.3.3)$$

where $\text{GKT}(\sigma_N t, B_{LF})$ represents the Gaussian Kubo-Toyabe function which arises from nuclear moments (see chapter 3); $\sigma_N = 0.163(1) \mu\text{s}^{-1}$. We attribute the exponential factor to fluctuating electronic moments in the motional narrowing limit, which is typical for paramagnetic moments at high temperatures. The value of λ is roughly constant between 56 K and 10 K: On Dolly $\lambda(T = 56 \text{ K}) = 0.147(7) \mu\text{s}^{-1}$ and $\lambda(10 \text{ K}) = 0.151(3) \mu\text{s}^{-1}$ while for GPS $\lambda(45 \text{ K}) = 0.170(5) \mu\text{s}^{-1}$ and $\lambda(15 \text{ K}) = 0.173(5) \mu\text{s}^{-1}$.

The high-temperature LF spectra show that the nuclear depolarization is easily

suppressed by $B_{\text{LF}} = 50 \text{ Oe}$, as expected for the weakly magnetic nuclei. The exponential component is qualitatively unchanged by fields of up to 500 Oe , as expected, which demonstrates that the exponential decay arises from dense electronic (Yb^{3+}) moments in the fast-fluctuation limit (see chapter 3). Additionally, the simple ZF functional form and response to longitudinal fields implies that the system is homogeneous in its paramagnetic state. This rules out magnetic inhomogeneity due to inclusions and similar defects.

The lack of a temperature dependence in the high-temperature ZF spectra between 10 K and 56 K is unusual, but can occur due to several reasons unrelated to magnetic frustration. Specifically, λ is temperature independent in the $T \rightarrow \infty$ limit of a Curie-Weiss magnet [24], and this is occasionally observed [25]. Alternatively, crystal electric field splitting may sometimes create quasi-degenerate states that create a nearly constant spin-fluctuation rate ν over a broad temperature range [26].

4.3.4 Discussion LiYbO_2

The specific heat, neutron, and magnetic susceptibility data taken for LiYbO_2 points to an incommensurate long range ordered state. The phase disordered state between 450 mK and 1.1 K is an interesting consequence of magnetic frustration though, and not fully understood. In particular LiYbO_2 proximate to a QSL state, or even host a closely related ‘quantum spiral spin liquid’ state [27]–[29].

In the original neutron paper, our collaborators performed some basic theoretical analysis to show that most of the phase diagram of LiYbO_2 can be captured by the $J_1 - J_2$ model (Figure 4-15 [11]. With proper tuning of the parameters, the various helical orders below 450 mK , including the phase differences between the bipartite lattices of Yb^{3+} . The $J_1 - J_2$ Heisenberg model failed to capture the presence of a distinct magnetic phase between 450 mK and 1.1 K . It also failed to capture the effect of interplane interactions, which cant the spins and align their the planes ferromagnetically along the c -axis.

The random phase state between 450 mK and 1.1 K is merely an assumption; neutron scattering was unable verify for certain that this is the correct state. Therefore,

we refer to this theory as the "random phase bipartite model" (RPBI). As a local field probe, μ SR provides additional supporting evidence that the RPBI state exists, as well as additional evidence that the ground state is highly degenerate, or at least proximate to a QSL-like state.

The μ SR data is unusual; different spectra appear to support different conclusions about the magnetic state of the system.. We see no spontaneous muon oscillations in zero-field from the long-range order. The complicated magnetic structure of LiYbO_2 may heavily dampen oscillations, but the short time data clearly shows a lack of conventional oscillations. The exponential decay at long times—as opposed to a restoration to a $1/3$ tail—suggests that slow, to moderate dynamics is present in the system. The LF spectra appear to contradict this though: the sensitivity of the spectra to small LF fields indicates that the internal field distribution probed by the muon is small, and that the system is static.

One possible interpretation of the LF spectra is that the system is magnetically inhomogeneous. If the muon probes regions of extremely weak magnetism, on the order of nuclear dipole fields, then a full decoupling would be expected by 50 Oe. While it is plausible that the ground state of the system is inhomogeneous, such an idea runs into conceptual difficulties when compared to the other spectra. The zero-field spectra at low T would be expected to follow a Kubo-Toyabe curve (see chapter 3) with a rate of $\sigma \sim 0.1 \mu\text{s}^{-1}$ to $0.2 \mu\text{s}^{-1}$, which is not seen. It would also be difficult to interpret f_λ , whose value of $1/3$ corresponds well to a quasi-static polycrystal system. At high temperature, the ZF and LF spectra are consistent with a homogeneous paramagnet, as one would expect.

As a last point, the shape of the depolarization envelope is unusual, resembling that of a Bessel function of an incommensurate magnet more than the Gaussian decay expected of a frozen spin lattice. We find that no single conventional depolarization function fits the rapid decay over multiple spectra below the 1.1 K. Fitting the full data range well requires a minimum of three independent terms whose parameters do not yield a temperature dependence. Given the unusual incommensurate order seen by neutron scattering, it is likely that one would need to derive their own polarization

function to fit the data properly. It is for that reason I perform my own analysis of the system and derive the following " J_0^2 model" to describe system.

4.3.5 Model of μ SR in LiYbO_2

The approximate internal field distribution for a single stopping site in an incommensurate magnet is known and given as [24]:

$$D_m(B_{\text{loc}}) = \begin{cases} \frac{1}{\pi} \frac{1}{\sqrt{B_{\text{max}}^2 - B_{\text{loc}}^2}}, & -B_{\text{max}} < B_{\text{loc}} < B_{\text{max}} \\ 0, & \text{Otherwise} \end{cases} \quad (4.3.4)$$

The muon only sees internal fields $|\mathbf{B}_{\text{loc}}| < B_{\text{max}}$. This field distribution is fundamentally different from most other distributions in μ SR in that it arises due to long-range magnetic order instead of random disorder. As a result, the internal field distribution is bounded by $\pm B_{\text{max}}$.

The polarization for an isotropic polycrystal is [24]

$$P(t) = \frac{1}{3} + \frac{2}{3} \int_0^\infty \cos(\gamma_\mu B_{\text{loc}} t) D_m(B_{\text{loc}}) dB_{\text{loc}}. \quad (4.3.5)$$

For the field distribution in equation 4.3.5, this gives $P(t) = 2/3 J_0(\gamma_\mu B_{\text{max}} t) + 1/3$, where $J_0(x)$ is the 0th order Bessel function of the 1st kind. The oscillations in an incommensurate magnet inherently depolarize themselves, with a rate proportion to the oscillation frequency (See figure 4-16). Moreover, the decay envelope for times $t \gg \gamma_\mu B_{\text{max}}$ goes as $1/t$ which is a unique polynomial decay instead of the exponential decay that is ubiquitous to nearly all other analytical polarization functions. Additionally, incommensurate magnets are noticeably more sensitive to small longitudinal fields than either commensurate magnets or conventionally disordered systems. These unique attributes can be traced back to the fact that for an incommensurate system, the muon stopping site samples the entire magnetic unit-cell, as opposed to sampling random variances in the local magnetic field at the muon stopping site due to defects or disorder.

Our system is a bipartite system consisting of two magnetic sublattices with identical spiral order, but a phase difference ω between the two sublattices. Neutron scattering shows compelling evidence that ω is disordered and randomized between either magnetic domains or polycrystal grains in the temperature range $450 \text{ mK} < T < 1.1 \text{ K}$. We propose that the internal field distribution can be modeled as two identical, but independent, incommensurate field distributions.

The combination of two statistically independent field distribution is the convolution product of the two field distributions: $D(\mathbf{B}_{\text{loc}}) = (D_1 * D_2)(\mathbf{B}_{\text{loc}})$ (see chapter 3). Equation 4.3.5 has the form of a cosine Fourier transform and the Fourier transform of a convolution is simply the product of the individual Fourier transforms.

This immediately gives the polarization function for our “doubly-incommensurate” model:

$$P(t) = \frac{2}{3} J_0^2(\gamma_\mu B_{\text{max}} t) + \frac{1}{3} \quad (4.3.6)$$

We can generalize equation 4.3.6 to the slow fluctuation limit by writing $P(t) = 2/3 J_0^2(\gamma_\mu B_{\text{max}} t) + 1/3 e^{-2/3t}$. We can further generalize this to account for certain types of magnetic anisotropies, or small inhomogeneities by writing

$$P(t) = (1 - f_\lambda) J_0^2(\gamma_\mu B_{\text{max}} t) + f_\lambda e^{-\lambda t} \quad (4.3.7)$$

This now resembles our original phenomenological fit function in equation 4.3.2, but with the gaussian term replaced by J_0^2 . We can establish a firm connection between equations 4.3.2 and 4.3.7 by noting that the gaussian term was fitted only to the short times of the spectra, while the Lorentzian term was fitted to long time behavior.

To second order:

$$\begin{aligned}
e^{-\frac{\sigma^2 t^2}{2}} &\approx 1 - \sigma^2 t^2 / 2 \\
J_0^2(\gamma_\mu B_{\max} t) &\approx 1 - \frac{\gamma_\mu^2 B_{\max}^2 t^2}{2} \\
\therefore e^{-\frac{\sigma^2 t^2}{2}} &\approx J_0^2(\gamma_\mu B_{\max} t) \quad \text{and} \quad \sigma \approx \gamma_\mu B_{\max} \quad \text{for sufficiently small } t. \quad (4.3.8)
\end{aligned}$$

Thus, we have shown that our theoretically derived result in equation 4.3.7 is equivalent to our phenomenological fit function in 4.3.2 in the short time limit. This is confirmed comparing our phenomenological fit to equation 4.3.7 while using the same parameters (figure 4-17) for $T = 550$ mK. Equation 4.3.7 aligns almost perfectly with the data without any additional fitting required. More importantly, the oscillations are highly suppressed and fit well within the noise-width of our data, which explains the lack of clear oscillations despite the long range order.

We can also qualitatively explain the anomalous LF dependence using this model as well. While not trivial, it can be shown that the internal field distribution resulting from the self-convolution of eq. 4.3.4

$$D_m(B_{\text{loc}}) = \frac{4}{\pi^2} K \left[1 - \left(\frac{B_{\text{loc}}}{2B_{\max}} \right)^2 \right] \begin{cases} \text{For } -2B_{\max} < \mathbf{B}_{\text{loc}} < 2B_{\max} \\ 0 \quad \text{Otherwise} \end{cases} \quad (4.3.9)$$

$K[x]$ is the Complete Elliptical Integral of the First Kind, and a function that does not normally appear in μ SR theory.³ We plot the calculated field distribution in figure 4-17 against the standard incommensurate field distribution.

From the field distribution we expect the Elliptical distribution to be highly sensitive to small longitudinal fields, and less sensitive to larger fields, due to the large spectral weight near $\mathbf{B}_{\text{loc}} = 0$ Oe. This is as opposed to the standard incommensu-

³Note that the domain of $K(X)$ here is $\pm 2B_{\max}$, not $\pm 1B_{\max}$. This is because B_{loc} is a physical variable, therefore the domains of equation 4.3.4 and 4.3.5 are formally $(-\infty, \infty)$. Physically, this represents the fact that the local field the muon sees is the sum of the fields from the two sublattices. Therefore if the max field seen by the muon from one sublattice is $\pm B_{\max}$, then the maximum field seen by the muon is $\pm 2B_{\max}$.

rate field distribution which features most of its spectral weight near $\mathbf{B}_{\text{loc}} = B_{\text{max}}$. We numerically calculate the LF dependence of the static tail in figure 4-17 for our proposed distribution, as well as several other common field distributions [25], [30], [31].

Figure 4-17a shows that both the conventional models and the J_0^2 model grossly overestimate the static tail at high-fields. Only the J_0^2 model has, qualitatively, the correct field-dependence. Given that magnetic inhomogeneity has been ruled out, this suggests that there is some subtle physics at work. The culprit is likely "sporadic dynamics," which has been observed in several other frustrated systems, including ones similar to LiYbO_2 over the years [25], [30], [31].

4.3.6 Persistent and Sporadic Dynamics in μSR and LiYbO_2

Highly frustrated spin systems frequently exhibit anomalous "persistent dynamics" well into their ordered phase, even down to 50 mK [32]–[34]. In these systems dynamics appears with an unusually slow rate ranging between 0.1 – 10 MHz, which normally would qualify as "quasi-static." Less frequently, some of these systems show a perplexingly weak longitudinal field responses that suggest that the internal fluctuation rate is dozens of times larger than measured via ZF measurements [35]. In these cases, the applied LF field itself appears to be linearly screened by a constant factor f [25], [30], [31]. The current theory is that these anomalous systems experience "intermittent" fields where the internal field depolarizes the muon only for some fraction of the time f . It can be shown that longitudinal μSR functions obey (in simple cases) the scaling law $P(ft, \Delta, \omega, B_{\text{LF}}, \nu) = P(t, f\Delta, f\omega, fB_{\text{LF}}, f\nu)$ where Δ , B_{LF} , ω and ν are the characteristic internal field strengths, the applied LF field, the oscillation frequency, and the fluctuation rates, respectively [25]. As a result, the LF response of the system is reduced, as well as the apparent dynamical rates in zero-field.

Figure 4-17b shows the results of the RPBI model for a screening factor of $\alpha = 1/3$. We obtain numerical agreement with the data. Conversely, the other conventional models are unable to obtain even qualitative agreement with the data due to the differences in curvature at low field values. At first glance, this is surprising: systems

characterized by sporadic dynamics are less sensitive to applied fields—not more. And indeed that is true in this case. But remember, the RPBI model is inherently sensitive to small longitudinal fields due to the peak near $B_{\text{loc}} = 0$ (4-16a), which is extremely unusual for a long-range ordered state. For a given initial depolarization rate at $t = 0$, the J_0^2 is naturally far more sensitive to small longitudinal fields than other conventional systems.

The deficiency of this model is that we cannot provide a concrete explanation as to why sporadic dynamics occur. Sporadic dynamics have only been reported for a small number of systems, and there is currently no proper microscopic theory, beyond the qualitative explanation given above. That said, we do note that the double-degenerate wave-vector $(0.384, \pm 0.384, 0)$ allows the spiral structures to have an arbitrary direction of propagation in the ab -plane. The ground state of LiYbO_2 may be highly degenerate with collective spin fluctuations between different propagation directions. Such fluctuations may be the source of low-energy spin excitations seen in INS and provide a potential mechanism for sporadic dynamics. Moreover, such fluctuations would be suggestive of a “spiral quantum spin liquid.” Loosely speaking, a spiral QSL is a QSL-like state consisting of fluctuating, degenerate, spin spirals, as opposed to degenerate individual spins. Such a state has been recently proposed for NiRh_2O_4 [29].

With this, our model is complete and successfully describes the μSR spectra, including the anomalous LF dependences. The bipartite, phase-disordered, incommensurate order creates a highly unusual field distribution that is abnormally sensitive to small applied fields. Furthermore, the anomalous exponential decay in zero-field is indeed a result of the weak dynamics observed by INS. Moreover, LiYbO_2 is a rare system that—in addition to conventional dynamics—also exhibits sporadic dynamics. The mechanism of sporadic dynamics is not well understood, and may be evidence of a highly degenerate, QSL-like, ground state in the system.

4.4 Conclusions

The AYbO_2 ($A=\text{Akali}$) family is a diverse group of frustrated $J_{\text{eff}} = 1/2$ magnets. In particular, NaYbO_2 is an excellent example of a viable QSL candidate. It is one of the first simple, inorganic, compound to host a frustrated $J_{\text{eff}} = 1/2$ triangular lattice. NaYbO_2 shows no conventional signs of spin-freezing or magnetic order down to 50 mK. Our magnetic susceptibility measurements show that NaYbO_2 is quantum critical—we see magnetic field induced long-range order. At 3 T the system long-range orders with an unusual AFM up-up-down down order. Magnetic susceptibility and specific heat measurements suggest that at 6 T and 7 T the long-range order melts into a reentrant disordered state. Correspondingly, our discovery of extreme frustration and a quantum critical point in NaYbO_2 has kicked off a large flurry of research.

LiYbO_2 is a more complicated case. The system undergoes long range order at 1.1 K, so it's not QSL system—though it may be proximate to a QSL state. Below 450 mK LiYbO_2 forms a bipartite incommensurate spiral structure, where the two sublattices are phase offset by 0.58π . The magnetic order can be mostly understood through the $J_1 - J_2$ Heisenberg model, though spin canting and a ferromagnetic alignment of the planes show that interplane correlations are important to the spin physics and that the system is not 2D. The $J_1 - J_2$ Heisenberg model fails to describe the intermediate temperature range $1.1 \text{ K} > T > 0.45 \text{ K}$ where the sublattices appear to have randomized phases. Additionally, inelastic neutron scattering shows the presence of low energy persistent dynamics down to 50 mK, even in the presence of high fields $B < 10 \text{ K}$.

Our μSR measurements are seemingly difficult to understand. μSR spectra show no spontaneous oscillations or missing asymmetry which would indicate long-range magnetic order. The spectra give uneven evidence for the presence of weak dynamics. The μSR data can be understood by a combination of ‘persistent’ dynamics which have been seen in other frustrated systems similar to LiYbO_2 , and by introducing a novel ‘doubly-incommensurate’ local field distribution based on the unique magnetic

structure we previously proposed for LiYbO_2 . This gives rise to a J_0^2 depolarizations that almost completely suppresses spontaneous oscillations and depolarizes the muon at a rapid rate relative to the size of the internal magnetic field distribution. This internal field distribution is highly sensitive to longitudinal field measurements.

We have characterized two important compounds in the first of frustrated magnetism, NaYbO_2 and LiYbO_2 . The former has proved to be an ideal system to access the QSL physics of a triangular lattice. The former is a long-range ordered magnet that allows a test of the $J_1 - J_2$ Heisenberg model. Additionally, our μSR measurements on LiYbO_2 illustrates the limits of μSR on ordered magnets, allows us to extend the theory of μSR in incommensurate magnets, and suggests that LiYbO_2 may be a spiral quantum spin liquid material.

4.5 References

- [1] Y. Zhou, K. Kanoda, and T.-K. Ng, “Quantum spin liquid states,” *Reviews of Modern Physics*, vol. 89, no. 2, p. 025 003, Apr. 18, 2017. DOI: 10.1103/RevModPhys.89.025003.
- [2] S. Sachdev, “Kagome and triangular-lattice Heisenberg antiferromagnets: Ordering from quantum fluctuations and quantum-disordered ground states with unconfined bosonic spinons,” *Physical Review B*, vol. 45, no. 21, pp. 12 377–12 396, Jun. 1, 1992. DOI: 10.1103/PhysRevB.45.12377.
- [3] L. Savary and L. Balents, “Quantum spin liquids: A review,” *Reports on Progress in Physics*, vol. 80, no. 1, p. 016 502, Jan. 1, 2017. DOI: 10.1088/0034-4885/80/1/016502.
- [4] N. Niggemann, M. Hering, and J. Reuther, “Classical spiral spin liquids as a possible route to quantum spin liquids,” *Journal of Physics: Condensed Matter*, vol. 32, no. 2, p. 024 001, Jan. 9, 2020. DOI: 10.1088/1361-648X/ab4480.

- [5] M. R. Norman, “Colloquium: Herbertsmithite and the search for the quantum spin liquid,” *Reviews of Modern Physics*, vol. 88, no. 4, p. 041 002, Dec. 2, 2016. DOI: 10.1103/RevModPhys.88.041002.
- [6] J. Knolle and R. Moessner, “A Field Guide to Spin Liquids,” *Annual Review of Condensed Matter Physics*, vol. 10, no. 1, pp. 451–472, Mar. 10, 2019. DOI: 10.1146/annurev-conmatphys-031218-013401.
- [7] L. Clark and A. H. Abdeldaim, “Quantum Spin Liquids from a Materials Perspective,” *Annual Review of Materials Research*, vol. 51, no. 1, pp. 495–519, Jul. 26, 2021. DOI: 10.1146/annurev-matsci-080819-011453.
- [8] C. Broholm, R. J. Cava, S. A. Kivelson, D. G. Nocera, M. R. Norman, and T. Senthil, “Quantum spin liquids,” *Science*, vol. 367, no. 6475, p. 0668, Jan. 17, 2020. DOI: 10.1126/science.aay0668.
- [9] M. M. Bordelon, E. Kenney, C. Liu, *et al.*, “Field-tunable quantum disordered ground state in the triangular-lattice antiferromagnet NaYbO₂,” *Nature Physics*, vol. 15, no. 10, pp. 1058–1064, Oct. 2019. DOI: 10.1038/s41567-019-0594-5.
- [10] Y. Li, G. Chen, W. Tong, *et al.*, “Rare-Earth Triangular Lattice Spin Liquid: A Single-Crystal Study of ybm₂gao₄,” *Physical Review Letters*, vol. 115, no. 16, p. 167 203, Oct. 16, 2015. DOI: 10.1103/PhysRevLett.115.167203.
- [11] M. M. Bordelon, C. Liu, L. Posthuma, *et al.*, “Frustrated Heisenberg $J_1 - J_2$ model within the stretched diamond lattice of LiYbO₂,” *Physical Review B*, vol. 103, no. 1, p. 014 420, Jan. 14, 2021. DOI: 10.1103/PhysRevB.103.014420.
- [12] Y. Motome and J. Nasu, “Hunting Majorana Fermions in Kitaev Magnets,” *Journal of the Physical Society of Japan*, vol. 89, no. 1, p. 012 002, Jan. 15, 2020. DOI: 10.7566/JPSJ.89.012002.
- [13] A. Nag and S. Ray, “Misjudging frustrations in spin liquids from oversimplified use of Curie-Weiss law,” *Journal of Magnetism and Magnetic Materials*, vol. 424, pp. 93–98, Feb. 2017. DOI: 10.1016/j.jmmm.2016.10.014.

- [14] J. A. Mydosh, “Spin glasses: Redux: An updated experimental/materials survey,” *Reports on Progress in Physics*, vol. 78, no. 5, p. 052 501, May 1, 2015. DOI: 10.1088/0034-4885/78/5/052501.
- [15] Z. Zhu, P. A. Maksimov, S. R. White, and A. L. Chernyshev, “Topography of Spin Liquids on a Triangular Lattice,” *Physical Review Letters*, vol. 120, no. 20, p. 207 203, May 15, 2018. DOI: 10.1103/PhysRevLett.120.207203.
- [16] D. Yamamoto, G. Marmorini, and I. Danshita, “Quantum Phase Diagram of the Triangular-Lattice XXZ Model in a Magnetic Field,” *Physical Review Letters*, vol. 112, no. 12, p. 127 203, Mar. 26, 2014. DOI: 10.1103/PhysRevLett.112.127203.
- [17] Y. Shirata, H. Tanaka, A. Matsuo, and K. Kindo, “Experimental Realization of a Spin-1/2 Triangular-Lattice Heisenberg Antiferromagnet,” *Physical Review Letters*, vol. 108, no. 5, p. 057 205, Jan. 31, 2012. DOI: 10.1103/PhysRevLett.108.057205.
- [18] J. Ma, Y. Kamiya, T. Hong, *et al.*, “Static and Dynamical Properties of the Spin-1/2 Equilateral Triangular-Lattice Antiferromagnet $\text{Ba}_3\text{CoSb}_2\text{O}_9$,” *Physical Review Letters*, vol. 116, no. 8, p. 087 201, Feb. 24, 2016. DOI: 10.1103/PhysRevLett.116.087201.
- [19] S. J. Clarke, A. J. Fowkes, A. Harrison, R. M. Ibberson, and M. J. Rosseinsky, “Synthesis, Structure, and Magnetic Properties of NaTiO_2 ,” *Chemistry of Materials*, vol. 10, no. 1, pp. 372–384, Jan. 19, 1998. DOI: 10.1021/cm970538c.
- [20] G. Jackeli and D. A. Ivanov, “Dimer phases in quantum antiferromagnets with orbital degeneracy,” *Physical Review B*, vol. 76, no. 13, p. 132 407, Oct. 22, 2007. DOI: 10.1103/PhysRevB.76.132407.
- [21] S.-S. Lee and P. A. Lee, “ $U(1)$ Gauge Theory of the Hubbard Model: Spin Liquid States and Possible Application to $\kappa\text{-(BEDT-TTF)}_2\text{Cu}_2(\text{CN})_3$,” *Physical Review Letters*, vol. 95, no. 3, p. 036 403, Jul. 15, 2005. DOI: 10.1103/PhysRevLett.95.036403.

- [22] T. Itou, A. Oyamada, S. Maegawa, M. Tamura, and R. Kato, “Quantum spin liquid in the spin-1/2 triangular antiferromagnet $\text{EtMe}_3\text{Sb}[\text{Pd}(\text{dmit})_2]_2$,” *Physical Review B*, vol. 77, no. 10, p. 104413, Mar. 11, 2008. DOI: 10.1103/PhysRevB.77.104413.
- [23] A. Suter and B. M. Wojek, “Musrfit: A Free Platform-Independent Framework for μSR Data Analysis,” *Physics Procedia*, 12th International Conference on Muon Spin Rotation, Relaxation and Resonance ($\mu\text{SR}2011$), vol. 30, pp. 69–73, Jan. 1, 2012. DOI: 10.1016/j.phpro.2012.04.042.
- [24] A. Le Yaouanc and P. D. De Réotier, *Muon Spin Rotation, Relaxation, and Resonance: Applications to Condensed Matter*, ser. International Series of Monographs on Physics no. 147. Oxford: Oxford University Press, 2010, 486 pp., ISBN: 978-0-19-959647-8.
- [25] Y. J. Uemura, A. Keren, K. Kojima, *et al.*, “Spin Fluctuations in Frustrated Kagomé Lattice System $\text{SrCr}_8\text{Ga}_4\text{O}_{19}$ Studied by Muon Spin Relaxation,” *Physical Review Letters*, vol. 73, no. 24, pp. 3306–3309, Dec. 12, 1994. DOI: 10.1103/PhysRevLett.73.3306.
- [26] D. Procissi, A. Lascialfari, E. Micotti, *et al.*, “Low-energy excitations in the $S = 1/2$ molecular nanomagnet $\text{K}_6[\text{V}_{15}^{\text{IV}}\text{As}_6\text{O}_{42}(\text{H}_2\text{O})] \cdot 8\text{H}_2\text{O}$ from proton NMR and μSR ,” *Physical Review B*, vol. 73, no. 18, p. 184417, May 15, 2006. DOI: 10.1103/PhysRevB.73.184417.
- [27] L. Balents, “Spin liquids in frustrated magnets,” *Nature*, vol. 464, no. 7286, Mar. 2010, ISSN: 1476-4687. DOI: 10.1038/nature08917.
- [28] X.-P. Yao, J. Q. Liu, C.-J. Huang, X. Wang, and G. Chen, “Generic spiral spin liquids,” *Frontiers of Physics*, vol. 16, no. 5, p. 53303, May 28, 2021, ISSN: 2095-0470. DOI: 10.1007/s11467-021-1074-9.
- [29] F. L. Buessen, M. Hering, J. Reuther, and S. Trebst, “Quantum Spin Liquids in Frustrated Spin-1 Diamond Antiferromagnets,” *Physical Review Letters*, vol. 120, no. 5, p. 057201, Jan. 29, 2018. DOI: 10.1103/PhysRevLett.120.057201.

- [30] P. Dalmas de Réotier, V. Glazkov, C. Marin, *et al.*, “Studies of $R_2Ti_2O_7$ (R=Gd and Yb); new results,” *Physica B: Condensed Matter*, vol. 374–375, pp. 145–147, Mar. 2006. DOI: 10.1016/j.physb.2005.11.037.
- [31] D. Bono, P. Mendels, G. Collin, *et al.*, “ μ Sr study of the Quantum Dynamics in the frustrated $S = 3/2$ Kagomé Bilayers,” *Physical Review Letters*, vol. 93, no. 18, p. 187 201, Oct. 26, 2004. DOI: 10.1103/PhysRevLett.93.187201.
- [32] Y. Cai, M. N. Wilson, A. M. Hallas, *et al.*, “ μ SR study of spin freezing and persistent spin dynamics in $NaCaNi_2F_7$,” *Journal of Physics: Condensed Matter*, vol. 30, no. 38, p. 385 802, Aug. 2018. DOI: 10.1088/1361-648X/aad91c.
- [33] M. T. Rovers, P. P. Kyriakou, H. A. Dabkowska, G. M. Luke, M. I. Larkin, and A. T. Savici, “Muon-spin-relaxation investigation of the spin dynamics of geometrically frustrated chromium spinels,” *Physical Review B*, vol. 66, no. 17, p. 174 434, Nov. 26, 2002. DOI: 10.1103/PhysRevB.66.174434.
- [34] P. Dalmas de Réotier, A. Maisuradze, and A. Yaouanc, “Recent μ SR Studies of Insulating Rare-Earth Pyrochlore Magnets,” *Journal of the Physical Society of Japan*, vol. 85, no. 9, p. 091 010, Sep. 15, 2016. DOI: 10.7566/JPSJ.85.091010.
- [35] P. Carretta and A. Keren, “NMR and μ SR in Highly Frustrated Magnets,” in *Introduction to Frustrated Magnetism: Materials, Experiments, Theory*, ser. Springer Series in Solid-State Sciences 164, Berlin, Heidelberg: Springer-Verlag Berlin Heidelberg Springer e-books, 2011, pp. 98–101, ISBN: 978-3-642-10589-0.

4.6 Figures

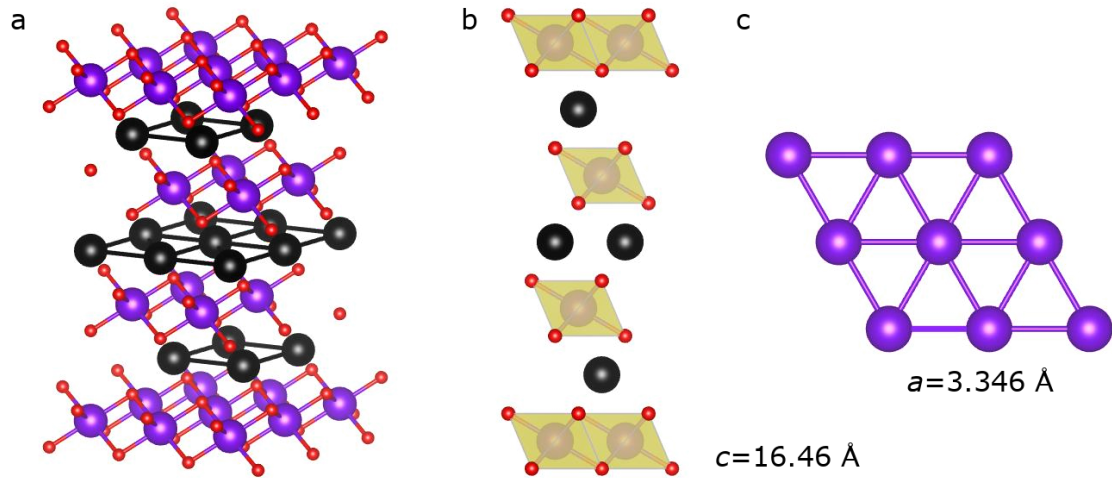


Figure 4-1: (a) Layered structure of NaYbO₂. Purple spheres = Ytterbium, black = Sodium, red = Oxygen. (b) Side view of NaYbO₂ structure with Yb octahedra emphasized. (c) top view (*ab*-plane) of Yb-layers. Yb spacing is 2.346 Å. Full details of the crystallographic structure can be found in [9].

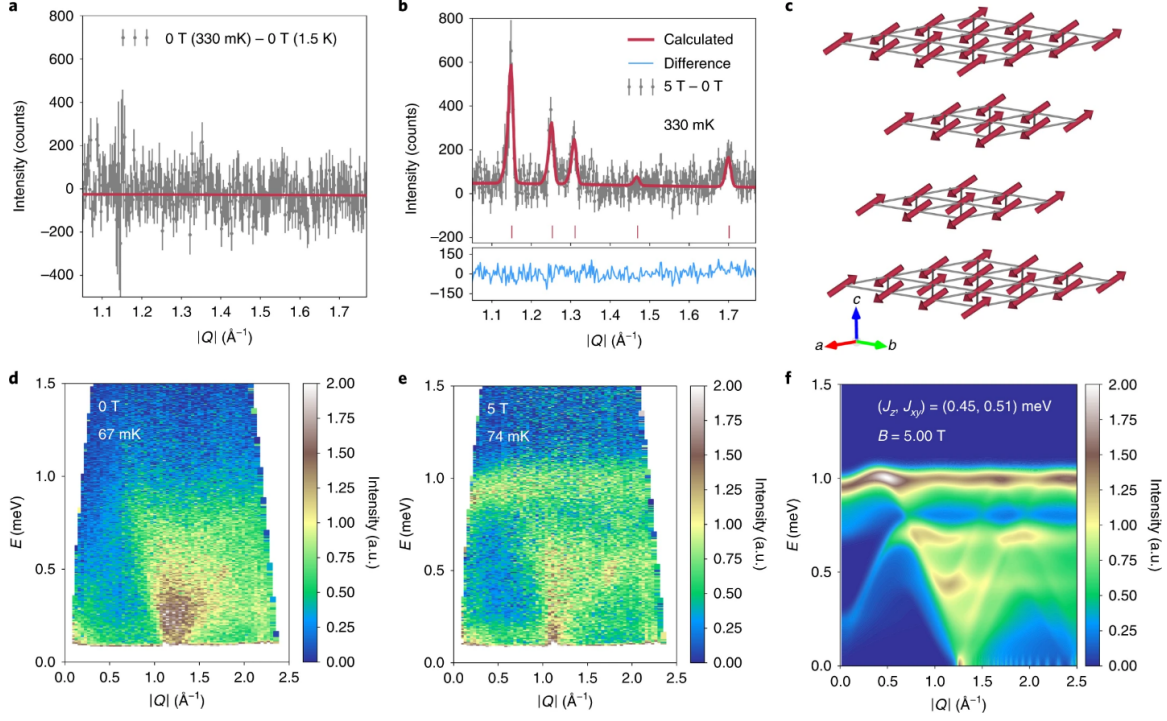


Figure 4-2: Neutron diffraction and inelastic scattering data, presented as originally published, for NaYbO₂. **(a)** Zero-field temperature-subtracted neutron powder diffraction spectra (0.330 K to 1.5 K). No magnetic reflection peaks are observed. **(b)** Magnetic field-subtracted neutron spectra (450 mK and 5 T - 330 mK and 0 T). Peaks appear at $(1/3, 1/3, z)$ positions ($z = 0, 1, 3$), with a corresponding wave vector of $q = (1/3, 1/3, 0)$. **(c)** Magnetic structure of best fit to 5 T data. Moments align approximately along $\langle 1, -1, -1 \rangle$ in an 'up-up-down' order, with a Yb moment of $1.36(10) \mu_B$. **(d, e)** Inelastic neutron-scattering spectra in zero-field (67 mK) and 5 T (74 mK). **(f)** Linear spin wave calculations showing powder averaged $S(Q, E)$ for a two-dimensional triangular lattice of anisotropic Yb³⁺ moments of NaYbO₂ in a 5 T field, with the proposed 'up-up-down' order. Error bars indicate one standard deviation of the data.

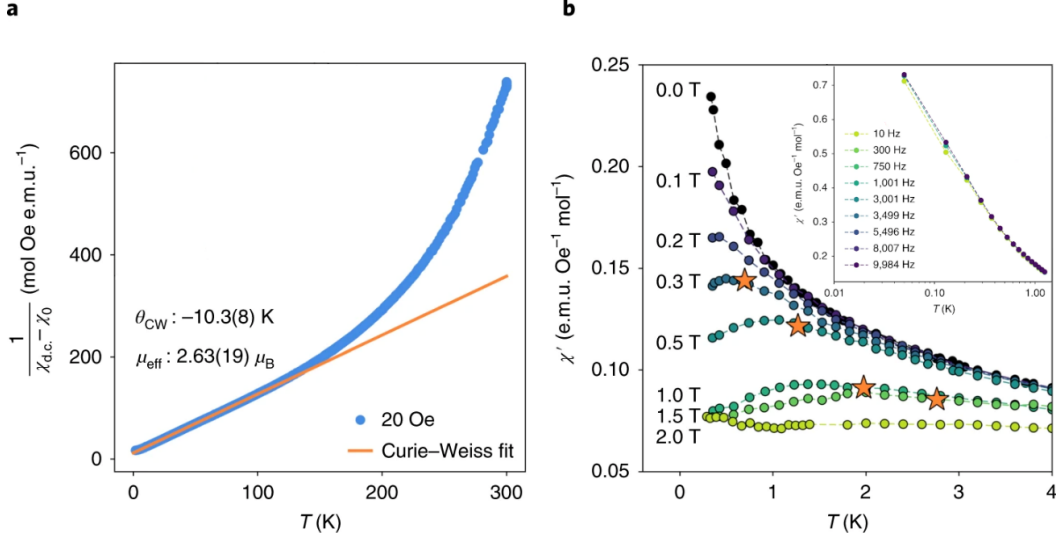


Figure 4-3: Bulk magnetic susceptibility and specific heat data for NaYbO₂. (a) DC magnetic susceptibility from 2 K to 300 K with Curie-Weiss fit between 20 K and 100 K. $\theta_{CW} = -10.3(8)$ K and $\mu_{eff} = 2.63(8) \mu_B$. (b) Real AC susceptibility as a function of temperature between 330 mK and 4 K. Stars represent the expected Zeeman splitting energy using $T = \Delta E/k_B = 2g_{ave} J_{eff} \mu_B H/k_B$. (Inset) Real AC susceptibility as a function of temperature and excitation frequency. The lack of appreciable shifts over three orders of magnitude indicates that the system is not a spin-glass.

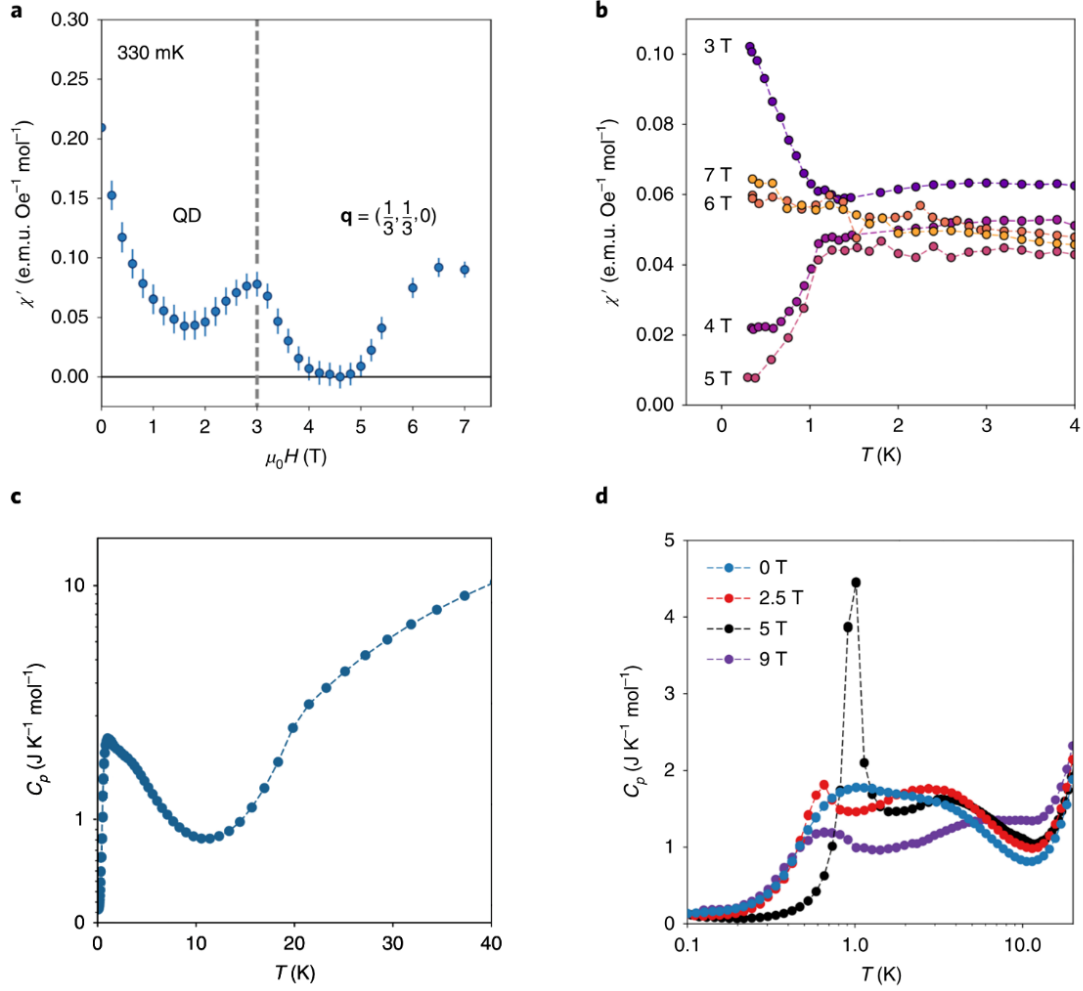


Figure 4-4: Bulk magnetic susceptibility and specific heat data from ref. [9] for NaYbO₂. (a) Real AC magnetic susceptibility as a function of field at 330 mK. At 3 T the system orders with propagation vector $\mathbf{q} = (1/3, 1/3, 0)$. (b) Real AC magnetic susceptibility between 1 T and 7 T. We observe a transition temperature at 1 K for all fields, which is consistent with specific heat measurements. (c) Zero-field Heat-capacity C_p from 40 K to 80 mK showing crossover behavior. (d) Low-temperature Heat-capacity C_p on a log scale.

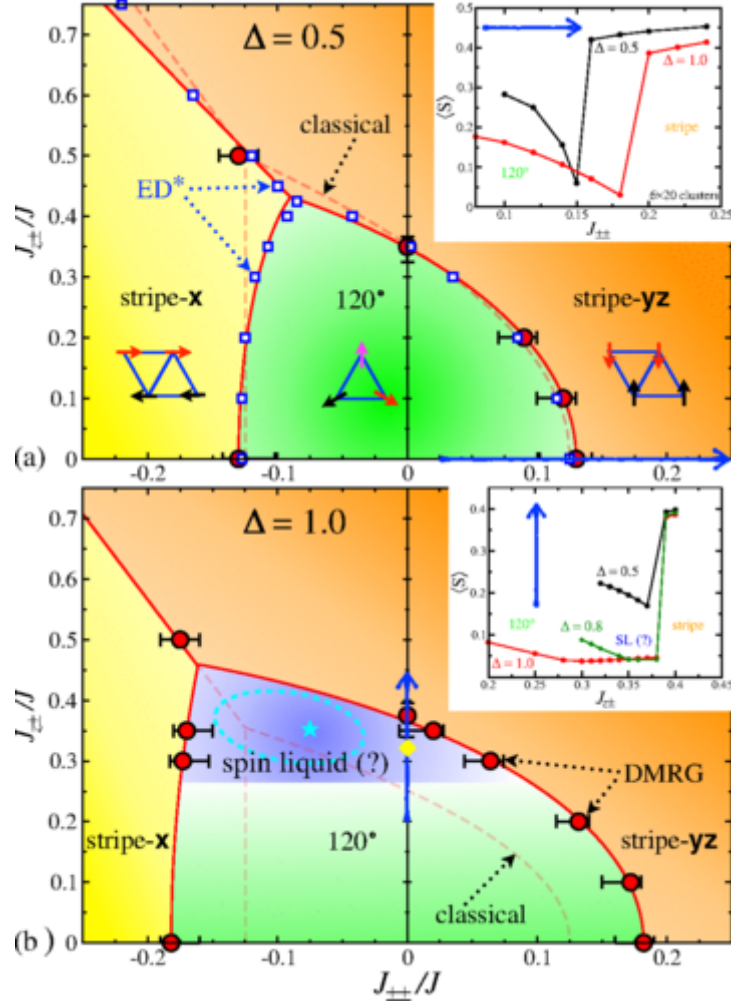


Figure 4-5: Theoretical phase diagram of the generalized nearest-neighbor spin-1/2 triangular lattice, for selected anisotropies $\Delta = 0.5$ and $\Delta = 1.0$. definitions of $J_{z\pm}/J$ and $J_{\pm\pm}/J$ are given in the text. Full details of figures and models can be found in the original source, ref. [15]. Phase diagram predicts 120° order and a potential spin liquid state for small values of $J_{\pm\pm}/J$, and high anisotropy parameters Δ . This state evolves continuously out of the 120° order state, and therefore is expected to exhibit spin-fluctuations with 120° correlations.

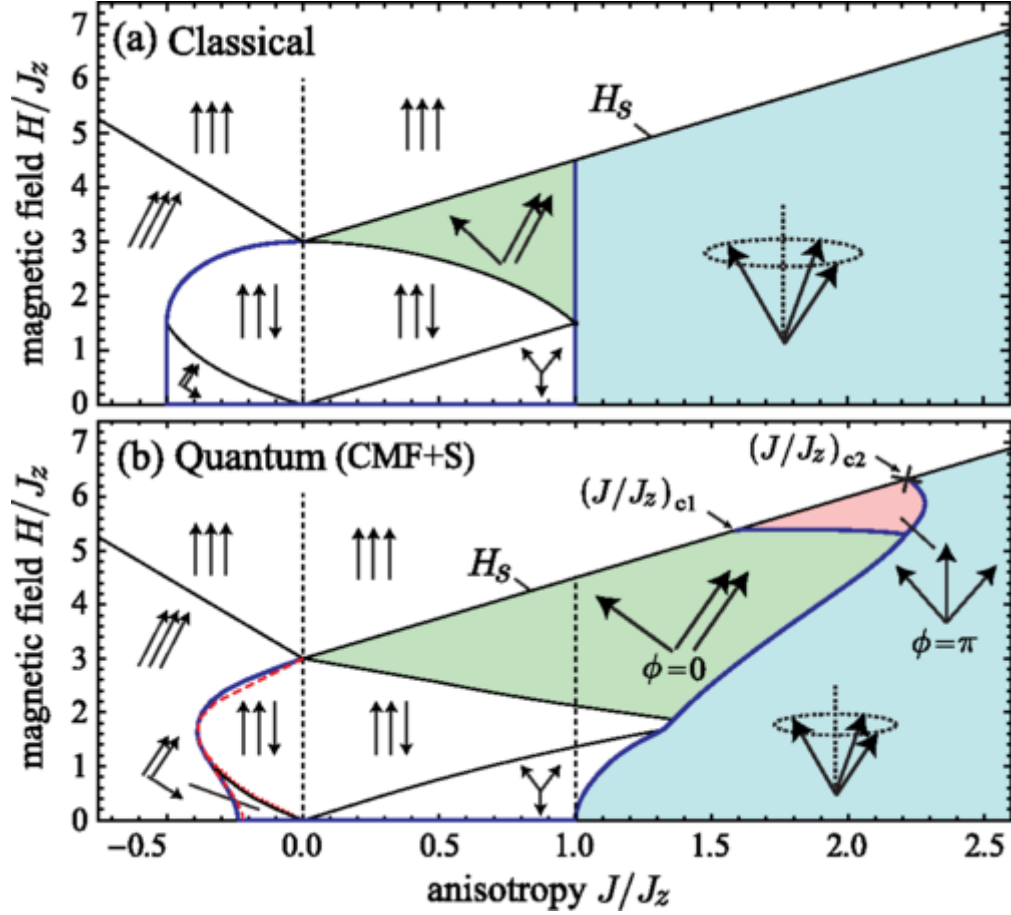


Figure 4-6: Theoretical phase diagram of the anisotropic XXZ model on the triangular lattice, with magnetic field H applied along the \hat{c} -axis (out-of-plane [16]). The top diagram (a) shows the classical phase diagram, while the bottom diagram (b) accounts for quantum mechanical effects on the diagram. Arrows illustrate the relative ordering of spin-1/2 moments in a triangular cell. Here the quantity J/J_z corresponds to $1/\Delta$ in the general model. Both phase diagrams are fully ordered in their ground state, indicating that this model is not sufficient to describe the disordered behavior of NaYbO_2 . Both diagrams do predict, though, a field-induced ‘up-up-down’ order for small to moderate anisotropies including spin-canted ‘up-up-down’. This diagram agrees well with the coupling constant of $J_z \sim 0.45$ estimated from neutron diffraction, which places $|J/J_z| \sim 0.5$

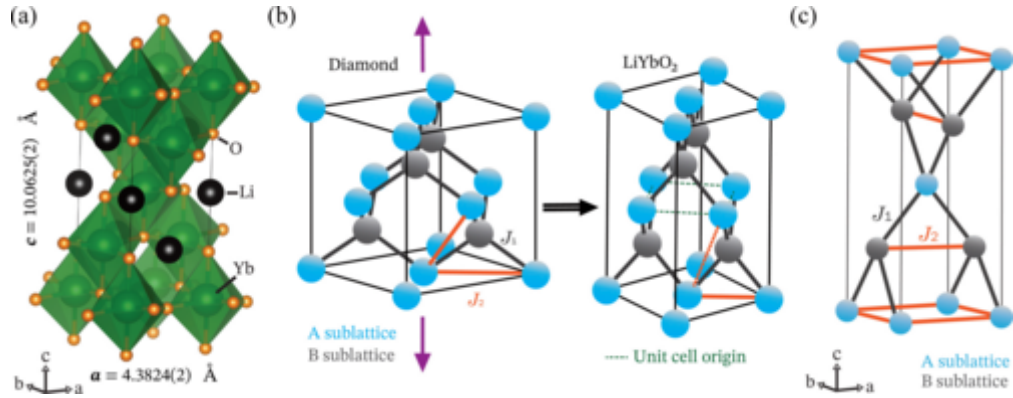


Figure 4-7: Structure of LiYbO_2 , as presented in our paper ref. [11]. (a) Crystal-structure with Black=Li, Orange=O, and green=Yb octahedra. (b) Diagram illustrating an idealized diamond structure and the stretched diamond structure of LiYbO_2 . (c) Diagram showing a simplified unit cell of the Yblattice, with emphasis on the bipartite sublattice structure. Black lines J_1 represent nearest-neighbor spin-couplings within a sublattice, while orange lines J_2 represent nearest-neighbor spin couplings between the two sublattices.

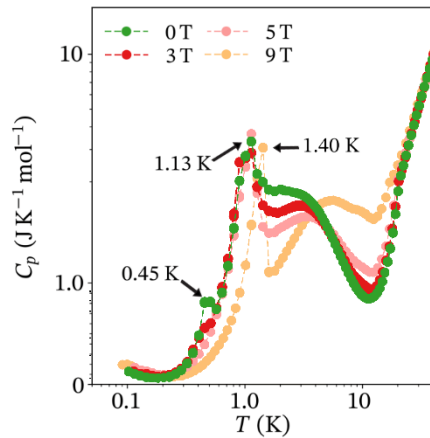


Figure 4-8: Specific Heat $C(T)$ of LiYbO_2 as a function of temperature for $B = 0, 3, 4,$ and 9 T. Original figure can be found in ref. [11].

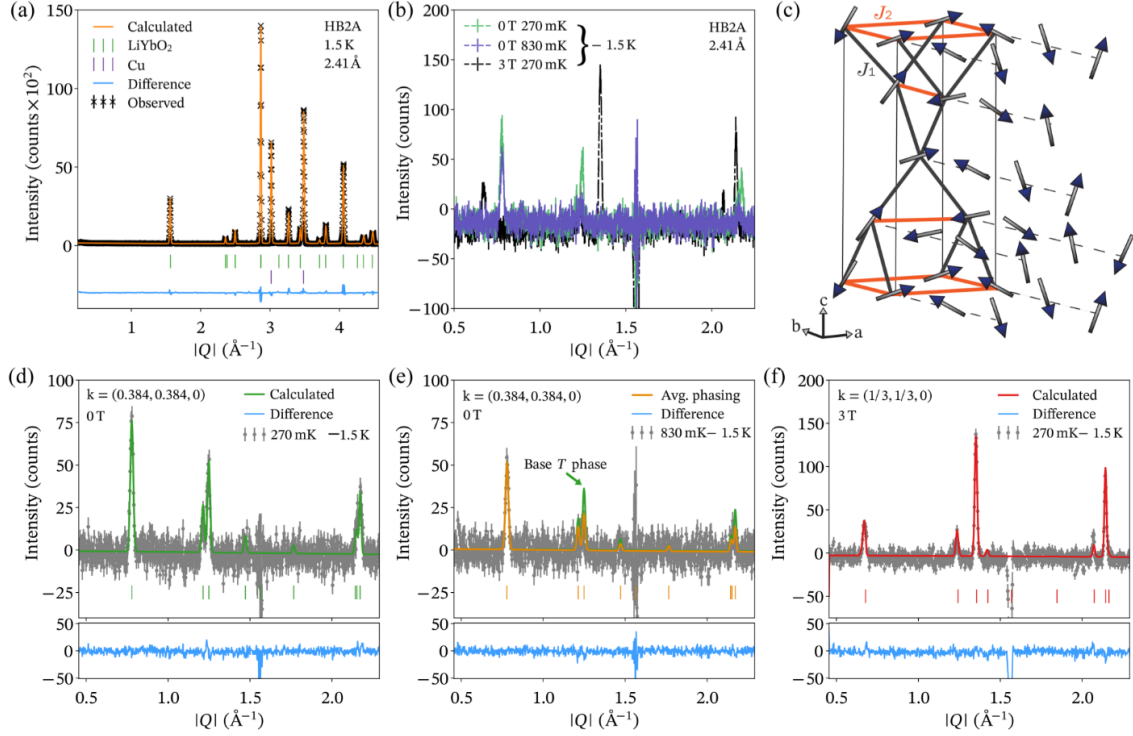


Figure 4-9: Neutron powder diffraction data for LiYbO_2 as originally published, including caption text [11]. Data was collected at HB-2A at the High Flux Isotope Reactor. (a) Fits to the elastic scattering data at 1.5 K reveal only one structural phase. (b) Temperature-subtracted diffraction data ($T - 1.5$ K) revealing a series of new magnetic peaks on cooling. Additionally, at 270 mK and 3 T, another set of magnetic peaks arise. Intensity near 1.5 \AA results from slight under/over subtraction of the structural peak at that position in (a) and is not a magnetic Bragg reflection. (c) helical magnetic structure fit below the ordering transition T_N2 . (d) The 270 mK data collected under zero field with the 1.5 K structural data subtracted. Green line shows the resulting fit using the magnetic structure described in the text. (e) The 830 mK data collected under zero field with the 1.5 K structural data subtracted. The orange line shows the partially disordered, intermediate helical state described in the text and the green line shows a fit using the fully ordered helical structure for comparison. (f) The 270 mK data collected under $\mu_B H = 3$ T with the 1.5 K structural data subtracted. The red line shows the fit to the commensurate magnetic structure describe in the text.

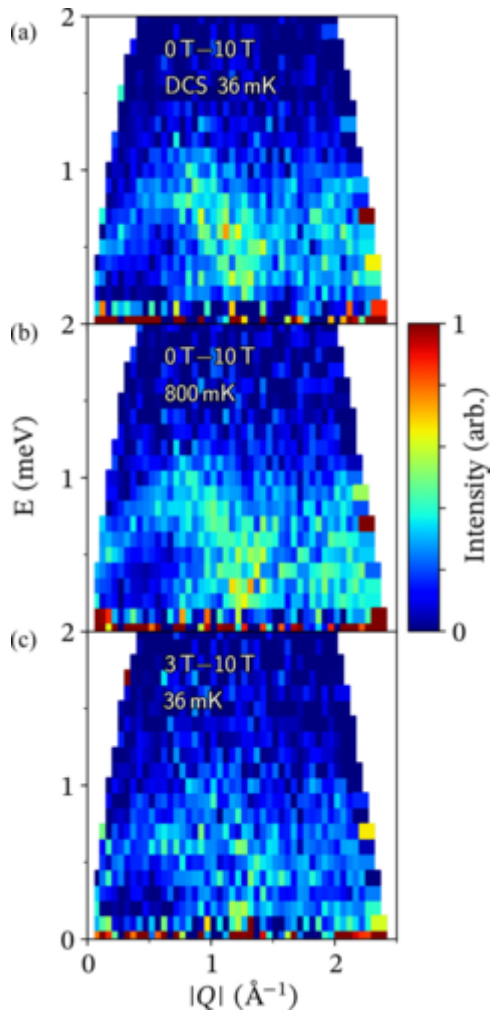


Figure 4-10: Low energy inelastic neutron scattering spectra $S(|Q|, \hbar\omega)$ for LiYbO_2 [11]. (a) $B=0$ T and $T = 36$ mK. (b) $B = 0$ T and $T = 800$ mK. (c) $B=3$ T and $T = 36$ mK. All spectra have data at $B = 10$ T and $T = 36$ mK subtracted off.

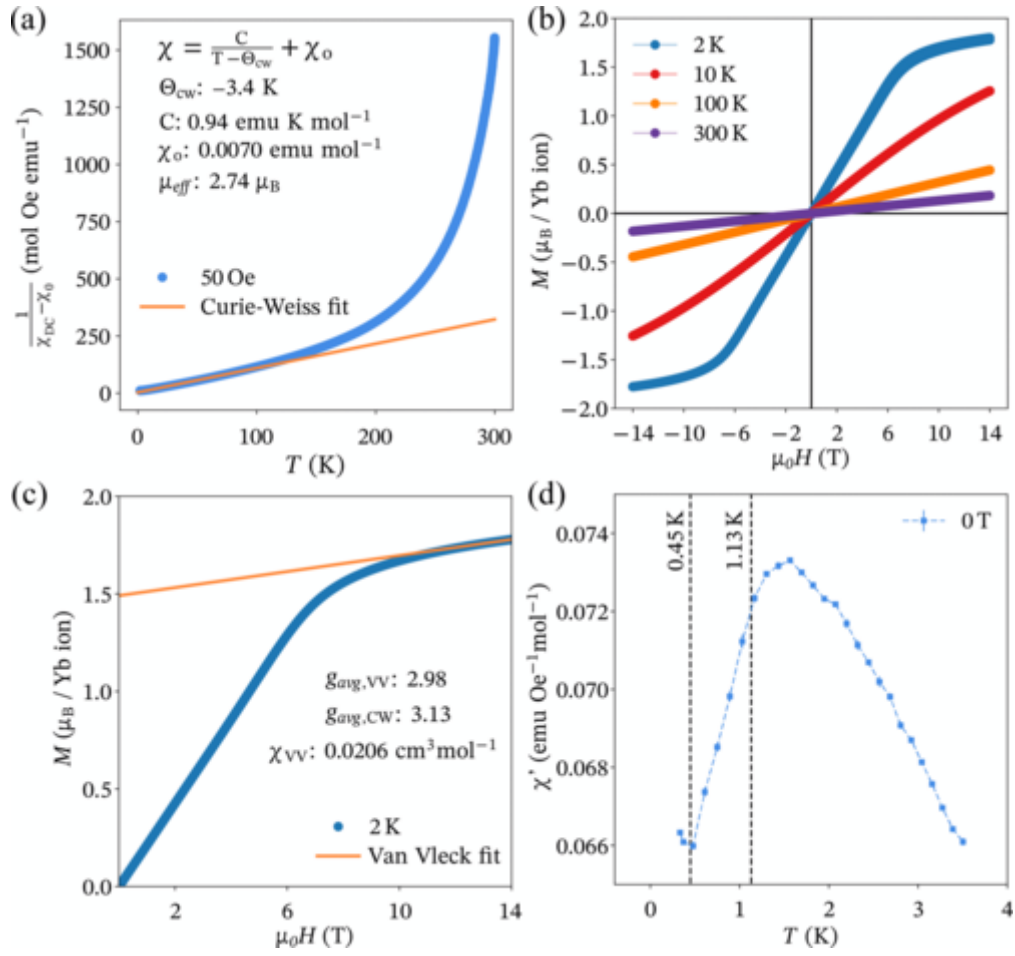


Figure 4-11: Bulk magnetic susceptibility and magnetization for LiYbO₂ [11]. (a) Fits to high temperature DC susceptibility between 20 K and 100 K. (b) Isothermal DC magnetization. (c) Van Vleck fit to DC magnetization at 2 K. (d) Real AC magnetic susceptibility in zero field at lower temperatures. Transition temperatures at 1.13 K and 450 mK are highlighted.

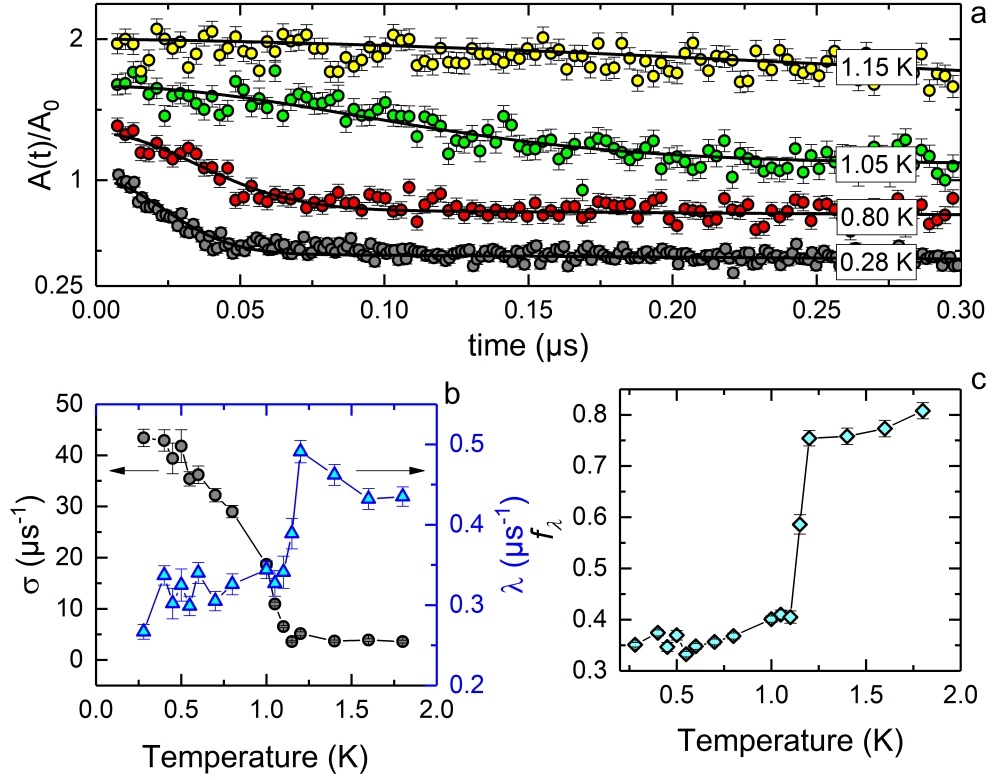


Figure 4-12: μSR data for LiYbO_2 . (a) Selected zero-field (ZF) asymmetry spectra from 0.28 K to 1.15 K measured on the Dolly spectrometer. Curves are offset by 1/3 for clarity. We observe a sharp transition between 1.05 K and 1.15 K. (b,c) Temperature dependence of the fit parameters described in the main text. The exponential rate λ and its fraction f_λ describes the long time decay of the asymmetry,, which is indicative of slow spin fluctuations, while the Gaussian rate σ describes the short-time behavior due to static order. The sharp drop of f_λ to 1/3 is consistent with a thermodynamic transition to a spin-ordered state in a polycrystalline sample.

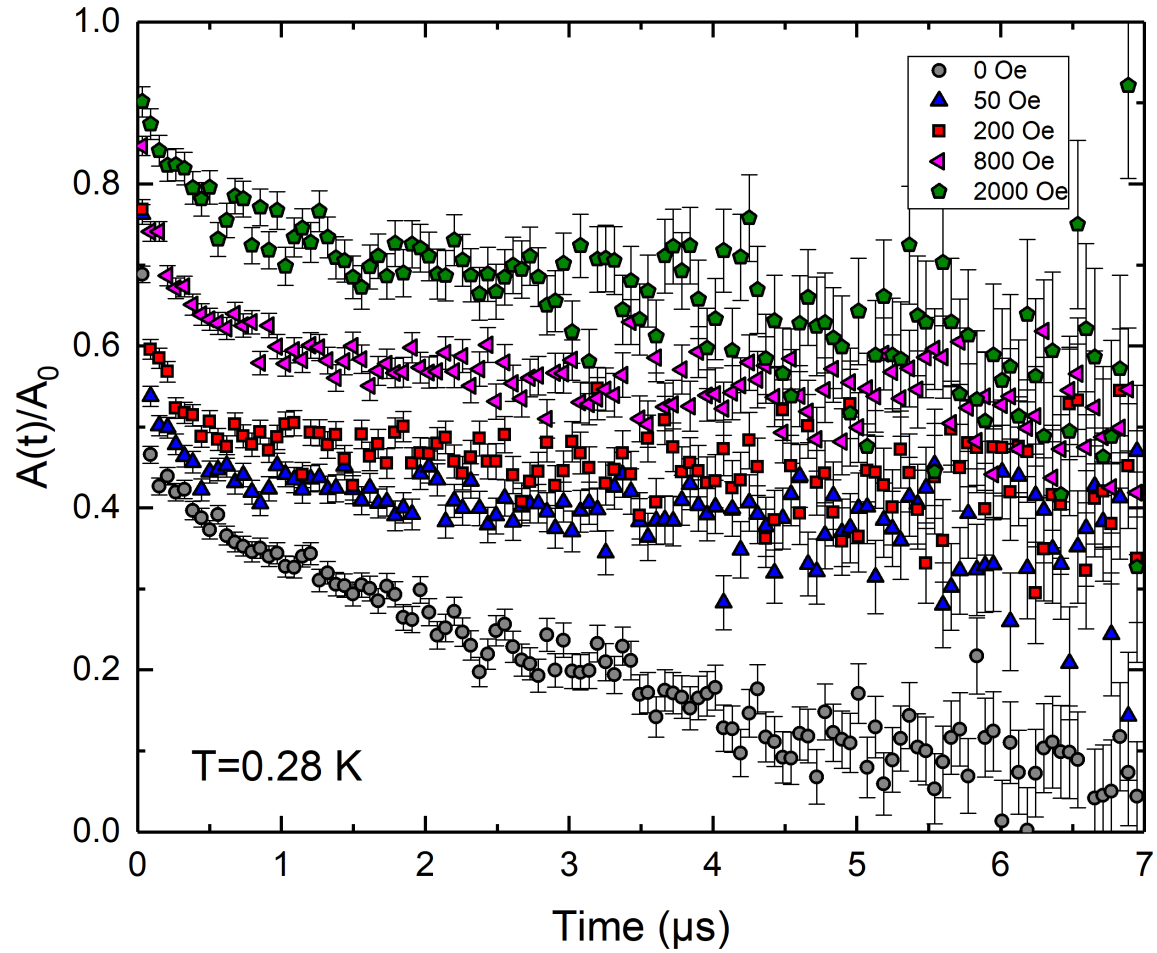


Figure 4-13: μ SR data for LiYbO_2 . Longitudinal Field μ SR Spectra at 0.28 K. The initial lifting of the asymmetry spectra corresponds to the suppression of static disorder or quasi-static fluctuations.

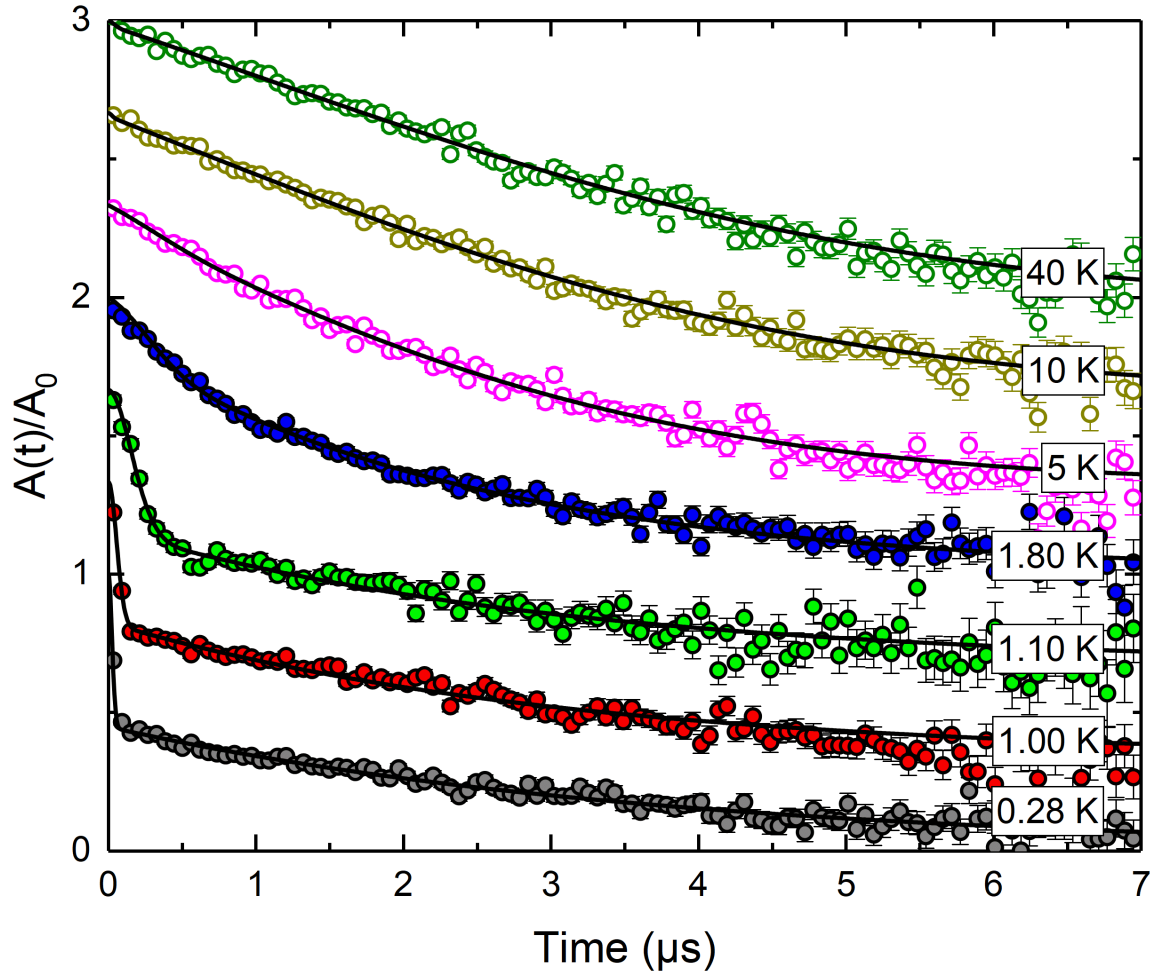


Figure 4-14: Zero field depolarization spectra of LiYbO₂ measured on the Dolly (solid circles) and GPS (empty circles) spectrometers with fits as described in text (solid lines). Curves are offset by 1/3 for clarity.

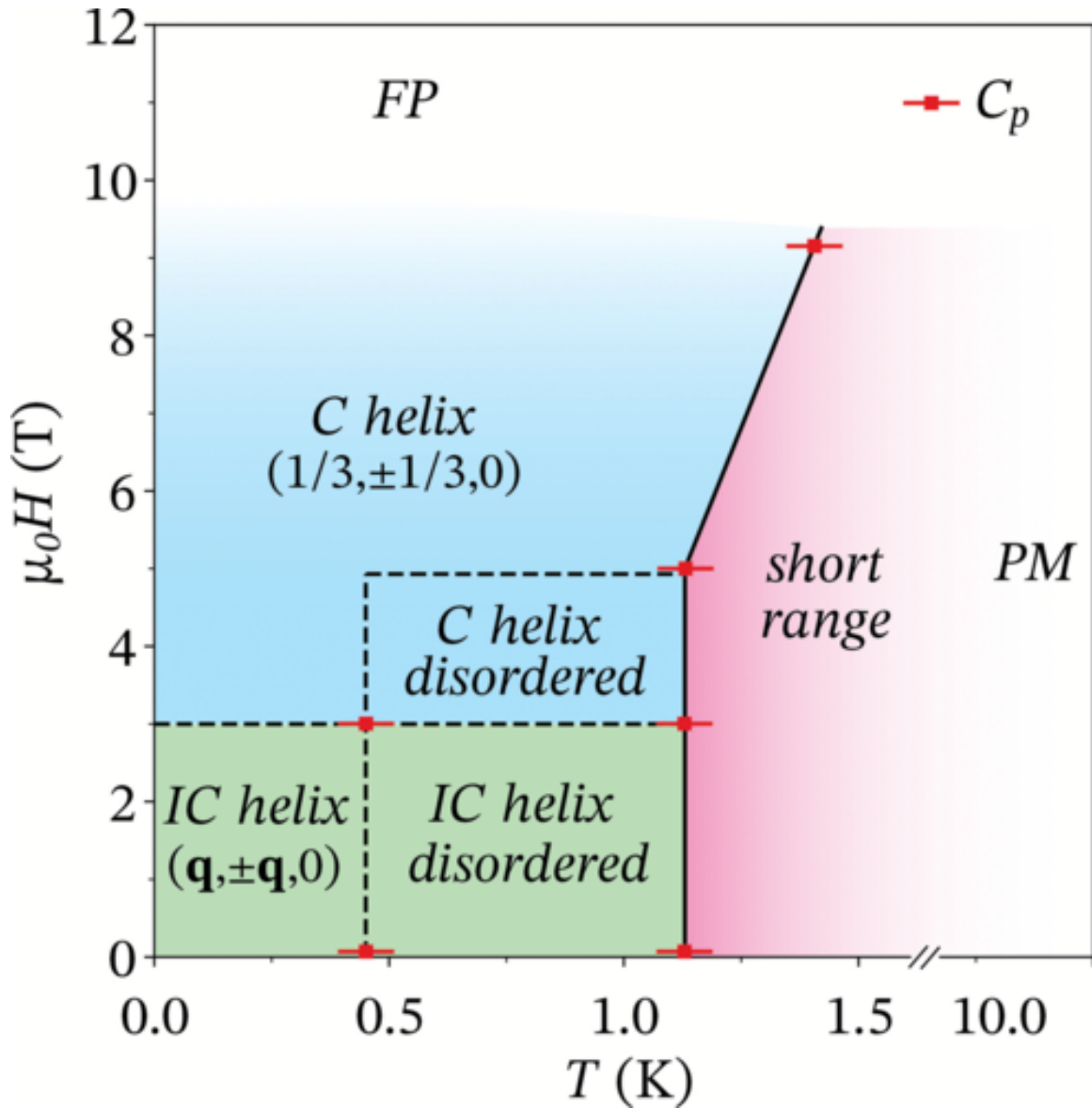


Figure 4-15: Proposed phase diagram of LiYbO₂, from our original paper [11]. Red dots correspond to transitions in the specific heat C_p . “IC helix disordered” refers to the intermediate state where both sublattices incommensurately order with $(q, \pm q, 0)$, but a disordered phase difference between sublattices. This phase difference remains disordered in the field-induced commensurate state.

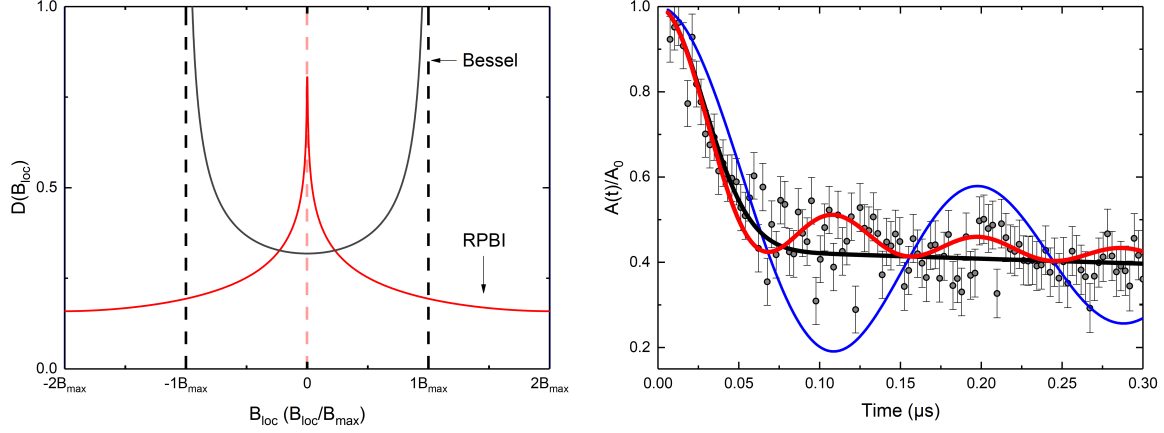


Figure 4-16: **(Left)** Field distributions $D(B_{\text{loc}})$ for a simple incommensurate magnet (Bessel) and the RPBI distribution, as described in the text. **(Right)** Asymmetry plots at $T = 550$ mK plotted against the Bessel and Bessel squared polarization functions described in the text. The parameters used are obtained from the shown Gaussian fit. For the Bessel polarization, we take $\gamma_{\mu} B_{\text{max}} = \sqrt{2}\sigma$ in accordance with the short-time expansions of J_0 and $e^{-\frac{\sigma^2 t^2}{2}}$.

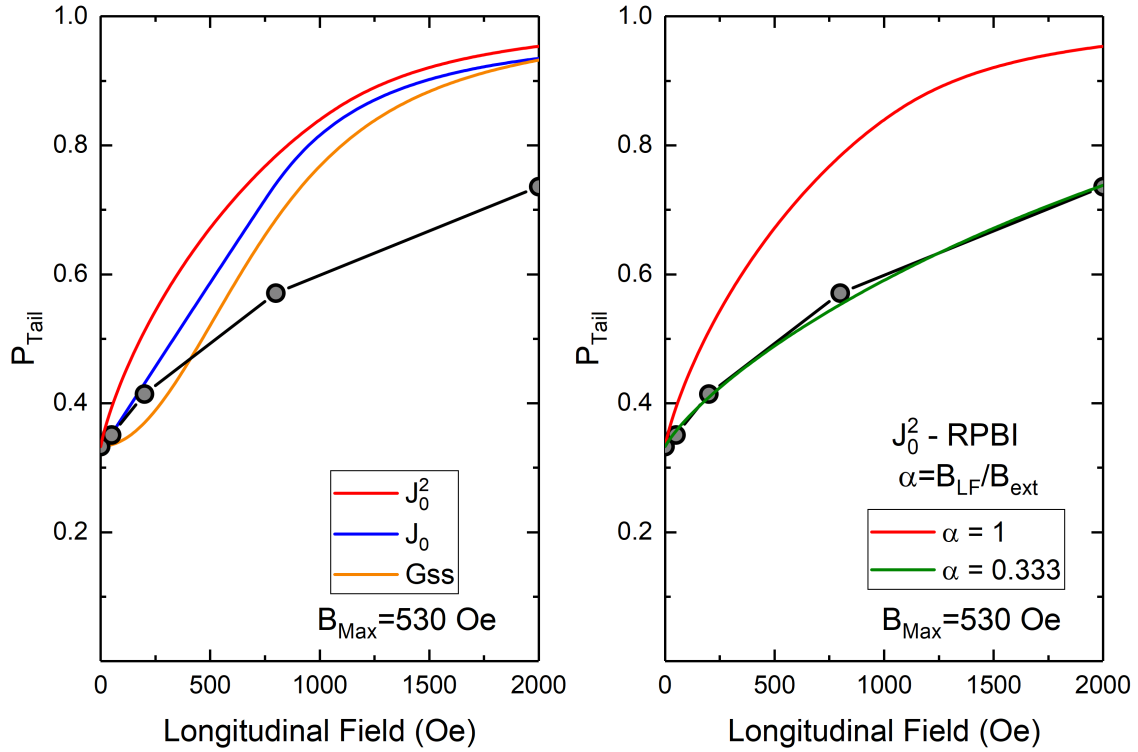


Figure 4-17: **(Left)** Longitudinal field dependence of the static tails for LiYbO_2 . The grey points correspond to the experimental data. Overlaid is the calculated LF dependence for the field distributions in the text, given the fit parameters extracted from the fit at 0.28 K. The internal field values are derived from the fitted depolarization rate. The lack of high-field agreement in any model indicates the presence of dynamics, despite the gaussian-like line-shape in zero-field. **(Right)** The LF tail recalculated using a linearly screened field with $f = 1/3$.

Chapter 5

Frustrated Magnetism in Cu_2IrO_3 and $\text{Ag}_3\text{LiIr}_2\text{O}_6$

Key Publications

*Coexistence of Static and Dynamic Magnetism in the Kitaev
Spin Liquid Material Cu_2IrO_3
Phys. Rev. B, Sept. 2019.*

*Effect of Structural Disorder on the Kitaev Magnet $\text{Ag}_3\text{LiIr}_2\text{O}_6$
Phys. Rev. B, March 2021.*

5.1 Introduction

Honeycomb lattices occupy a place of special importance in the field of frustrated magnetism. It was the publication of the exactly solvable Kitaev $S = 1/2$ honeycomb model that started the intense search for QSL candidates satisfying the Kitaev model [1]. Some of the most promising and well-studied systems are Kitaev honeycombs, such as α - RuCl_3 , Li_2IrO_3 , and Na_2IrO_3 . Most of these systems have been eliminated as true QSL candidates because they magnetically order. In 2018 our own Prof. Tafti successfully synthesized a new member of the Kitaev honeycomb family, Cu_2IrO_3 [2]. This material formed the basis of a new chemical family for exploring magnetic frustration on $J_{\text{eff}} = 1/2$ honeycomb lattices, including the material $\text{Ag}_3\text{LiIr}_2\text{O}_6$ (ALIO).

Initial bulk characterization of Cu_2IrO_3 was promising, with good lattice quality and no obvious signs of long-range order. X-ray diffraction showed that the kagome lattices of Cu_2IrO_3 were significantly closer to their ideal geometry with 120° bond angles (figure 5-1). Prior Iridates, Li_2IrO_3 and Na_2IrO_3 , had distorted honeycombs which created anisotropies that were likely responsible for their long-range ordering. Specific heat showed no peaks down to 2.7 K—as opposed to its parent compound Na_2IrO_3 which has a clear AFM peak at 15 K. A weak inflection at 2.7 K in Zero-field magnetic susceptibility χ suggested a possible ordering transition, though this feature was easily suppressed by weak fields and was only a tiny fraction of large signal that increased strongly with decreasing temperature. Naturally, this material warranted more investigation.

$\text{Ag}_3\text{LiIr}_2\text{O}_6$ (ALIO) is a sibling of Cu_2IrO_3 .¹ ALIO is structurally similar to Cu_2IrO_3 , where the Ir^{4+} ions form a honeycomb lattice intercalated by non-magnetic ions (Li/Cu, respectively). Unlike Cu_2IrO_3 , we find that synthesis conditions can be adjusted in order to induce extended row-defects of Ag ions within the honeycomb planes. The effects of extended defects on Kitaev systems and their bulk properties are not well understood, and in some cases may give misleading results. A comparative

study of extended defects in high-quality samples is called for.

The local probe technique of Muon Spin Rotation/Relaxation/Resonance (μ SR) is well known for its ability to eliminate QSL candidates and characterize disordered magnetism. In this section we discuss the μ SR measurements we performed on Cu_2IrO_3 and $\text{Ag}_3\text{LiIr}_2\text{O}_6$. Our measurements showed that Cu_2IrO_3 is magnetically inhomogeneous with a near 50/50 split between spin frozen and a highly dynamic domains at 50 mK. Supplemental measurements performed by our collaborators showed that Cu_2IrO_3 suffers from charge-state disorder, which results in a sizable fraction of the honeycomb spins transferring to copper sites. Our μ SR measurements on ALIO, on the other hand, revealed an incommensurately ordered phase whose experimental signatures are heavily suppressed by structural defects.

We conclude that Cu_2IrO_3 is proximate to a QSL state, and theorize that the ground state of Cu_2IrO_3 may form an inhomogeneous QSL state. We conclude that $\text{Ag}_3\text{LiIr}_2\text{O}_6$ is long-ranged ordered in its ground state. We also conclude, from our measurements on ALIO, that extended lattice defects, such as rows of Ag inclusions, that the standard thermodynamic signatures of a magnetic transition in Kitaev systems can be heavily suppressed despite long range order.

5.2 Cu_2IrO_3

5.2.1 Characterization Cu_2IrO_3

Tafti Lab and our collaborators thoroughly characterized Cu_2IrO_3 using several techniques in order to verify the crystallographic and electronic structure of the samples [3]. Upon initial synthesis powdered X-ray diffraction was used to verify the overall structure and stoichiometry of the samples. Scanning Electron Transmission Microscopy was used to characterize the detailed structure and characterize lattice defects. X-ray absorption near-edge spectroscopy (XANES) was used to probe the charge states of

¹Both are members of the Delafossite-Iridate family with chemical formula $\text{A}_3\text{B}\text{Ir}_2\text{O}_6$, which reduces to A_2IrO_3 when $\text{A}=\text{B}$. The relationship between $\text{Ag}_3\text{LiIr}_2\text{O}_6$ and Cu_2IrO_3 can be clarified by rewriting their chemical formulas as $\text{Ag}_3(\text{LiIr}_2)\text{O}_6$ and $\text{Cu}_3(\text{CuIr}_2)\text{O}_6$, which emphasizes the chemical composition of the iridium-honeycomb planes.

Cu and Ir ion in order to directly confirm the presence of Ir⁴⁺ with $J_{\text{eff}} = 1/2$. Density Functional Theory (DFT) was used to confirm the results of XANES.

Electron transmission microscopy (STEM) shows perfect honeycomb lattices with no site-mixing or distortions (figure 5-2). STEM shows the presence of numerous stacking faults along the c -axis which form a "zig-zag" pattern. The stacking faults are a form of crystal twinning where adjacent layers may rotate and orient themselves along either $[1\ 0\ 0]$, $[1\ 1\ 0]$, or $[\bar{1}\ 1\ 0]$. The ideal Kitaev system is 2D and should not be affected by rotational stacking faults. While we did not pursue this idea further in our measurements, control of stacking faults would provide a way to test the two-dimensionality of the spin-physics in Cu₂IrO₃, as was done in Ag₃LiIr₂O₆ [4].

X-ray absorption near-edge spectroscopy was performed in order to confirm that honeycomb layers are comprised of magnetic Ir⁴⁺, $J_{\text{eff}} = 1/2$, ions. We expected that the Ir ions in the honeycomb planes would exist in the Ir⁴⁺ oxidation state due to the requirement of charge neutrality in the unit cell.² The Ir⁴⁺ should be magnetic with $J_{\text{eff}} = 1/2$ due to a combination of crystal electric field splitting and the spin-orbit interaction resulting in a single unfilled t_{2g} level [5]. But, charge and coordination arguments also allow the possibility of Cu²⁺ and Ir³⁺ ions in the unit cell. In this case Ir³⁺ would be non-magnetic. At the same time, Cu²⁺ is trivially magnetic with $S = 1/2$ ([Cu²⁺]=[3d9]) while Cu⁺ is trivially non-magnetic ([Cu⁺]=[3d10]). Our μ SR results, as discussed later, indicated magnetic inhomogeneity which can be explained by charge-state inhomogeneity.

To clarify the charge-structure of Cu₂IrO₃, XANES K-edge and L-edge was performed. Cu K-edge showed roughly 8.5% Cu²⁺ content while L-edge showed approximately 13% Cu²⁺ content. This gives an estimation of a roughly 20% non-magnetic impurity fraction of Ir³⁺ and a 10% $S = 1/2$ impurity of Cu²⁺. Ir L-edge was then

²Oxygen is almost always O²⁻ as a general principle. (O²⁻)₃ gives a total charge of -6 which must be balanced by Cu₂Ir. The preferred oxidation states of iridium are Ir⁴⁺ and Ir³⁺, while for copper the preferred states are Cu⁺ and 3. Charge conservation then requires that a unit cell either contains two Cu and one Ir⁴⁺, or one Cu⁺, one Cu²⁺, and one Ir³⁺. Cu ions normally are linearly coordinated as "dumbbells," which is observed in Cu₂IrO₃, while Cu²⁺ tends to coordinate in square-planar structures. The former is compatible with both the A and B sites in the A₃(BX₂)O₆ structure, while the latter is compatible with only the Cu²⁺ sites.

performed, which confirmed that roughly 20 % of iridium was in the Ir^{3+} state.

Density functional theory (DFT) calculations were also performed using the VASP code to confirm the crystallographic structures, which were observed directly using STEM and X-ray diffraction, as well as to confirm the oxidation states measured by XANES. DFT calculations yielded a Cu^{2+} content of 12 %, which agreed well with the Cu L-edge spectroscopy. These results were combined with electron energy loss spectroscopy (EELS) to show that the Cu^{2+} spin-impurities exist purely in the honeycomb layers. This was done by comparing Cu_2IrO_3 spectra to spectra from $\text{Cu}_{1.5}\text{Na}_{0.5}\text{SnO}_3$ and $\text{Cu}_{1.5}\text{Li}_{0.5}\text{SnO}_3$. These are non-magnetic structural analogues to Cu_2IrO_3 , including the presence of stacking faults. In these materials Cu is restricted to interplanar sites and the Cu^+ state; spectra comparisons allows us to deduce that Cu^{2+} exists in the honeycomb planes.

In summary, Cu_2IrO_3 has crystallographically nearly ideal iridium honeycomb structures that are marred by oxidation-state disorder. Roughly 20 % of the iridium ions are non-magnetic, with the missing spin being transferred to a neighboring Cu site. Additionally, Cu_2IrO_3 hosts a large number of stacking faults along the *c*-axis. Ideally, the presence of stacking faults should not affect the 2D Kitaev physics we are searching for, but no real system is ideal. The former point, the mixing of oxidation states creating magnetic disorder has a significant effect on the ground state of Cu_2IrO_3 , as we will see in our μSR results.

5.2.2 Experimental Cu_2IrO_3

μSR measurements were performed at the ISIS Pulsed Muon Source at the Rutherford Appleton Laboratory using the EMU and MuSR spectrometers. The Cu_2IrO_3 sample consisted of a packed-powder disc 8 mm in diameter and 1.9 mm in thickness, and then wrapped in 12.5 μm thick silver foil and mounted onto a silver plate. The same sample was measured in both EMU and MuSR. In EMU, the sample was placed into a dilution refrigerator for low-temperature measurements $50 \text{ mK} < T < 4.5 \text{ K}$ (and calibration data at $T = 16.4 \text{ K}$). In MuSR, the sample was placed into a helium exchange cryostat for wide temperature range measurements between $1.7 \text{ K} < T < 20 \text{ K}$ (with

calibration data taken at 50 K).

Signal backgrounds for the data was measured to be approximately 40 % in EMU and 76 % in MuSR. The large background in the EMU data set is a result of the spectrometer's "flypast" mode, while in MuSR the large background is a result of using a large beam-spot size. In our data the non-relaxing backgrounds are subtracted off and renormalized using the initial asymmetry at high temperatures. Data was fit using the WIMDA software package.

5.2.3 Results Cu_2IrO_3

Zero-field polarization as a function of temperature is plotted in figure 5-3. Strong magnetism sets in near 10 K, with the spectra exhibiting a strong depolarization at early times, followed by a slow relaxation at longer times. Between 10 K and 50 mK we fit the polarization as the sum of a fast component and a slow component:

$$P(t) = G_{KT}(t) (f \exp(-\lambda_{fast}t) + (1 - f) \exp(-\lambda_{slow}t)) \quad (5.2.1)$$

The rapid depolarization is too fast to be fully captured by the detectors at ISIS, but a small tail can be seen at early times. To capture the fast component, we fit the data of several low-temperature spectra at short times using an exponential function over several spectra as $\lambda_{fast} = 9(3) \mu\text{s}^{-1}$ and leave this as a fixed constant for the rest of the spectra. The slow component is well captured by pulsed source detectors at ISIS, which excel at measuring slow depolarizations, and is fitted as a function of temperature as shown in figure 5-1. By plotting the rapidly depolarizing fraction f and the slow depolarization rate λ_{slow} , we observe a clear magnetic crossover at 10 K. Both parameters grow monotonically with decreasing temperature before saturating near 2 K, with at $\lambda_{slow} \approx 0.5 \mu\text{s}^{-1}$ and $f \approx 0.55$ at 50 mK.

The muon is a volumetric probe, therefore equation 5.2.1 implies that either the sample is either magnetically inhomogeneous, or that the muon probes multiple magnetically inequivalent stopping sites in the crystallographic unit cell. It is unlikely that the muon can such radically different magnetic environments within a single unit

cell, therefore we interpret equation 5.2.1 as representing an inhomogeneous magnet. Therefore f represents the volume fraction of a distinct magnetic domain. The increase in f implies that the strongly magnetic phase expands at low temperatures relative to the weakly magnetic phase.

In figure 5-3e we show longitudinal field measurements at 500 Oe and 1000 Oe. Strong longitudinal field measurements can be used to discriminate between static and dynamic internal field distributions (see chapter 3). For a frozen spin distribution with relaxation rate λ , we expect the depolarization to be heavily suppressed by longitudinal fields of $B_{LF} \approx 5\lambda/\gamma_\mu$, [6]. Figure 5-3e shows that the fast component is indeed heavily suppressed; the missing asymmetry at short-times is recovered as a non-depolarizing background.

Long-range magnetic ordering (LRO) can be almost ruled out via a simple estimate of the internal field distribution combined with the lack of a sharp magnetic transition. From the LF response of the tail at 500 Oe and 1000 Oe, we can estimate an internal field strength of roughly 500 Oe. For a LRO magnet, this would correspond to the average local field probed seen by the muon and would result in cosine oscillation with frequency $B_{loc}/2\pi \approx 6.5$ MHz. This is easily within the 10 MHz limit of the ISIS beamlines [7]. For a spin-frozen system, the estimated internal field strength would correspond roughly to the variance (or second-moment) of the internal field-distribution, which would be centered about $B_{loc} = 0$ Oe. It is possible that the signal is a heavily damped oscillation, which would be a combination of LRO and disordered magnetism. But considering that we observe a logarithmic crossover with no indication of a thermodynamic transition, the static phase is most likely a disordered spin-frozen state.

The slow fraction shows virtually no decoupling at all between 500 Oe and 1000 Oe, though the depolarization rate is slightly reduced. Similar to the fast component, we would expect the slow component to be decoupled by fields of $\lambda_{slow}/\gamma_\mu \approx 25$ Oe if no dynamical process are at play. If dynamical process are present though, the strong collision theory for muon depolarization states that longitudinal field dependence of

λ_{slow} should vary as [6]

$$\lambda_{\text{slow}} \approx \frac{2\gamma_{\mu}^2 \Delta^2 \nu}{\gamma_{\mu} B_{\text{LF}}^2 + \nu^2} \quad (5.2.2)$$

where ν is the collision rate of the hard-collision model, and $\nu \gg \gamma_{\mu} \Delta$ where Δ is the characteristic internal field distribution for $\nu = 0$. Fitting the LF1000 spectra (figure 5-3e) shows that λ_{slow} is reduced by 10% at most from ZF. This puts a minimum bound of approximately 260 MHz on ν , which in turn gives a lower bound of $\Delta \approx 100$ Oe for the internal field strength. The internal field parameter Δ , while smaller than what is observed for the fast component, is still clearly corresponds to a magnetic spin system. We interpret the dynamical signal as spin-fluctuations.

For perspective on the value of ν : ν is smaller compared to most conventional dynamical systems, which operate in GHz-THz range [8]. Low-frequency "persistent dynamics" in the mK range are frequently seen in QSL candidates—the pyrochlores and spinels being good examples [9]–[11]. The rates though, are roughly between 0.1 MHz \approx 10 MHz. Similarly, new μ SR measurements have very recently been published for $\text{Ag}_3\text{LiIr}_2\text{O}_6$ —a closely related Iridate that we'll be discussing shortly—and these measurements found a persistent fluctuation rate of 2 MHz at 50 mK.³ The dynamical rate of ≥ 260 MHz is about 100 \times larger than the rates observed for similar systems.

Finally, we note that the transition temperature $T_c \cong 10$ K and the plateau at $T \cong 2$ K matches with observations in magnetic susceptibility. DC Magnetic susceptibility measurements show an onset of hysteresis at 10 K and a small peak at 2 K (figure 5-3d). Hysteresis is a signature—but not proof—of various types of spin-freezing processes, including long-range order, spin-glass transitions, and frozen uncorrelated spins.

5.2.4 Discussion Cu_2IrO_3

The μ SR results show that the sample is magnetically inhomogeneous at 50 mK, with a near 50/50 split between domains of frozen spins and domains of rapidly fluctuating

³Although $\text{Ag}_3\text{LiIr}_2\text{O}_6$ is incommensurately long-ranged ordered, and not spin-frozen or inhomogeneous. So the comparison isn't exactly 1:1.

spins. This split can be understood in part by the detailed characterization performed on the oxidation states of iridium and copper in the honeycomb planes.⁴ While structurally perfect, the honeycomb planes suffer from severe charge defects, causing 20 % of the iridium spins to transfer to the in-plane copper ions. It is easy to imagine that these defects break the spin-frustration of the remaining Ir^{4+} ions, resulting in a disordered frozen-spin ground state.

A closer inspection shows that this explanation is incomplete. A two component polarization is easily explained by Cu^{2+} inducing magnetic inhomogeneity within Cu_2IrO_3 , and it explains why one of the magnetic phases is disordered. It does not explain why the other phase is so intensely dynamic at 50 mK. The estimated fluctuation rate of $\nu \geq 260$ MHz is abnormally high for a spin system at 50 mK, let alone one that is partially frozen by frequent defects. It is known that frustrated spin systems frequently retain some level of persistent dynamics at ultra-low temperatures ($T \approx 50$ mK), even after magnetically ordering. But the persistent dynamics seen in such systems are closer to the quasi-static limit with rates ranging between roughly 1 MHz to 10 MHz.

As a final point, we mention the work of Choi et al on Cu_2IrO_3 whose preprint was published to arXiv at about the same time our preprint was. Choi et al also show similar measurements to our own [12] and observed a purely dynamical signal. We note that they synthesized their samples according to the method previously published by Prof. Tafti [2]. The discrepancy is still unresolved. That said, very recently a third group (Pal et al) confirmed our observations as part of a Raman study on polycrystalline samples they synthesized themselves [13]. Additionally, Pal et al observed anomalies in their Raman spectra that are consistent with the fractionalization of Majorana fermions predicted for the Kitaev model, and theorize that Cu_2IrO_3 is an inhomogeneous QSL. It is possible that small defects in the lattice may suppress the formation of Cu^{2+} and Ir^{3+} , leading to a phase-homogeneous system, instead of the magnetically inhomogeneous state we observed [2]. More research is needed to

⁴These characterizations were performed *after* the μSR experiments in order to explain the μSR data.

understand the ground state of Cu_2IrO_3 , which still remains a promising new system despite the presence of phase inhomogeneity.

5.3 $\text{Ag}_3\text{LiIr}_2\text{O}_6$

5.3.1 Characterization $\text{Ag}_3\text{LiIr}_2\text{O}_6$

The synthesis of $\text{Ag}_3\text{LiIr}_2\text{O}_6$ (ALIO) is sensitive to the quality of the precursor material, $\alpha\text{-Li}_2\text{IrO}_3$, as well as the duration of the topotactic reaction used to synthesize ALIO. The structure is similar to Cu_2IrO_3 , with Ag taking the place of Cu in forming the dumbbell structures that connect together the Ir planes. Consequently, ALIO lacks the “buckling” structure seen in Cu_2IrO_3 (figure 5-1). Instead, the Ag dumbbells are straight, forming a more regular crystallographic structure. This, presumably, should reduce the effects of the Dzyaloshinskii-Moriya interaction. Additionally, Ag only has a single main oxidation state (+1) as opposed to the two main oxidation states of Cu (+1, +2). As such, the charge-state disorder seen in Cu_2IrO_3 is not expected to occur in ALIO.

$\text{Ag}_3\text{LiIr}_2\text{O}_6$ shows two types of defects: stacking defects and extended row defects. Stacking defects occur as rotations along the \hat{c} axis, similar to Cu_2IrO_3 . Row defects occur where the iridium honeycomb lattice is replaced by rows of Ag ions. Silver row defects occur as a function of detailed synthesis conditions. While difficult, our collaborators at Tafti lab managed to refine the synthesis process and produce pristine samples of ALIO [2], [4]. We leveraged this in order to report on the effects of extended structural defects on the Iridate kitaev lattice.

Tafti lab synthesized two different batches of ALIO: S1, which was a “clean” system with no Ag inclusions and pristine Ir honeycombs, and a “dirty” system with many Ag inclusions. Both samples suffered from stacking faults, similar to Cu_2IrO_3 , though we ultimately concluded that the presence of stacking faults does not appreciably affect the magnetism in the Ir^{4+} layers. Characterization was performed using a combination of x-ray diffraction and high-angle annular dark field scanning TEM

(HAADF-STEM).

X-ray spectra was performed in-house using a Bruker D8 ECO instrument in order to characterize the presence of structural disorder. Figure 5-4a shows a comparison of the spectra for S1 and S2. We see a broadening of peak, which is indicative of strong structural disorder. STEM measurements of the lattice (figure 5-4b) directly reveal the nature of the disorder. We see that in S2 the Ir ions (bright pairs of points) are occasionally replaced by rows of Ag ions (dense small rows of points.) Additionally, we see the presence of stacking faults similar to Cu_2IrO_3 . We note that the parent compound, $\alpha\text{-Li}_2\text{IrO}_3$ also shows these defects, though they are much more frequent in ALIO. The stacking faults are present in both S1 and S2, but the measured magnetic order in S1 is similar to that of $\alpha\text{-Li}_2\text{IrO}_3$ [14], therefore we conclude that the magnetic ground state is not strongly affected by the presence of stacking faults. The presence of Ag inclusions, as we will show, does strongly affect the observed bulk magnetic properties of ALIO.

5.3.2 Experimental $\text{Ag}_3\text{LiIr}_2\text{O}_6$

μSR measurements were performed at the Paul Scherrer Institute (PSI) continuous muon source. Measurements of sample S1 were performed in a ^3He refrigerator using the Dolly spectrometer General Purpose Spectrometer (GPS) using a gas-flow cryostat. Sample S2 was measured similarly in GPS. The S1 sample consisted of a packed pellet measuring 13 mm in diameter and 1 mm thick. Sample S2 was 13 mm in diameter and 1.2 mm thick. Both were wrapped in 25 μm thick silver foil and attached onto copper sample holders using GE Varnish. Finally, we note that sample S2 was initially measured several months earlier in both a dilution refrigerator and a gas-flow cryostat at the Appleton Rutherford Lab ISIS Pulsed Muon source, using the EMU and MuSR spectrometers. The sample background in MuSR was estimated using an identically sized Cu plate mounted on an aluminum sample holder. The background in MuSR was estimated as $\approx 40\%$ while in EMU it is estimated at 76% .

5.3.3 Results $\text{Ag}_3\text{LiIr}_2\text{O}_6$

Both samples S1 and S2 show signatures of strong magnetism at temperatures below roughly 10 K. Figure 5-5 plots the short-time asymmetry spectra of sample S1 at several representative temperatures. We see that the depolarization is essentially flat at 20 K, indicating rapidly fluctuating Ir^{4+} moments in the paramagnetic regime. As temperature is reduced, a rapid depolarization sets in, becoming prominent at 10 K. Near 7 K, spontaneous oscillations begin to appear, and by 300 mK, oscillations indicating long-range order are clearly resolved. We fit these oscillations to a Bessel function, which indicates incommensurate long-range magnetic order [6].

We fit the S1 spectra to

$$A_{LRO}(t) = A_0 \left(f_{\alpha_F} e^{-\lambda_1 t} * J_0(\gamma_\mu B_{\max} t) + (1 - f_{\alpha_F}) e^{-\lambda_2 t} \right), \quad (5.3.1)$$

where J_0 is the 0th order Bessel of the first kind. Physically, B_{\max} represents the maximum internal field observable by the muon in an incommensurate field distribution. The parameter B_{\max} is, to approximation, dependent only on the dipole moment size for a given LRO and spin-density.⁵ Therefore B_{\max} is approximately constant with temperature, as shown in figure 5-6a. Above 8 K the oscillations are no longer visible due to the high damping rate and small fraction volume fraction, α_F . Therefore we keep B_{\max} fixed as a function of temperature above 8 K. Figure 5-6a plots the two parameters together.

Overlaying spectra for S1 and S2 in figure 5-6 shows qualitatively different spectra at $T = 10$ K, but surprisingly similar spectra at $T = 1.6$ K. At 1.6 K, the oscillations in the S2 spectra are heavily damped barely resolvable, but roughly line up with spectra S1. The depolarization envelope of S2 roughly lines up with S1 at 1.6 K. This implies that sample S2 hosts the same low-temperature incommensurate order

⁵This is because the muon stops at a fixed site within the crystallographic unit cell, while the magnetic order is incommensurate with the unit cell. Therefore the muon samples the entire internal field distribution of the incommensurate order, provided that the internal field distribution is isotropic and that the muon is far enough away from the moments to ignore $\frac{1}{r^3}$ divergences.

as sample S1 (with the same B_{\max} parameter), but that there is additional magnetic disorder at the local level which heavily dampens the oscillations, and alters the polarization function above 10 K.

Longitudinal Field (LF) measurements (figure 5-7) show that the depolarization is decoupled by LF fields comparable to B_{\max} , which confirms the internal field distribution is static [6], [8]. By fitting the LF dependence of the long-time ($t \rightarrow \infty$) tail asymmetry, we can estimate the approximate internal field strengths [6], [15]. In particular, for a commensurate polycrystalline magnet, the mid-point of asymmetry restoration occurs at $B_{\text{LF}}/B_{\text{int}} = 4/3$ [15]. We use this to estimate the local field at the muon site as $B_{\text{loc}} \approx 263$ Oe for S1 and $B_{\text{loc}} \approx 111$ Oe for S2. For an incommensurate magnet, this is proportional to B_{\max} . This would imply that sample S2 should depolarize slower and oscillate slower than sample S1 because they're both incommensurate magnets. This is not observed, with sample S2 having a similar depolarization envelope, and apparent oscillation rate, to sample S1 (figure 5-6b) at $T = 1.6$ K.

5.3.4 Discussion $\text{Ag}_3\text{LiIr}_2\text{O}_6$

Pristine samples of ALIO clearly undergo long-range magnetic order, albeit rather slowly over a 4 K to 5 K range. At first glance the dirty samples do not appear to host LRO, as there are no obvious spontaneous oscillations in ZF. The peaks in the spectra can be interpreted as Kubo-Toyabe repolarization to a 1/3rd tail (see chapter 3). But a quick comparison with the spectra of S1 quickly shows that is not the case; the previously inscrutable features of S2 are overdamped oscillations.

HAADF-STEM images show that the dirty samples have extended Ag impurities replacing portions of the honeycomb lattice. While the Kitaev honeycomb model is stable with respect to point defects, it is not stable with respect to extended defects [16]. The parent compound of ALIO, $\alpha\text{-Li}_2\text{IrO}_3$, is now known to host incommensurate spiral order. It is highly likely that $\text{Ag}_3\text{LiIr}_2\text{O}_6$ forms the same incommensurate spiral order as its parent compound [14].

One oddity of the depolarization is how well the overall depolarization envelopes match-up between samples in the ordered state. From LF measurements we expect

two different B_{max} parameters for each sample. For incommensurate magnets, the oscillation rate and depolarization rate are intrinsically tied together, because Bessel functions naturally decay as $J_0(x) \approx 1/x$ for $x \gg 0$. This is an unusual decay envelope in μSR , where most decays follow an exponential-like decay. Despite this, the spectra at 1.6 K appear to have similar oscillation rates and similar depolarization envelopes. The match-up is exceptional considering that the samples were measured months apart at different facilities. It becomes even more striking when one compares the data at 10 K which show two clearly different systems.

The simplest explanation for this is that the rows of Ag inclusions cause a non-trivial modification to the local field sensed by the muon. Muons which stop near Ag impurities do not observe a simple disordered phase, nor a non-magnetic region. Rather than seeing regions of pure disorder or non-magnetism, the muons in the dirty sample likely see a distorted LRO that is beyond the scope of this text to describe. The difference, then, between samples S1 and S2 at 10 K would be the correlation length and field strengths of short-range correlations leading up to the ordering transition. At 1.6 K, both systems are LRO, but the muon senses a distorted internal field distribution that yields highly damped oscillations, but a similar decay rate.

Bulk probes did not show long-range order in sample S2. Magnetic susceptibility and magnetic heat-capacity showed a distinct lack of a magnetic transition in the dirty samples S2, while a two step entropy release (figure 5-8) was originally observed in the heat capacity of S1. The two-step entropy release was taken as a sign of a Kitaev honeycomb spin liquid.⁶ [17] The clean S1 samples showed signs of LRO, with anomalies in χ at $T_N = 14$ K and $T_{\text{LRO}} = 8$ K. Our μSR studies have showed that these anomalies correspond to the onset of strong magnetism (likely short-range correlations) at 14 K, and LRO at 8 K in both samples. By comparing the bulk data of S1 to the μSR data of S1 and S2, we can confirm that both samples enter a long-range ordered, spin-frozen, phase, despite the original interpretation of S2 as a spin-frustrated system [17].

⁶It is believed that the Kitaev QSL model may show a signature “two-step” entropy release due

We note that this is not the first time that bulk-measurements on Kitaev systems have given misleading results. α -Li₂IrO₃, Na₂IrO₃, and α -RuCl₃ all show similar C_m figures, which have in the past been interpreted as signs of quasi-particle fractionalization into Majorana fermions [18], [19]. Similarly, another promising QSL candidate, H₃LiIr₂O₆, has been reported to have a similar low temperature $\chi(T)$ to ALIO [20], and a similar structural disorder to ALIO [21]. In fact, this was the case for Cu₂IrO₃, which was first reported as completely lacking static magnetism due to smooth, Curie-Weiss, like χ and deceptive C_m figures [12]. Our study on higher quality samples proved that ALIO undergoes a conventional thermodynamic transition to a LRO state [3].

5.4 Conclusions

We used μ SR to study two new members of the Kitaev honeycomb family. Cu₂IrO₃ was a newly synthesized material that showed a promising lack of LRO in bulk-measurements to 1.8 K. μ SR measurements revealed that Cu₂IrO₃ is magnetically inhomogeneous, with the ground state being near evenly divided into frozen spin and fluctuating spin volumes down to 50 mK. Further analysis revealed that the charge states of Cu and Ir are disordered which results in spin-defects at roughly 20 % of the honeycomb sites. That said, the highly dynamic phase at 50 mK is highly unusual and Cu₂IrO₃ may still be proximate to a possible QSL phase.

Ag₃LiIr₂O₆ (ALIO) was another promising system that appeared to be highly frustrated when first synthesized [17]. As sample quality improved, μ SR revealed strong, static, magnetism in both high-quality and low-quality samples, along with clear long-range magnetic order. The extended rows of Ag defects in low-quality ALIO samples does not prevent long range order, but it does obscure the thermodynamic signatures of magnetic ordering and spin-freezing. Care must be taken in interpreting bulk-data for QSL candidates containing significant structural defects.

to the formation of Majorana fermion quasi-particles at T_H , followed by the long-range entanglement of the quasi-particles at T_L .

Together these measurements show the strength of μ SR in evaluating QSL candidates. As a volumetric local magnetic probe μ SR is sensitive to subtle forms of magnetic disorder that are not readily apparent in bulk probe measurements, such as magnetic susceptibility or specific heat. μ SR can reliably discriminate between magnetically inhomogeneous systems when the ground state is highly sensitive to defects and impurities, such as in a QSL system. This can be used to detect long-range magnetic order or spin freezing in disordered systems where bulk probes can't. In $\text{Ag}_3\text{LiIr}_2\text{O}_6$ we can see long-range order in samples were extended rows of Ag impurities disrupt the magnetic order and obscure the usual transitions in bulk probes. In Cu_2IrO_3 , we see a magnetically inhomogeneous system with domains of spin-frozen states coexisting with what appears to be spin-frustrated state down to 50 mK. For systems such as these, μ SR excels while bulk probes often given incomplete, or incorrect, pictures.

5.5 References

- [1] A. Kitaev, "Anyons in an exactly solved model and beyond," *Annals of Physics*, vol. 321, no. 1, pp. 2–111, 2006. DOI: 10.1016/j.aop.2005.10.005.
- [2] M. Abramchuk, C. Ozsoy-Keskinbora, J. W. Krizan, K. R. Metz, D. C. Bell, and F. Tafti, " Cu_2IrO_3 : A New Magnetically Frustrated Honeycomb Iridate," *Journal of the American Chemical Society*, vol. 139, no. 43, pp. 15 371–15 376, Nov. 1, 2017. DOI: 10.1021/jacs.7b06911.
- [3] E. M. Kenney, C. U. Segre, W. Lafargue-Dit-Hauret, *et al.*, "Coexistence of static and dynamic magnetism in the Kitaev spin liquid material Cu_2IrO_3 ," *Physical Review B*, vol. 100, no. 9, p. 094 418, Sep. 12, 2019. DOI: 10.1103/PhysRevB.100.094418.
- [4] F. Bahrami, E. M. Kenney, C. Wang, *et al.*, "Effect of structural disorder on the Kitaev magnet $\text{Ag}_3\text{LiIr}_2\text{O}_6$," *Physical Review B*, vol. 103, no. 9, p. 094 427, Mar. 17, 2021. DOI: 10.1103/PhysRevB.103.094427.

- [5] A. Shitade, H. Katsura, J. Kuneš, X.-L. Qi, S.-C. Zhang, and N. Nagaosa, “Quantum Spin Hall Effect in a Transition Metal Oxide Na_2IrO_3 ,” *Physical Review Letters*, vol. 102, no. 25, p. 256403, Jun. 24, 2009. DOI: 10.1103/PhysRevLett.102.256403.
- [6] A. Le Yaouanc and P. D. De Réotier, *Muon Spin Rotation, Relaxation, and Resonance: Applications to Condensed Matter*, ser. International Series of Monographs on Physics no. 147. Oxford: Oxford University Press, 2010, 486 pp., ISBN: 978-0-19-959647-8.
- [7] A. D. Hillier, D. J. Adams, P. J. Baker, *et al.*, “Developments at the ISIS muon source and the concomitant benefit to the user community,” *Journal of Physics: Conference Series*, vol. 551, p. 012067, Dec. 16, 2014. DOI: 10.1088/1742-6596/551/1/012067.
- [8] Y. J. Uemura, “ μSR relaxation functions in magnetic materials,” in *Muon Science: Muons in Physics, Chemistry, and Materials*, London: SUSSP Publications, Institute of Physics Publishing, 1999, ISBN: 0-7503-0630-0.
- [9] P. Dalmas de Réotier, A. Maisuradze, and A. Yaouanc, “Recent μSR Studies of Insulating Rare-Earth Pyrochlore Magnets,” *Journal of the Physical Society of Japan*, vol. 85, no. 9, p. 091010, Sep. 15, 2016. DOI: 10.7566/JPSJ.85.091010.
- [10] Y. Cai, M. N. Wilson, A. M. Hallas, *et al.*, “ μSR study of spin freezing and persistent spin dynamics in $\text{NaCaNi}_2\text{F}_7$,” *Journal of Physics: Condensed Matter*, vol. 30, no. 38, p. 385802, Aug. 2018. DOI: 10.1088/1361-648X/aad91c.
- [11] M. T. Rovers, P. P. Kyriakou, H. A. Dabkowska, G. M. Luke, M. I. Larkin, and A. T. Savici, “Muon-spin-relaxation investigation of the spin dynamics of geometrically frustrated chromium spinels,” *Physical Review B*, vol. 66, no. 17, p. 174434, Nov. 26, 2002. DOI: 10.1103/PhysRevB.66.174434.
- [12] Y. S. Choi, C. H. Lee, S. Lee, *et al.*, “Exotic Low-Energy Excitations Emergent in the Random Kitaev Magnet Cu_2IrO_3 ,” *Physical Review Letters*, vol. 122, no. 16, p. 167202, Apr. 26, 2019. DOI: 10.1103/PhysRevLett.122.167202.

- [13] S. Pal, A. Seth, P. Sakrikar, *et al.*, “Probing signatures of fractionalization in the candidate quantum spin liquid Cu_2IrO_3 via anomalous Raman scattering,” *Physical Review B*, vol. 104, no. 18, p. 184420, Nov. 17, 2021. DOI: 10.1103/PhysRevB.104.184420.
- [14] S. Choi, S. Manni, J. Singleton, *et al.*, “Spin dynamics and field-induced magnetic phase transition in the honeycomb Kitaev magnet $\alpha\text{-Li}_2\text{IrO}_3$,” *Physical Review B*, vol. 99, no. 5, p. 054426, Feb. 25, 2019. DOI: 10.1103/PhysRevB.99.054426.
- [15] F. L. Pratt, “Field dependence of μSR signals in a polycrystalline magnet,” *Journal of Physics: Condensed Matter*, vol. 19, no. 45, p. 456207, Oct. 11, 2007. DOI: 10.1088/0953-8984/19/45/456207.
- [16] W.-H. Kao, J. Knolle, G. B. Halász, R. Moessner, and N. B. Perkins, “Vacancy-Induced Low-Energy Density of States in the Kitaev Spin Liquid,” *Physical Review X*, vol. 11, no. 1, p. 011034, Feb. 18, 2021. DOI: 10.1103/PhysRevX.11.011034.
- [17] F. Bahrami, W. Lafargue-Dit-Hauret, O. I. Lebedev, *et al.*, “Thermodynamic Evidence of Proximity to a Kitaev Spin Liquid in $\text{Ag}_3\text{LiIr}_2\text{O}_6$,” *Physical Review Letters*, vol. 123, no. 23, p. 237203, Dec. 3, 2019. DOI: 10.1103/PhysRevLett.123.237203.
- [18] K. Mehlawat, A. Thamizhavel, and Y. Singh, “Heat capacity evidence for proximity to the Kitaev quantum spin liquid in A_2IrO_3 ($\text{A} = \text{Na}, \text{Li}$),” *Physical Review B*, vol. 95, no. 14, p. 144406, Apr. 7, 2017. DOI: 10.1103/PhysRevB.95.144406.
- [19] S. Widmann, V. Tsurkan, D. A. Prishchenko, V. G. Mazurenko, A. A. Tsirlin, and A. Loidl, “Thermodynamic evidence of fractionalized excitations in RuCl_3 ,” *Physical Review B*, vol. 99, no. 9, p. 094415, Mar. 14, 2019. DOI: 10.1103/PhysRevB.99.094415.

- [20] K. Kitagawa, T. Takayama, Y. Matsumoto, *et al.*, “A spin–orbital-entangled quantum liquid on a honeycomb lattice,” *Nature*, vol. 554, no. 7692, pp. 341–345, Feb. 2018. DOI: 10.1038/nature25482.
- [21] S. Bette, T. Takayama, K. Kitagawa, R. Takano, H. Takagi, and R. E. Dinnebier, “Solution of the heavily stacking faulted crystal structure of the honeycomb iridate $\text{H}_3\text{LiIr}_2\text{O}_6$,” *Dalton Transactions*, vol. 46, no. 44, pp. 15 216–15 227, 2017. DOI: 10.1039/C7DT02978K.

5.6 Figures

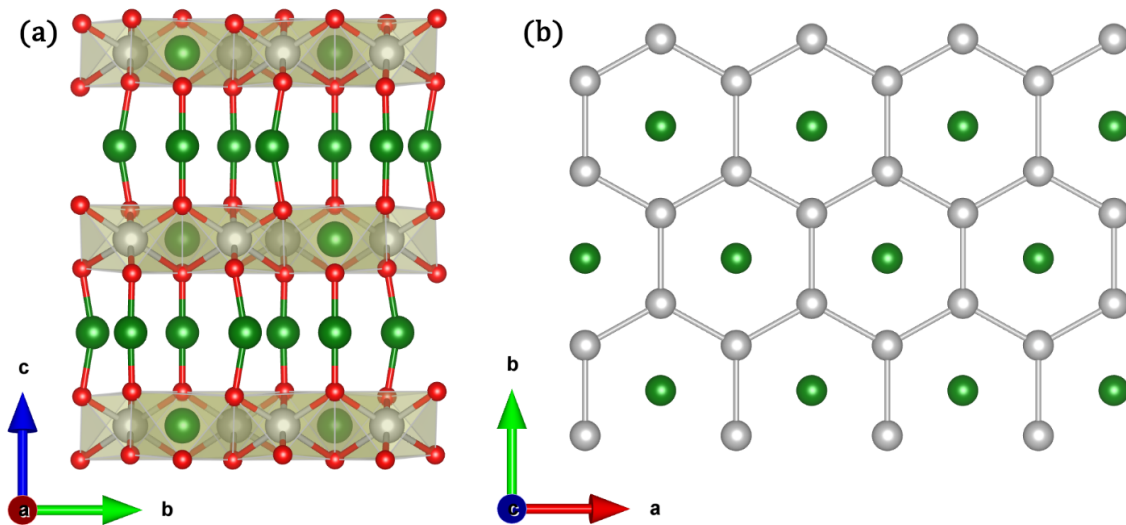


Figure 5-1: Structure of Cu_2IrO_3 . White = Iridium, Green = Copper, Red = Oxygen. (a) Layered structure of Cu_2IrO_3 illustrating iridium octahedra. Each layer is connected together via Cu dumbbells, which show a buckled structure. (b) Honeycomb lattice of iridium. The hexagon angles are close to the ideal value of 120° , with Rietveld refined angles of $118.74(7)^\circ/118.74(7)^\circ/122.5(1)^\circ$. Detailed structure parameters, including space group and lattice spacing, can be found in ref [2].

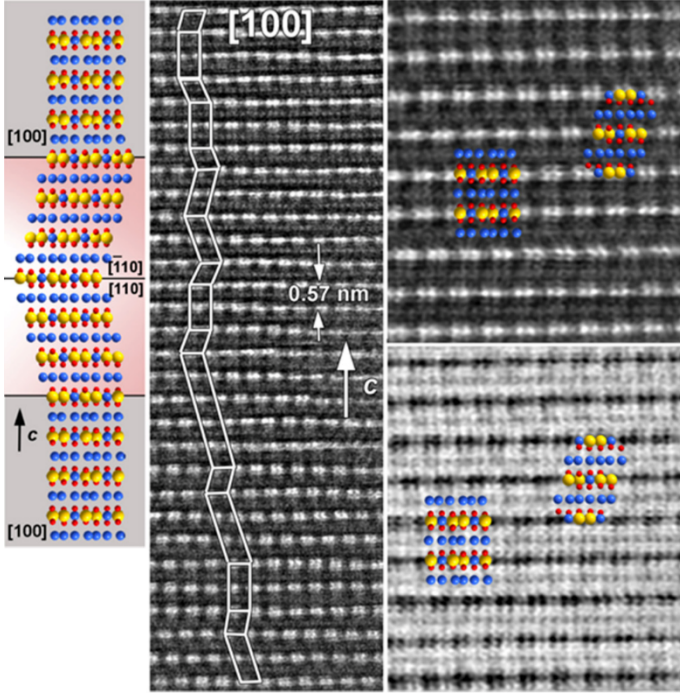


Figure 5-2: STEM images of Cu_2IrO_3 layers taken from ref [3]. Cu_2IrO_3 are shown; Yellow = Iridium, Blue = Copper, Red = Oxygen. The left-hand image is an illustration of the stacking faults along the c -axis. The middle panel shows a HAADF-STEM image along the c -axis, showing the zig-zag pattern formed by the stacking faults. The right-top and right-bottom are magnified HAADF-STEM and ABF-STEM images, respectively. Unitcells of Cu_2IrO_3 are overlaid for clarity. While we observe clear stacking faults along the c -axis, we do not observe disorder within the iridium planes themselves, indicating that the individual kitaev lattices are unaffected by stacking faults.

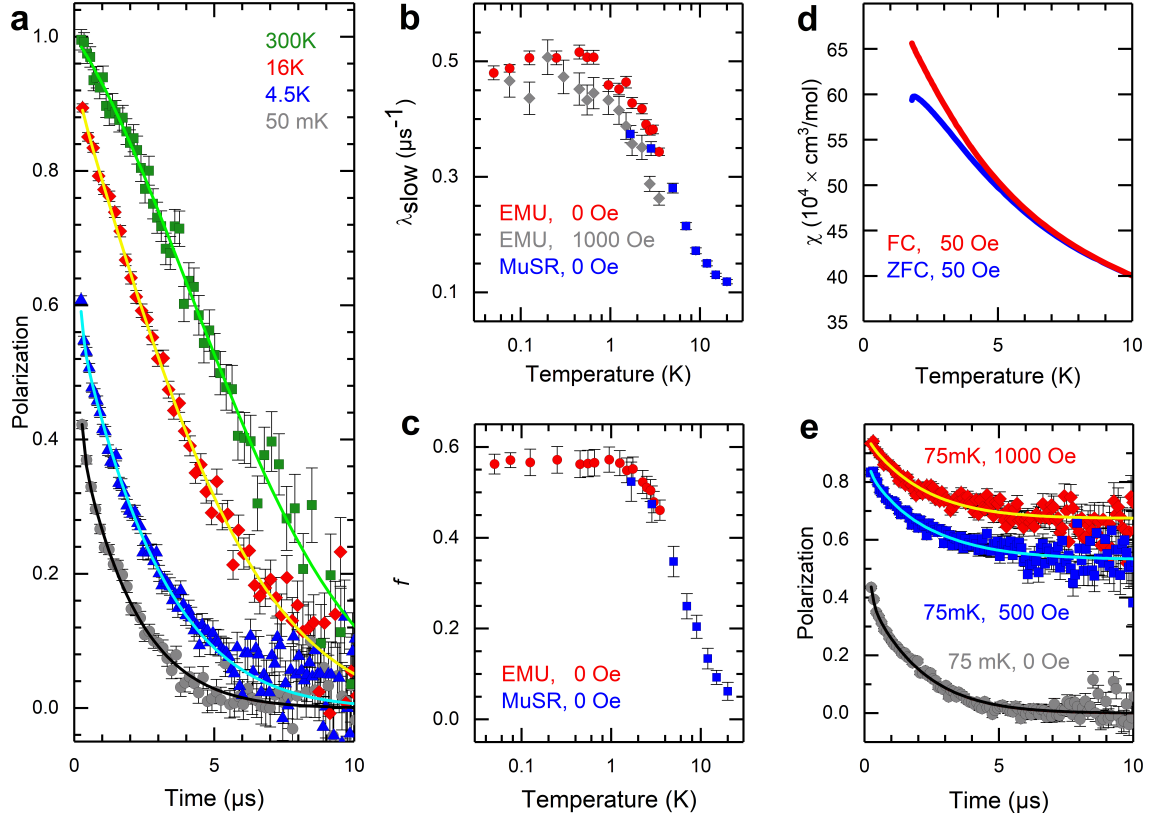


Figure 5-3: μ SR fit results of Cu_2IrO_3 , as originally published in ref [3]. (a): Zero-field polarization spectra of Cu_2IrO_3 between room temperature (300 K) and base temperature (50 mK). A strongly magnetic depolarization appears. (b) The depolarization rate λ_{slow} as a function of temperature. Measurements were taken in two spectrometers, EMU and MuSR. λ_{slow} plateaus near 1 K~2 K at roughly $\lambda_{\text{slow}} \cong 0.5 \mu\text{s}^{-1}$. λ_{slow} is weakly affected by applied LF fields. (c) Fast depolarization fraction f as a function of temperature. The fast fraction temperature dependence mirrors that of λ_{slow} . (d) Magnetic susceptibility measurements in 50 Oe showing hysteresis starting at 5 K and a peak near 2 K. (e) Longitudinal field (LF) polarization spectra at 0 Oe, 500 Oe, and 1000 Oe. The fast depolarization is quickly decoupled, but the slow depolarization rate remains nearly the same, illustrating that the rapid depolarization is due to static magnetism (frozen spins) while the slow depolarization is due to dynamic spins (rapidly fluctuating spins).

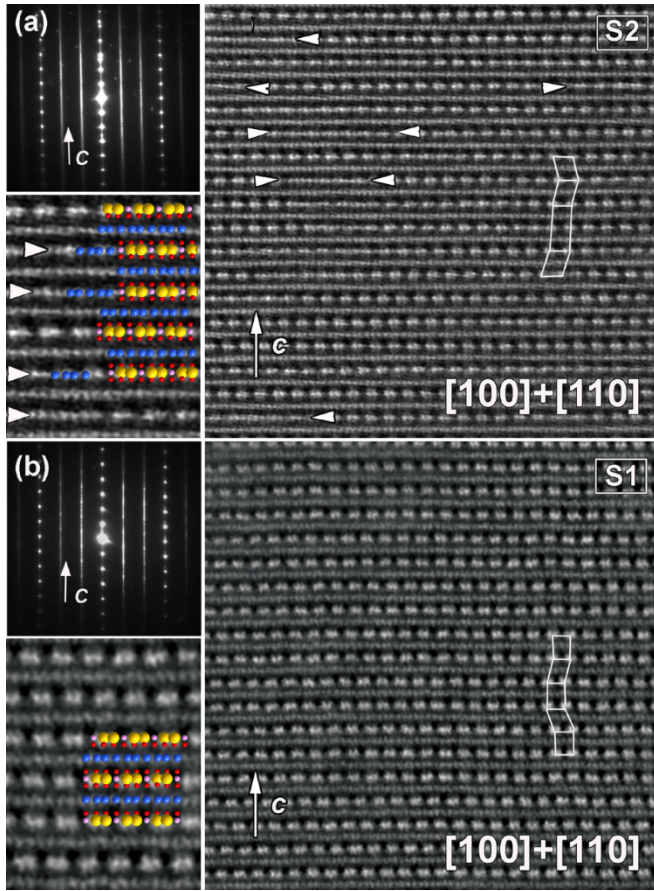


Figure 5-4: Electron diffraction and HAADF-STEM images of dirty ALIO, as originally published in ref [4]. The crystallographic structure is overlaid for clarity. Yellow = Iridium, Blue = Silver, Red = Oxygen. (a) images of sample S2, which contains rows of Ag defects. Defects are rows of bright spots and are highlighted with arrows. Ag defects exist solely in the kитаev planes. (b) Images of sample S1, which does not contain Ag defects. Additionally, both samples contain "zig-zag" stacking faults, similar to Cu_2IrO_3 . These faults are highlighted in the smaller right-hand corner STEM images.

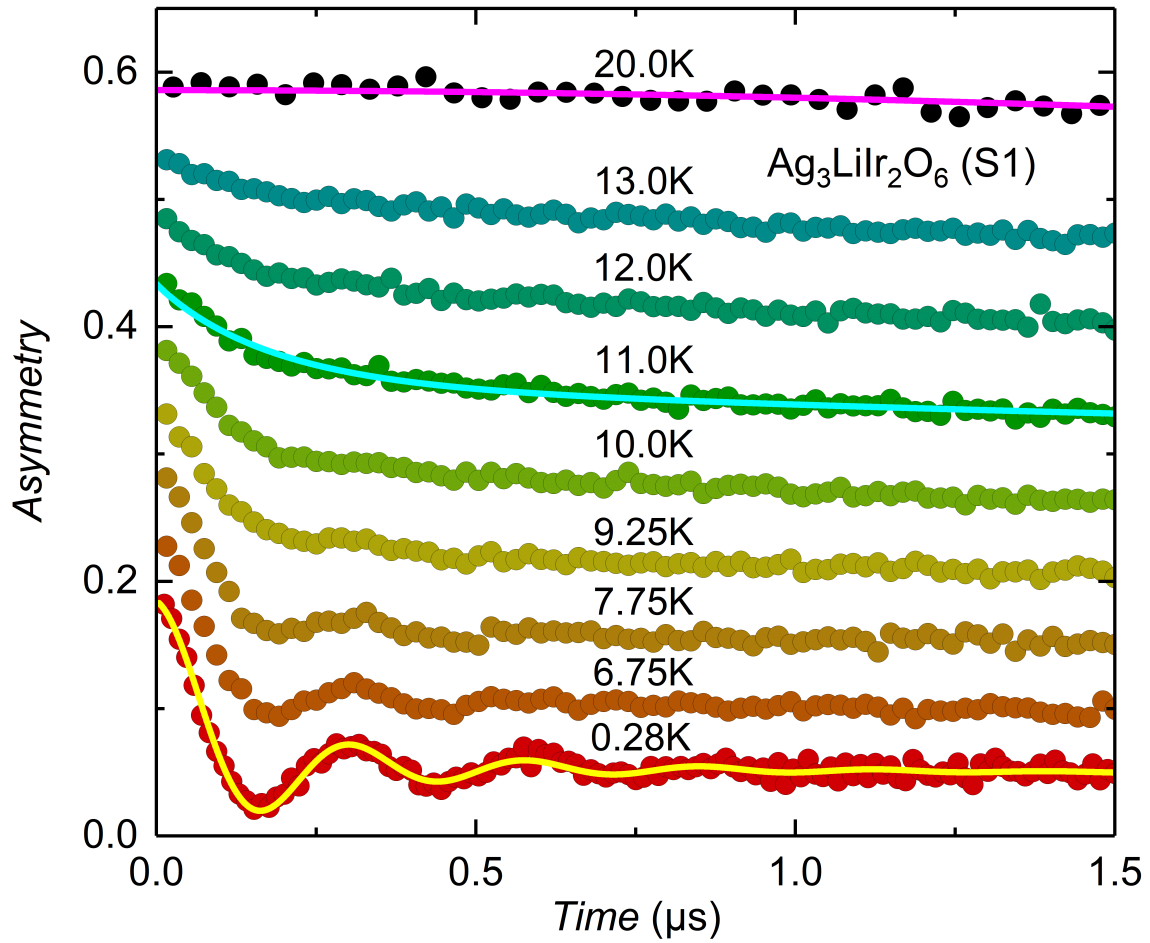


Figure 5-5: Asymmetry plotted as a function of time for short time-scales, as originally presented in Ref. [4] for ALIO sample S1. Curves are vertically offset by a 0.05 for clarity; the initial asymmetry remains constant for all curves. Fits for 0.28 K, 11 K, and 20 K, are shown in yellow, cyan, and purple, respectively.

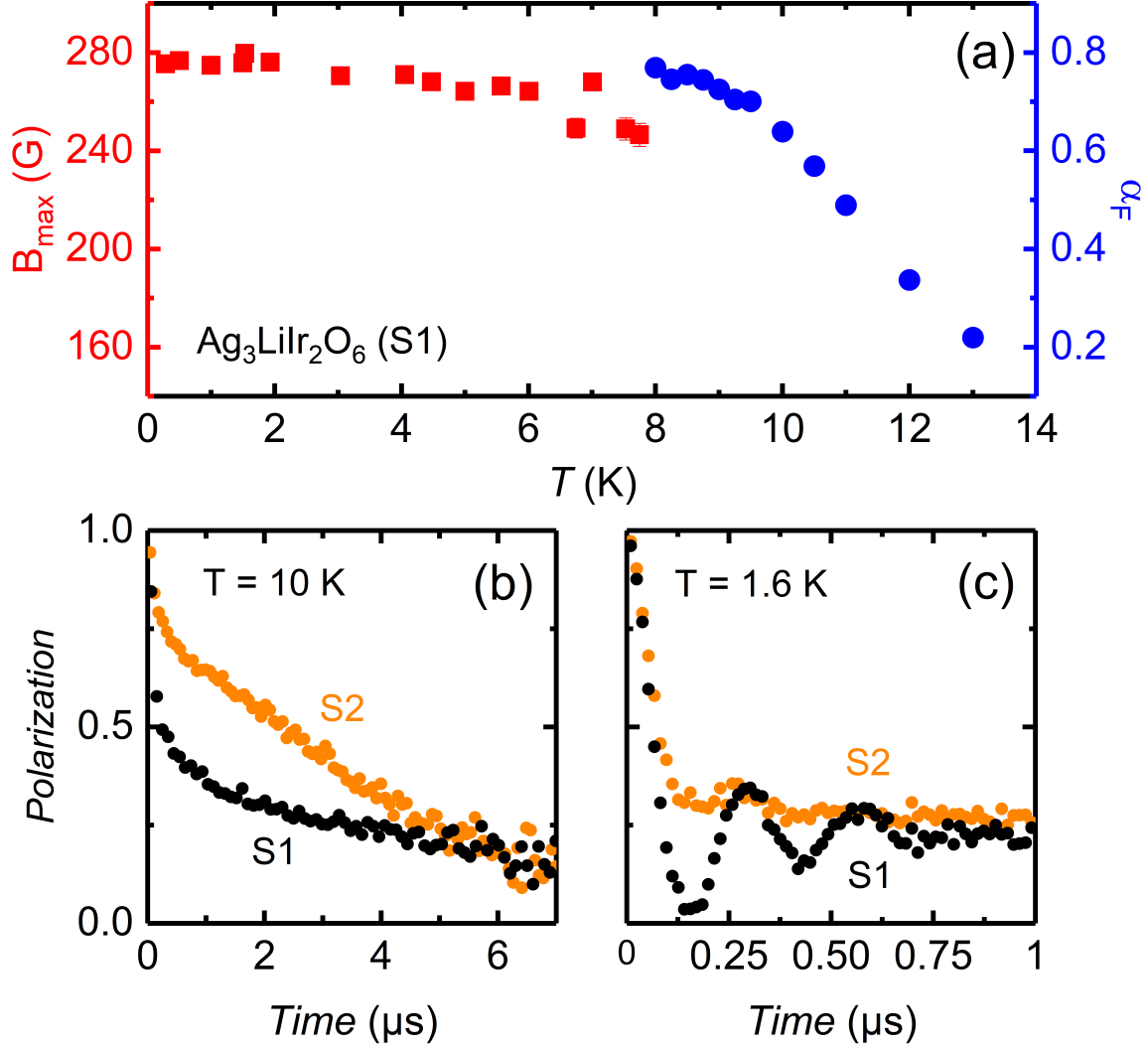


Figure 5-6: μSR fit parameters and data as originally published in ref [4]. (a) B_{\max} and α_f plotted as a function of temperature. B_{\max} is, as expected for an incommensurate magnet, nearly temperature independent until near the transition. Near the transition, the asymmetry fraction becomes too small to fit and we instead plot α_f . (b) Zero-field polarization spectra of S1 and S2 at 10 K. Sample S1 has a noticeably stronger depolarization than S2 at 10 K. (c) Zero-field polarization spectra of S1 and S2 at 1.6 K. Sample S1 has clear Bessel oscillations indicating incommensurate magnetic order. The anomalous peaks in the spectra of S2 line up well with the peaks of S1, suggesting that S2 also undergoes the same incommensurate LRO transition, but with additional magnetic disorder that suppresses the oscillations.

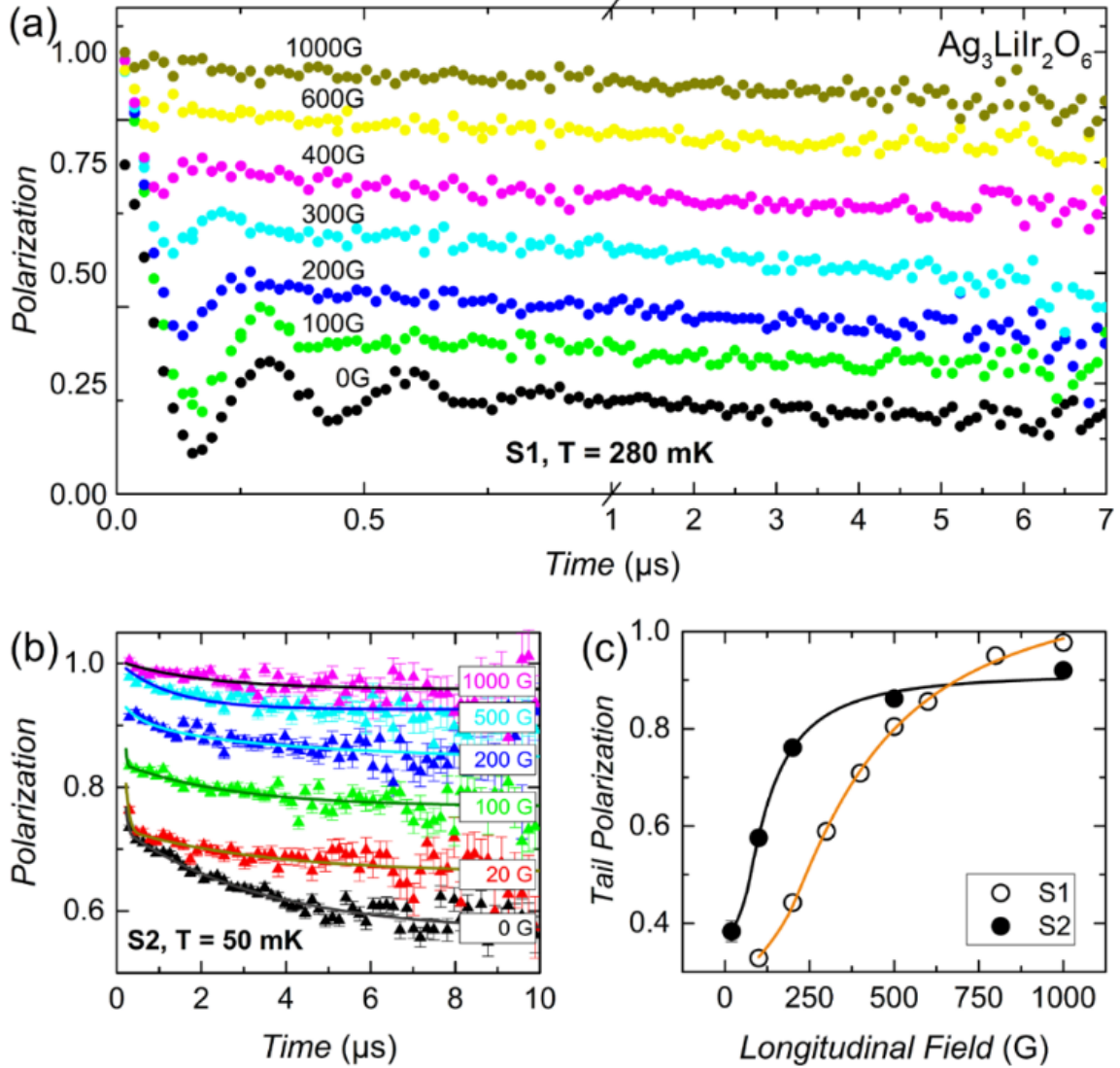


Figure 5-7: ALIO Longitudinal Field (LF) μ SR data as originally published in ref [4]. (a) LF polarization spectra of the "clean" sample S1 measured at 208 mK. The x -axis is expanded below 1 μ s to reveal oscillations. The oscillations are decoupled from the polarization by 1000 Oe, a weak exponential depolarization is seen at long times for all applied fields. (b) LF polarization spectra of the "dirty" sample S2 measured at 50 mK. The LF spectra for S2 are qualitatively similar to S1, though a weak exponential decay is not observed. The data in (a) and (b) were collected at PSI and ISIS, respectively. (c) The field dependence of the long-time tail, plotted as a fraction of the total polarization against applied fields. The lines are guides to the eye. From this figure we estimate $B_{\text{int}} = 263$ G in S1 and $B_{\text{int}} = 113$ G in S2.

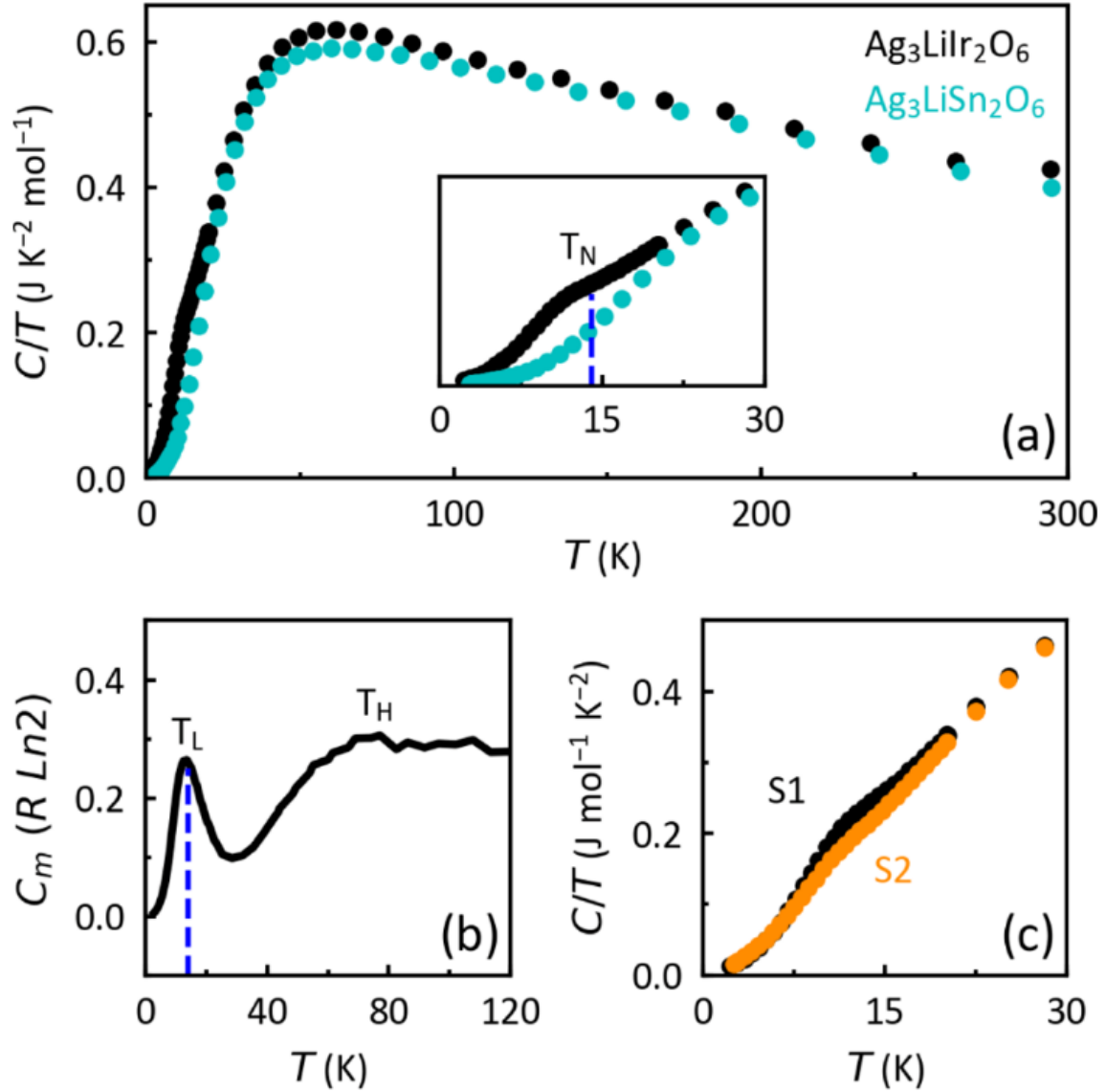


Figure 5-8: (a) Specific heat C/T of $\text{Ag}_3\text{LiIr}_2\text{O}_6$ between 2 K and 300 K. The non-magnetic analogue, $\text{Ag}_3\text{LiSn}_2\text{O}_6$ is plotted for comparison. (b) Magnetic specific heat C_m of ALIO plotted 0 K to 120 K. We see two peaks, a broad peak at T_H followed by a narrow peak at T_L . This can be interpreted as the double entropy release expected for Kitaev Magnets. (c) A comparison of the T_L peaks in C/T between samples S1 and S2. Full details can be found in our original publication in ref [4].

Chapter 6

The Kagome Metal KV_3Sb_5 : Novel Electronic States Disguised as Frustrated Magnetism

Key Publications

Absence of local moments in the kagome metal KV_3Sb_5 as determined by muon spin spectroscopy
J. Condens. Matter Phys., May 2021.

Superconductivity in the Z_2 kagome metal KV_3Sb_5
Phys. Rev. Mat., March 2021.

6.1 Introduction

In this chapter we review our experiments on the metallic kagome lattice, KV_3Sb_5 . The kagome lattice is one of the two common 2D-geometries for purely geometric spin-frustration [1]–[3], the other being the triangular lattice. The kagome lattice consists of corner-sharing triangles with a coordination number of four, while the triangular lattice has a coordination number of six. This reduction in coordination number enhances the effects of quantum fluctuations and increases the ground-state

degeneracy of the lattice, which in turn makes the kagome lattice inherently more frustrated than the triangular lattice [4]–[7].

The importance of the coordination number is seen in the isotropic Heisenberg AFM model. Theoretical calculations show that the Heisenberg AFM model magnetically orders on the triangular lattice [8] but not the kagome lattice [9]. In the literature, the most promising and important 2D QSL candidates tend to be kagome systems. For example, one of the most important frustrated materials is Herbertsmithite [4], [10] which is a kagome system.

On the other hand, most frustrated kagome systems have been insulators. This is natural, as insulating phases, conventional or otherwise, are more amenable than metals to supporting localized moments due to the requisite localization of valence electrons. But the crystallographic structure of the kagome net gives rise to unconventional band structures which, in the metallic phase, allow for unusual electronic correlations [11]. For example, density functional theory, density matrix renormalization group, Monte Carlo, and other numerical theories have predicted superconductivity, topological states with 2D Chern Gaps, Weyl Semimetals, and, of course, QSL phases [12].

Our collaborators at the Wilson lab synthesized the family of metallic kagome lattices (AV_3Sb_5 , $A=K, Rb, Cs$) which they predicted to host antiferromagnetic spin-1/2 moments [13]. These lattices consist of perfect kagome nets of vanadium intercalated by layers of alkali atoms ($A=K, Rb, Cs$) and studded with antimony (see figure 6-1). Simple electron counting arguments suggest that the vanadium ions are V^{4+} , which is $S = 1/2$ (4s1 orbital). Initial bulk characterization measurements of the susceptibility χ and the specific heat C_p/T yielded a small effective moment $\mu_{\text{eff}} \sim 0.22 \mu_B$ and a Curie-Weiss temperature of $\theta_{\text{CW}} = -47 \text{ K}$ and failed to pick out any obvious magnetic transitions¹ down to dilution fridge temperatures ($T \sim 0.25 \text{ K}$) [13].

Density functional theory calculations presented in the same paper suggest that the Fermi-energy, ϵ_f , was near several Dirac cones, with a large number of Dirac points

¹In all three systems, a field-independent anomaly is observed in both χ and C_p/T . It has since been shown to be to be a charge density wave.

overall. Subsequent investigations by other groups discovered the presence of a so-called "Gigantic Anomalous Hall Effect," (GAHE) [14]–[16] which generally relies on the time-reversal symmetry breaking properties of localized magnetic moments [12].

In the following sections we describe μ SR [17] and AC Magnetic susceptibility measurements on KV_3Sb_5 [18] which show that KV_3Sb_5 lacks localized electronic moments at all temperatures and instead undergoes a superconducting transition ($T_{SC} = 1.1$ K) with near 100% volume fraction in higher quality single-crystal samples. This is despite the simple structure and initial DFT calculations which suggested spin one-half V^{4+} ions, and the occurrence of the GAHE. Instead, in AV_3Sb_5 family a charge density wave (CDW) onsets between 80 K to 110 K, and this CDW competes with a low-temperature superconducting state in all three systems [19]–[21]. A recent study has proposed that the magnetic properties arise from orbital charge currents which circulate about the kagome net [22]. μ SR measurements are uniquely sensitive to this phase and are consistent with this interpretation.

6.2 Characterization

KV_3Sb_5 was first synthesized and characterized by Wilson group of Santa Barbara and collaborators for crystallographic structure and bulk magnetism [13]. X-ray refinement yielded a hexagonal $P6/mmm$ structure consisting of V-Sb slabs separated by K cations, as shown in figure 5-1. The kagome lattice of V is structurally perfect with no distortions and full site occupancy, within experimental error. Transmission electron microscopy (TEM) similarly showed high quality kagome structures with no obvious disorder or imperfections.

Density functional theory was performed to determine the electronic structure of KV_3Sb_5 . DFT calculations show that KV_3Sb_5 is metallic and that the fermi energy lies close to several Dirac points. Further DFT calculations showed that there is little to no charge sharing between the K and V-Sb layers, suggesting that the 2D layers are electrostatically bonded (i.e. Van der waals bonding).

DC Magnetic susceptibility measurements showed two regions of paramagnetic

behavior separated by a peak at 80 K. Curie-Wiess fits above 80 K yield a Curie-Wiess temperature of $T_{CW} = -47.2$ K and an oddly small effective moment of $0.22 \mu_B$. Below 80 K χ increases dramatically in a paramagnet-like fashion down to ~ 1.8 K.

Neutron diffraction measurements showed a lack of magnetic ordering peaks at 110 K and 1.8 K to within the experimental resolution of $0.5 \mu_B/\text{atom}$. Diffuse scattering observed, which would indicate short-range correlations, was also not observed.

Additionally, specific heat and resistivity measurements were taken. A full description of the characterization of KV_3Sb_5 can be found in ref [13].

6.3 Experimental - μ SR

KV_3Sb_5 samples for μ SR were synthesized by Brenden R. Ortiz of Prof. Wilson's group at the University of Santa Barbara. The material was synthesized as powder which was pressed into a large disk measuring 3 mm in thickness and 10 mm in diameter. The sample integrity was then verified using X-ray diffraction before being sealed in quartz tubes under Argon; sample handling was performed mostly inside Ar/He hoods with atmospheric exposure lasting for several minutes total. The sample was measured at the Paul Scherrer Institute (PSI) using the general purpose surface-muon spectrometer (GPS) and a gas-flow cryostat.

The large sample was paired with a gas-flow cryostat in GPS to maximize the signal and minimize the background. The gas-flow cryostat in GPS uses a pronged sample holder and a continuous flow of cooled ^4He gas in order to achieve excellent thermalization with minimal mounting material between the range of 1.6 K and 110 K [23]. Our background was measured to be approximately 7.1% of the total asymmetry.

μ SR measurements were performed using longitudinal spin implantation orientation in order to maximize the signal strength for individual measurements, which further increased the quality of our measured data. The sample was first measured in zero-field conditions (ZF) at several points between 1.6 K and 110 K in order to check for spontaneous magnetic order. Longitudinal field measurements were then

performed at 1.6 K in order to discriminate between dynamical depolarization and static depolarization. Finally, we took a detailed set of measurements between 1.6 K and 110 K under 100 Oe Transverse Field (TF100) conditions.

The zero-field spectra were fit to a static Gaussian Kubo-Toyabe (GKT) function (see chapter 3) plus a small background term:

$$A_0 P_{ZF}(t) = A_0 (1 - f_{BG}) \text{GKT}(\sigma_{ZF}, t) + f_{BG} \quad (6.3.1)$$

Here A_0 is an experimental parameter known as the initial asymmetry. $A_0 \cong 0.26$ which is the expected maximum asymmetry for GPS. $f_{BG} = 0.071$ is the aforementioned signal background of 7.1%. The longitudinal field spectra were calculated as a field dependent GKT in 25 Oe, using the zero-field fit parameters held constant.

The transverse field measurements were fit to:

$$A_0 P_{TF}(t) = A_0 (1 - f_{BG}) \left\{ \cos(\gamma_\mu B_{loc} t) \exp\left(-\frac{1}{2}(\sigma_{TF} t)^2\right) \right\} + f_{BG} \cos(\gamma_\mu B_{loc} t) \quad (6.3.2)$$

Here $\gamma_\mu B_{loc}$ is the Larmor precession angular frequency of the Muon due to the application of an external transverse field. For reference, $B_{loc} \cong B_{TF} = 100$ Oe, and $\gamma_\mu B_{loc} \cong 8.52$ rad MHz.

6.4 Results - μ SR Measurements

Figure 6-2 shows the zero-field spectra [17]. The zero-field spectra show a weak depolarization that changes little between 110 K and 1.6 K and fits to a rate of roughly $\sigma \sim 0.2 \mu\text{s}^{-1}$. For a Gaussian distribution, this gives a characteristic internal field strength of $\Delta \sim \sigma/\gamma_\mu \sim 2.4$ Oe, which is typical of fields originating from nuclear dipole moments, not localized spin 1/2 moments. The inset of figure 6-3 (inset) shows that the depolarization is near-fully decoupled by a weak longitudinal field of $H = 10\sigma_{ZF}/\gamma_\mu \sim 25$ Oe which demonstrates that the magnetism observed by μ SR is static on the muon time scale [24], [25]. For perspective, a moderate fluctuation rate of (10 MHz–100 MHz) would require 25 Oe–2.500 Oe to achieve the same amount of

decoupling [24], [25].

High-spin nuclei such as vanadium or antimony can generate internal fields of up to several Oe in size and easily yield depolarization rates near $0.2 \mu\text{s}^{-1}$. Nuclear motions are virtually static on the time-scale of the muon, so nuclear depolarization is normally temperature independent and static.

Transverse field measurements (figure 6-3 Inset) are sensitive to small changes in the local field distribution. This, combined with the excellent data quality, allowed us to capture a weak temperature dependence of σ , accounting for a total change of $0.04 \mu\text{s}^{-1}$ between 110 K and 1.6 K (figure 6-3). This type of temperature dependence is not typical of nuclear depolarization, and suggests a weak non-nuclear contribution to the internal field distribution may exist. This will be elaborated on in the discussion section.

6.5 Results - μSR Calculations

The lack of electronic magnetism in KV_3Sb_5 surprising given that the prior bulk-characterization shows that KV_3Sb_5 is a weak paramagnet. In this section I perform several estimations of the muon depolarization rate to rule out the presence of localized electronic moments in KV_3Sb_5 .

It is possible to calculate the expected depolarization rate for a given system provided one knows the stopping site of the muon. In metals, the muon will usually stop at an electrostatic minimum in the crystallographic unit cell, which is usually a highly symmetry interstitial site.² Calculating the stopping accurately usually requires specialized DFT methods. This is not trivial because KV_3Sb_5 hosts a charge density wave [20] and the muon stopping site is dictated by electrostatics. Instead, we provide an estimation of the depolarization rate by assuming the muon stops at interstitial sites which minimize or maximize the depolarization rate.

I performed calculations of the depolarization rate for several basic models in order

²Strictly speaking, this often applies to insulating systems as well, but more care and nuance is required due to the formation of Muonium or other bound states. Additionally, there are special exceptions for metallic systems and bad metals, such as in Oxides, that we do not discuss here.

to confirm that the depolarization is primarily due to nuclear magnetic moments. If the stopping site of the muon is known we can calculate the depolarization rate due to nuclear moment using the following formula from Ref. [24] [24, p. 150]:

$$\sigma_{ZF, nuc}^2 = \frac{2}{\gamma_\mu^2} \sum_{i=1}^{N_{ns}} \left(\frac{\gamma_i \hbar}{r_i^3} \right)^2 \frac{I_i (I_i + 1)}{3} \quad (6.5.1)$$

Here the sum is over all the nuclei i in the lattice, starting with the nearest neighbors. I_i is the nuclear spin quantum number. r_i is the distance between the muon site and a given nuclear spin. The only unknown parameter in this equation r_i , which depends only on the stopping site and crystal-structure. Therefore equation (6.5.1) is temperature and field independent. I estimate the zero-field nuclear depolarization rate to be $0.13 \mu\text{s}^{-1} < \sigma_{ZF, nuc} < 0.56 \mu\text{s}^{-1}$.³ The exact details on how this estimation was performed can be found in our original paper [17].

The transverse field depolarization rate σ_{TF} can be related to the zero-field depolarization rate using

$$\begin{aligned} \sigma_{TF, nuc} &= \sqrt{2/5} \sigma_{ZF, nuc} \sim 0.63 \sigma_{ZF, nuc} \\ &\text{for } B_{TF} \gg \sigma_{ZF}/\gamma_\mu \end{aligned} \quad (6.5.2)$$

where γ_μ is the muon gyromagnetic ratio. Plotting σ_{TF} together with σ_{ZF} (figure 6-3) shows that σ_{TF} does not satisfy equation 6.5, though σ_{TF} is still somewhat smaller than σ_{ZF} and roughly proportional to σ_{ZF} .

Now we estimate the expected depolarization assuming local electronic moments associated with V^{4+} ions. In our original paper we estimated the effective magnetic moment V^{4+} in KV_3Sb_5 to be $\mu_{\text{eff}} \sim 0.22 \mu_B$ [13]. Here we use the following equation:⁴

³The lower-end of the depolarization rate is calculated by placing the muon at an interstitial site in the K planes. This minimizes σ relative to the other interstitial sites in the lattice. The maximum bound was found by calculating σ at several interstitial near the vanadium lattices.

⁴Equation 6.5.3 is obtained from equation 6.5—which is applicable to both nuclear and electronic spins—and identifying $\mu_{\text{eff}} \cong \gamma_i \hbar J_i (J_i + 1)$, where J_i is the total angular quantum number of moment i .

$$\sigma_{ZF, nuc}^2 = \frac{2}{3\gamma_\mu^2} \sum_{i=1}^{N_{ns}} \left(\frac{\mu_{\text{eff}}}{r_i^3} \right)^2 \quad (6.5.3)$$

Given the vast difference between nuclear and electronic moments, we obtain an estimate of $2.5 \mu\text{s}^{-1} < \sigma_{ZF} < 25 \mu\text{s}^{-1}$ for the expected electronic depolarization. This is, at minimum, an order of magnitude larger than what we observed.

One possibility is that the V^{4+} ions are non-magnetic, and instead we are observing magnetic impurities in our system. Such dilute impurities could easily give rise to the Curie-Wiess signal seen AC magnetic susceptibility (AC χ) [18]. Depolarization due to dilute magnetic impurities does not depend on the muon stopping site. It only depends on the size of the impurity moments, and the concentration of impurities. The dilute impurity depolarization rate is

$$\lambda_{ZF} = 4.54 \gamma_\mu \rho_{V, \text{imp}} g \mu_B |m| \quad (6.5.4)$$

The impurity volume density is $\rho_{V, \text{imp}}$ and the effective impurity moment is $\mu_{\text{eff}} = g \mu_B |m|$. If we assume nonmagnetic V^{4+} and dilute $S = \frac{1}{2}$ impurities—as we did in our original publication—we get an impurity density of roughly 1.5% and a characteristic depolarization rate of $\lambda_{ZF} \sim 0.3 \mu\text{s}^{-1}$.

The dilute impurity model gives a reasonable depolarization rate, but still fails because it gives the wrong functional dependence for the spectra; dilute impurities create a Lorentzian internal field distribution which depolarizes exponentially as $P(t) \sim \exp(-\lambda t)$ [24], [25]. A highly-dilute impurity model with a smaller μ_{eff} or volume density could possibly explain the weak temperature dependence seen in figure 6-3, but that would then fail to be consistent with our estimations from our magnetic susceptibility data. Such a Gaussian+Lorentzian model also does not provide an adequate fit to our data. We found that the functional model that best described our temperature dependent data in both zero-field and transverse field was a pure Gaussian mode.⁵

⁵By "pure Gaussian" we mean the set of polarization functions corresponding to the muon probing a Gaussian local-field distribution, which generically corresponds to densely packed nuclear or electronic moments. See chapter for details.

Finally, we can consider the possibility of rapidly fluctuating V^{4+} moments. Since KV_3Sb_5 was expected to be frustrated, we would expect spin fluctuations down to the lowest temperatures in the ideal case. Rapid spin fluctuations reduce the depolarization rate through temporal averaging of the field distribution. In the rapid fluctuation limit, the depolarization rate is expected to vary as [24], [25]:

$$\lambda_\nu \propto \frac{\lambda_0}{\nu} \text{ as } \nu \rightarrow \infty \quad (6.5.5)$$

where ν is the characteristic fluctuation rate of the system and λ_0 is the static depolarization rate when $\nu = 0$. This gives a minimum required fluctuation rate of 2.5 GHz. This is not possible; this would place the system into the motional narrowing limit of fluctuations which would drastically weaken the field dependence of the LF spectra (figure 6-2 inset), as well as change the depolarization to an exponential curve [24].

These calculations show that the only conventional source of depolarization in KV_3Sb_5 are nuclear dipole moments. Densely packed electronic moments, on vanadium or otherwise, would provide too strong of depolarization to be consistent with the weak depolarization we observe. Dilute magnetic impurities or rapid spin fluctuations would yield an exponential depolarization instead of a Gaussian depolarization. But: a simple nuclear dipole model does not satisfactorily explain the weak temperature dependence of σ , nor why σ_{TF} fails to follow equation 6.5.3. This will be discussed shortly.

6.6 Experimental –AC Susceptibility

Following our μ SR measurements the Wilson group synthesized high-quality single crystal samples of KV_3Sb_5 , which showed possible signs of superconductivity in low temperature specific heat measurements. Therefore, we performed AC susceptibility measurements in our ^3He fridge in order to search for a superconducting transition in KV_3Sb_5 .

AC magnetic susceptibility measurements were performed on single-crystal sam-

ples of KV_3Sb_5 synthesized using improved techniques following the μSR experiment [18]. The sample was a thin, roughly ovular shape measuring $2.5\text{ mm} \times 2.4\text{ mm} \times 0.22\text{ mm}$ and with mass 1.50 mg. The measurements were performed using a hand-made coil susceptometer placed inside a Janis cryogenic He3 refrigerator and driven using an SR830 lock-in amplifier. The excitation field was approximately $0.1\text{ Oe}_{\text{rms}}$, aligned with the crystallographic \hat{c} -axis, and driven at a frequency of 711.4 Hz. The temperature range was between roughly 300 mK and 3.5 K. The data was then calibrated against AC susceptibility measurements performed in a Quantum Design MPMS3 system which measures ACX between 1.8 K to room temperature. In order to calculate χ_V , which yields the superconducting volume fraction, we approximated the samples as cylindrical volumes and corrected for the demagnetization factor.

6.7 Results – AC Susceptibility

Figure 6-4d shows the AC magnetic susceptibility (ACX) diagram as originally published, [18] which clearly shows a superconducting transition at $T_C \approx 1\text{ K}$. This was the first observation of superconductivity in KV_3Sb_5 , and we observed a nearly textbook transition. The superconducting volume is nearly 100 %, given the nearly ideal diamagnetic susceptibility of -1 .⁶ The sharp transition indicates a high-quality sample with few impurities. Complementary measurements were subsequently performed by Wilson et al using resistivity and specific heat (figures 5-4e,f), which corroborate our data and confirm a type-II superconductor.

Figures 5-4a-c show the higher temperature DC susceptibility, resistivity, and heat capacity measurements performed by our collaborators. Resistivity and heat capacity show a small anomaly in ZF at 78 K. DC susceptibility at 1 T shows a larger anomaly at 78 K below which the susceptibility increases rapidly with a Curie-Wiess like behavior. The nature of the 78 K structure in single crystals was unclear when we

⁶The observant reader may notice that obtain $\chi'_V \sim -1.1$, which would indicate beyond perfect diamagnetism. This is a systematic error resulting from sample being a thin-cylinder placed lengthwise to the field. As the sample becomes infinitely thin along the field axis, and as $\chi'_V \rightarrow -1$, the observed susceptibility diverges due to demagnetization fields and the correction for the intrinsic susceptibility becomes extremely sensitive to small errors.

originally published our results, but this has since been shown to be a CDW transition that coexists with the superconducting ground state.

6.8 Discussion

Traditional electron counting arguments tell us that the kagome lattice in KV_3Sb_5 should consist of V^{4+} ions with $S = 1/2$. The valence shell is a single $4s1$ orbital; it would be unlikely that common crystal field splitting would render V^{4+} nonmagnetic. On the other hand, electron counting is merely a rough rule of thumb, and there are many factors which could force V into a non-magnetic state. But bulk measurements showed what appears to be a frustrated antiferromagnet, with a Curie-Weiss Temperature of $\theta_{\text{CW}} = -47.2 \text{ K}$ and an effective moment of $\mu_{\text{eff}} \sim 0.22 \mu_{\text{B}}$. Moreover, the giant anomalous hall effect displayed by KV_3Sb_5 requires time-reversal symmetry breaking [15]. TRSB is usually provided by localized electronic moments. Prior to our μSR measurements, all signs pointed to KV_3Sb_5 being a highly frustrated magnet.

Instead, we saw a clear absence of local moments in KV_3Sb_5 . Our μSR spectra showed a system dominated by tiny, densely packed, magnetic moments. Under a conventional analysis, this is only attributable to nuclear dipole moments. My calculations confirmed that conventional electronic moments would be unable to provide the weak Gaussian depolarization observed in KV_3Sb_5 . The later observation of superconductivity is also at odds with conventional magnetism in KV_3Sb_5 , since superconductivity is infamously incompatible with magnetism. Magnetism can coexist with superconductivity in only a select few systems, such as FeS or FeSe [26].

Rather than being a frustrated magnet, KV_3Sb_5 appears to be a topological superconductor with a competing Charge Density Wave (CDW) state. Since our original publications, superconductivity has now been observed in all three antimonides (AV_3Sb_5 , $\text{A}=\text{K}, \text{Cs}, \text{Rb}$) between roughly $1 \sim 2 \text{ K}$ [16], [18], [27]. A CDW phase has also been observed in all three materials, with transitions between roughly 80 K to 100 K [28]. This CDW competes with the superconducting state and is tunable

via pressure. Pressure-cell measurements show that the superconducting state is re-entrant in all three materials, including KV_3Sb_5 [28]. Superconductivity and charge order appear to be intrinsically tied to the AV_3Sb_5 family.

But while the electronic properties of the AV_3Sb_5 family are interesting, the lack of magnetism does present a conceptual problem. The entire AV_3Sb_5 family exhibits GAHE and therefore there should be a source of TRSB. The most common source of TRSB in magnetic systems is magnetic ordering or magnetic skew-scattering due to the dipole moment's inherent time-reversal symmetry violation. This is why the AHE is usually due to magnetism, and most explanations for GAHE depend on unusual magnetic interactions [29]–[32]. Non-magnetic mechanisms for TRSB and driving the regular AHE or GAHE states do exist. But then why is KV_3Sb_5 clearly a paramagnet? And how do we explain the temperature dependence of σ the size of σ_{TF} in our μSR data?

In our original paper we were unable to provide a satisfactory answer. We posited several possibilities. We suggested, for example, that the V^{4+} orbitals might dimerize into non-magnetic states, and that the temperature dependence would arise from dimerized spins. But ultimately, we were forced to conclude that some details of the KV_3Sb_5 spectra were difficult to explain given the information available at the time.

A recent arXiv paper by Li Yu et al. has given a convincing account of the μSR spectra using what they call a "hidden chiral flux phase" [22]. Motivated by our results they performed a combination of μSR measurements and second harmonic generation (SHG) measurements on single crystal samples of CsV_3Sb_5 (which has a similar band-structure and similar transition temperatures to KV_3Sb_5) and have shown that, for proper orientation, single crystal CsV_3Sb_5 has approximately the same μSR temperature dependence as KV_3Sb_5 .

The theory is that the AV_3Sb_5 family hosts a pair of transitions within the CDW phase at temperatures T' and T'' that occur below the original CDW transition temperature T_{CDW} . At these $T' = 78\text{ K}$ orbital currents begin cycling along the hexagons and triangles of the kagome lattice, as shown in figure 6-5. This results in a dense matrix of magnetic dipoles which give rise to an internal dipole field distribution

that has been simulated by Yu et al (figure 6-5c-h). Yu et al call this a chiral flux phase because of the chirality it imparts onto the CDW. The transition at $T'' = 30$ K is a long-range ordering transition of these dipole currents along the c -axis.

Figure 6-6 shows the normalized gaussian depolarization rate for single crystal samples of CsV_3Sb_5 [22]. Yu's study used single crystals to measure the anisotropic σ_{ZF} as a function of the initial muon polarization parallel to the c -axis, and parallel to the ab -plane. In figure 5-7 we plot our normalized σ_{TF} for polycrystal KV_3Sb_5 against the data for CsV_3Sb_5 . We find that our polycrystal data is qualitatively similar to the data for CsV_3Sb_5 . Considering that electronic structure for both materials are similar, and that both have CDW and superconducting transitions at similar temperatures, it stands to reason that the weak temperature dependence of σ in KV_3Sb_5 is not a spurious result, but rather is reflective of a subtle chiral CDW phase in both materials. These effective dipoles are much weaker than $S = 1/2$ electronic moments, but are nonetheless densely packed. The result is a weak Gaussian depolarization with an even weaker temperature dependence. I speculate that the lack of suppression of σ_{TF} is due to the orbital currents responding in a diamagnetic fashion similar to conventional diamagnetism.

Since Yu et al's original arXiv publication, several more journal-publications have put chiral charge order theories on solid footing for all three materials [19], [20], [33], [34] in the AV_3Sb_5 family. The chiral flux phase naturally breaks time-reversal symmetry as it results in the creation of ordered and quantized magnetic moments which break time-reversal symmetry in the same exact fashion that traditional electronic moments do. This gives an obvious source of TRSB for the GAHE [28]. It also gives provides a source of dipoles for the paramagnetism seen in magnetic susceptibility. It's worth noting that the electron counting arguments used to predict the presence of V^{4+} ions with $S = 1/2$ are not valid under a CDW, so we would no longer expect to see electronic moments at the vanadium sites.

The reason that these transitions are "hidden" is that most probes are not sensitive to this transition. The magnetic aspect of the transition is extremely weak. μSR was the perfect technique for discovering these transitions which are effectively invisible

to most other techniques.

6.9 Conclusions

We have shown that the kagome metal QSL candidate KV_3Sb_5 is a non-magnetic superconductor as opposed to being magnetically frustrated system as originally thought. In particular, our μSR measurements formed the impetus for the discovery of a novel chiral charge state featuring topologically protected bulk currents about the 2D kagome lattice. It was the obvious lack of electronic magnetism on the local probe level, combined with the anomalous temperature dependence of σ and the contradictory bulk magnetic susceptibility of KV_3Sb_5 and robust superconductivity that spurred the discoveries of charge order and eventually the chiral charge currents.

AV_3Sb_5 is a topological family which features unconventional superconductivity near $1 \sim 2$ K. Superconductivity in AV_3Sb_5 competes with a CDW state near $80 \text{ K} \sim 90 \text{ K}$. The giant anomalous hall effect—which usually results from magnetic ordering—is present in all three materials, including KV_3Sb_5 . The GHAE does not occur due to electronic dipole moments as one would normally expect, but occur due to a secondary transition in the CDW where topologically protected current states form along the kagome lattice.

These currents—and the fields they produce—are weak and are either invisible to most probes, or are indistinguishable from conventional magnetism. It was our μSR measurements that provided the key experimental results to understanding KV_3Sb_5 and its siblings. Of course, that means that the AV_3Sb_5 members are longer QSL candidates due to the lack of localized V^{4+} moments. On the other hand, we have systems featuring TRSB bulk topology via novel CDW and charge states, reentrant superconductivity competing with this topology and an entire family showing the GAHE. Our papers have received over 80 citations combined since publication. We fully expect the AV_3Sb_5 systems to provide rich and interesting physics to the fields of frustrated magnetism and highly correlated systems to come.

6.10 References

- [1] J. Knolle and R. Moessner, “A Field Guide to Spin Liquids,” *Annual Review of Condensed Matter Physics*, vol. 10, no. 1, pp. 451–472, Mar. 10, 2019. DOI: 10.1146/annurev-conmatphys-031218-013401.
- [2] P. Mendels and F. Bert, “Quantum kagome frustrated antiferromagnets: One route to quantum spin liquids,” *Comptes Rendus Physique*, vol. 17, no. 3-4, pp. 455–470, Mar. 2016. DOI: 10.1016/j.crhy.2015.12.001.
- [3] A. Vasiliev, O. Volkova, E. Zvereva, and M. Markina, “Milestones of low-D quantum magnetism,” *npj Quantum Materials*, vol. 3, no. 1, p. 18, Dec. 2018. DOI: 10.1038/s41535-018-0090-7.
- [4] M. R. Norman, “Colloquium: Herbertsmithite and the search for the quantum spin liquid,” *Reviews of Modern Physics*, vol. 88, no. 4, p. 041 002, Dec. 2, 2016. DOI: 10.1103/RevModPhys.88.041002.
- [5] L. Clark and A. H. Abdeldaim, “Quantum Spin Liquids from a Materials Perspective,” *Annual Review of Materials Research*, vol. 51, no. 1, pp. 495–519, Jul. 26, 2021. DOI: 10.1146/annurev-matsci-080819-011453.
- [6] S. Sachdev, “Kagome and triangular-lattice Heisenberg antiferromagnets: Ordering from quantum fluctuations and quantum-disordered ground states with unconfined bosonic spinons,” *Physical Review B*, vol. 45, no. 21, pp. 12 377–12 396, Jun. 1, 1992. DOI: 10.1103/PhysRevB.45.12377.
- [7] R. Moessner and A. P. Ramirez, “Geometrical frustration,” *Physics Today*, vol. 59, no. 2, pp. 24–29, Feb. 2006. DOI: 10.1063/1.2186278.
- [8] J. Reuther and R. Thomale, “Functional renormalization group for the anisotropic triangular antiferromagnet,” *Physical Review B*, vol. 83, no. 2, p. 024 402, Jan. 4, 2011. DOI: 10.1103/PhysRevB.83.024402.
- [9] P. Prelovšek, M. Gomilšek, T. Arh, and A. Zorko, “Dynamical spin correlations of the kagome antiferromagnet,” *Physical Review B*, vol. 103, no. 1, p. 014 431, Jan. 19, 2021. DOI: 10.1103/PhysRevB.103.014431.

- [10] C. Broholm, R. J. Cava, S. A. Kivelson, D. G. Nocera, M. R. Norman, and T. Senthil, “Quantum spin liquids,” *Science*, vol. 367, no. 6475, p. 0668, Jan. 17, 2020. DOI: 10.1126/science.aay0668.
- [11] H. Zhang, H. Feng, X. Xu, W. Hao, and Y. Du, “Recent Progress on 2D Kagome Magnets: Binary T_mSn_n ($T = Fe, Co, Mn$),” *Advanced Quantum Technologies*, p. 2100073, Sep. 23, 2021. DOI: 10.1002/qute.202100073.
- [12] J. Zhao, W. Wu, Y. Wang, and S. A. Yang, “Electronic correlations in the normal state of the kagome superconductor KV_3Sb_5 ,” *Physical Review B*, vol. 103, no. 24, p. L241117, Jun. 28, 2021. DOI: 10.1103/PhysRevB.103.L241117.
- [13] B. R. Ortiz, L. C. Gomes, J. R. Morey, *et al.*, “New kagome prototype materials: Discovery of kv_3sb_5 , rbv_3sb_5 , and csv_3sb_5 ,” *Physical Review Materials*, vol. 3, no. 9, p. 094407, Sep. 16, 2019. DOI: 10.1103/PhysRevMaterials.3.094407.
- [14] F. H. Yu, T. Wu, Z. Y. Wang, *et al.*, “Concurrence of anomalous Hall effect and charge density wave in a superconducting topological kagome metal,” *Physical Review B*, vol. 104, no. 4, p. L041103, Jul. 8, 2021. DOI: 10.1103/PhysRevB.104.L041103.
- [15] S.-Y. Yang, Y. Wang, B. R. Ortiz, *et al.*, “Giant, unconventional anomalous Hall effect in the metallic frustrated magnet candidate, KV_3Sb_5 ,” *Science Advances*, vol. 6, no. 31, eabb6003, Jul. 1, 2020. DOI: 10.1126/sciadv.abb6003. pmid: 32937588.
- [16] Q. Yin, Z. Tu, C. Gong, Y. Fu, S. Yan, and H. Lei, “Superconductivity and Normal-State Properties of Kagome Metal RbV_3Sb_5 Single Crystals,” vol. 38, no. 3, p. 037403, Mar. 2021. DOI: 10.1088/0256-307X/38/3/037403.
- [17] E. M. Kenney, B. R. Ortiz, C. Wang, S. D. Wilson, and M. J. Graf, “Absence of local moments in the kagome metal kv_3sb_5 as determined by muon spin spectroscopy,” *Journal of Physics: Condensed Matter*, vol. 33, no. 23, p. 235801, Jun. 9, 2021. DOI: 10.1088/1361-648X/abe8f9.

- [18] B. R. Ortiz, P. M. Sarte, E. M. Kenney, *et al.*, “Superconductivity in the \mathbb{Z}_2 kagome metal KV_3Sb_5 ,” *Physical Review Materials*, vol. 5, no. 3, p. 034801, Mar. 2, 2021. DOI: 10.1103/PhysRevMaterials.5.034801.
- [19] N. Shumiya, M. S. Hossain, J.-X. Yin, *et al.*, “Intrinsic nature of chiral charge order in the kagome superconductor RbV_3Sb_5 ,” *Physical Review B*, vol. 104, no. 3, p. 035131, Jul. 15, 2021. DOI: 10.1103/PhysRevB.104.035131.
- [20] Y.-X. Jiang, J.-X. Yin, M. M. Denner, *et al.*, “Unconventional chiral charge order in kagome superconductor KV_3Sb_5 ,” *Nature Materials*, vol. 20, no. 10, pp. 1353–1357, 10 Oct. 2021. DOI: 10.1038/s41563-021-01034-y.
- [21] E. Uykur, B. R. Ortiz, O. Iakutkina, *et al.*, “Low-energy optical properties of the nonmagnetic kagome metal CsV_3Sb_5 ,” *Physical Review B*, vol. 104, no. 4, p. 045130, Jul. 19, 2021. DOI: 10.1103/PhysRevB.104.045130.
- [22] L. Yu, C. Wang, Y. Zhang, *et al.*, “Evidence of a hidden flux phase in the topological kagome metal CsV_3Sb_5 ,” Jul. 22, 2021. arXiv: 2107.10714 [cond-mat].
- [23] A. Amato, H. Luetkens, K. Sedlak, *et al.*, “The new versatile general purpose surface-muon instrument (GPS) based on silicon photomultipliers for μSR measurements on a continuous-wave beam,” *Review of Scientific Instruments*, vol. 88, no. 9, p. 093301, Sep. 2017. DOI: 10.1063/1.4986045.
- [24] A. Le Yaouanc and P. D. De Réotier, *Muon Spin Rotation, Relaxation, and Resonance: Applications to Condensed Matter*, ser. International Series of Monographs on Physics no. 147. Oxford: Oxford University Press, 2010, 486 pp., ISBN: 978-0-19-959647-8.
- [25] S. L. Lee, S. H. Kilcoyne, and R. Cywinski, Eds., *Muon Science: Muons in Physics, Chemistry, and Materials: Proceedings of the Fifty First Scottish Universities Summer School in Physics, St. Andrews, August 1998*. Philadelphia, PA: Scottish Universities Summer School in Physics and Institute of Physics Pub, 1999, 482 pp., ISBN: 978-0-7503-0630-0.

- [26] S. K. Ghosh, M. Smidman, T. Shang, *et al.*, “Recent progress on superconductors with time-reversal symmetry breaking,” vol. 33, no. 3, p. 033 001, Oct. 2020. DOI: 10.1088/1361-648X/abaa06.
- [27] B. R. Ortiz, S. M. L. Teicher, Y. Hu, *et al.*, “CsV₃Sb₅: A \mathbb{Z}_2 Topological Kagome Metal with a Superconducting Ground State,” *Physical Review Letters*, vol. 125, no. 24, p. 247 002, Dec. 10, 2020. DOI: 10.1103/PhysRevLett.125.247002.
- [28] T. Neupert, M. M. Denner, J.-X. Yin, R. Thomale, and M. Z. Hasan, “Charge order and superconductivity in kagome materials,” *Nature Physics*, Dec. 2, 2021. DOI: 10.1038/s41567-021-01404-y.
- [29] X. Kou, Y. Fan, and K. L. Wang, “Review of Quantum Hall Trio,” *Journal of Physics and Chemistry of Solids, Spin-Orbit Coupled Materials*, vol. 128, pp. 2–23, May 1, 2019. DOI: 10.1016/j.jpcs.2017.10.016.
- [30] C.-Z. Chang and M. Li, “Quantum anomalous Hall effect in time-reversal-symmetry breaking topological insulators,” vol. 28, no. 12, p. 123 002, Mar. 2016. DOI: 10.1088/0953-8984/28/12/123002.
- [31] H. Weng, R. Yu, X. Hu, X. Dai, and Z. Fang, “Quantum anomalous Hall effect and related topological electronic states,” *Advances in Physics*, vol. 64, no. 3, pp. 227–282, May 4, 2015. DOI: 10.1080/00018732.2015.1068524.
- [32] Y. Tokura, K. Yasuda, and A. Tsukazaki, “Magnetic topological insulators,” *Nature Reviews Physics*, vol. 1, no. 2, pp. 126–143, 2 Feb. 2019. DOI: 10.1038/s42254-018-0011-5.
- [33] Z. Wang, Y.-X. Jiang, J.-X. Yin, *et al.*, “Electronic nature of chiral charge order in the kagome superconductor CsV₃Sb₅,” *Physical Review B*, vol. 104, no. 7, p. 075 148, Aug. 25, 2021. DOI: 10.1103/PhysRevB.104.075148.
- [34] H. Wakao, T. Yoshida, H. Araki, T. Mizoguchi, and Y. Hatsugai, “Higher-order topological phases in a spring-mass model on a breathing kagome lattice,” *Physical Review B*, vol. 101, no. 9, p. 094 107, Mar. 30, 2020. DOI: 10.1103/PhysRevB.101.094107.

6.11 figures

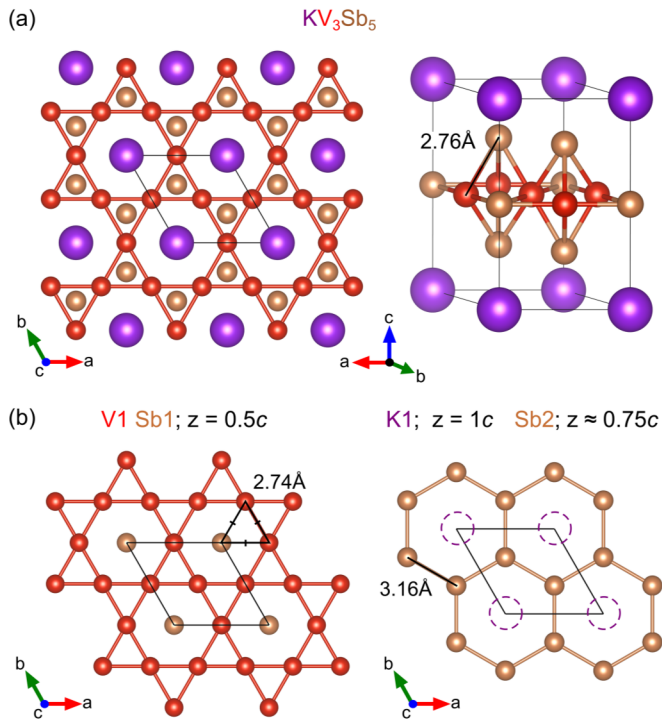


Figure 6-1: Crystal structure of KV_3Sb_5 as originally published [18]. (a) The kagome lattice of vanadium exists in the ab -plane and is intercalated with antimony. Each layer is separated by a van der waals layer of potassium. (b) By removing the vanadium we see that the in-plane antimony forms a hexagonal structure known as antimonene, due to its similarity to graphene.

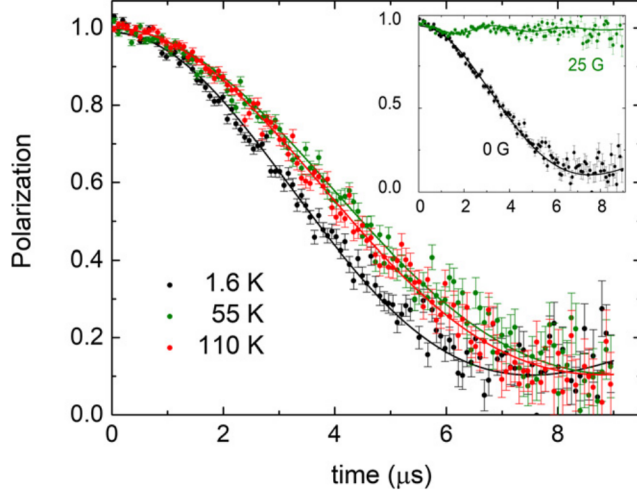


Figure 6-2: μ SR polarization spectra for KV_3Sb_5 , as published in ref [17]. (Main) Zero-field spectra fitted to a static Gaussian Kubo-Toyabe function at three temperatures. (Inset) Longitudinal-field spectra at 0 Oe and 25 Oe fitted to a longitudinal-field static Gaussian Kubo-Toyabe function.

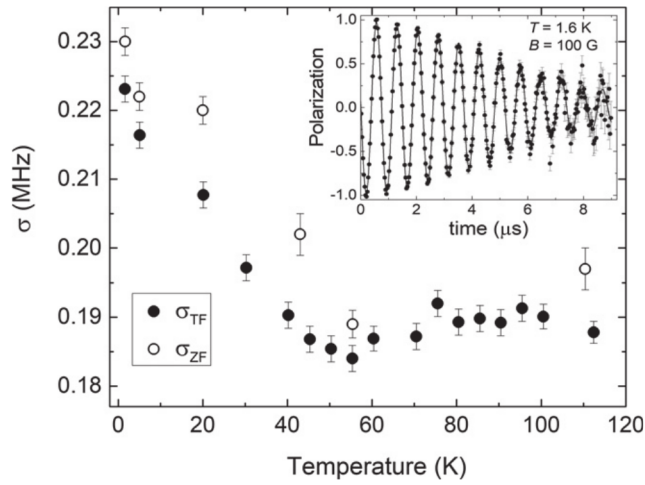


Figure 6-3: (Main) Temperature dependence of the Gaussian depolarization rate in zero-field and transverse field, as originally presented in ref [17]. Note that it is theoretically predicted that $\sigma_{TF} \approx \sqrt{2/5}\sigma_{ZF}$ when $B_{TF} \gg \sigma_{ZF}/\gamma_\mu$ and the dipole moments are static [24]. (Inset) Transverse field polarization of KV_3Sb_5 at $T = 1.6$ K, $B = 100$ Oe. Line represents fit as described in the text.

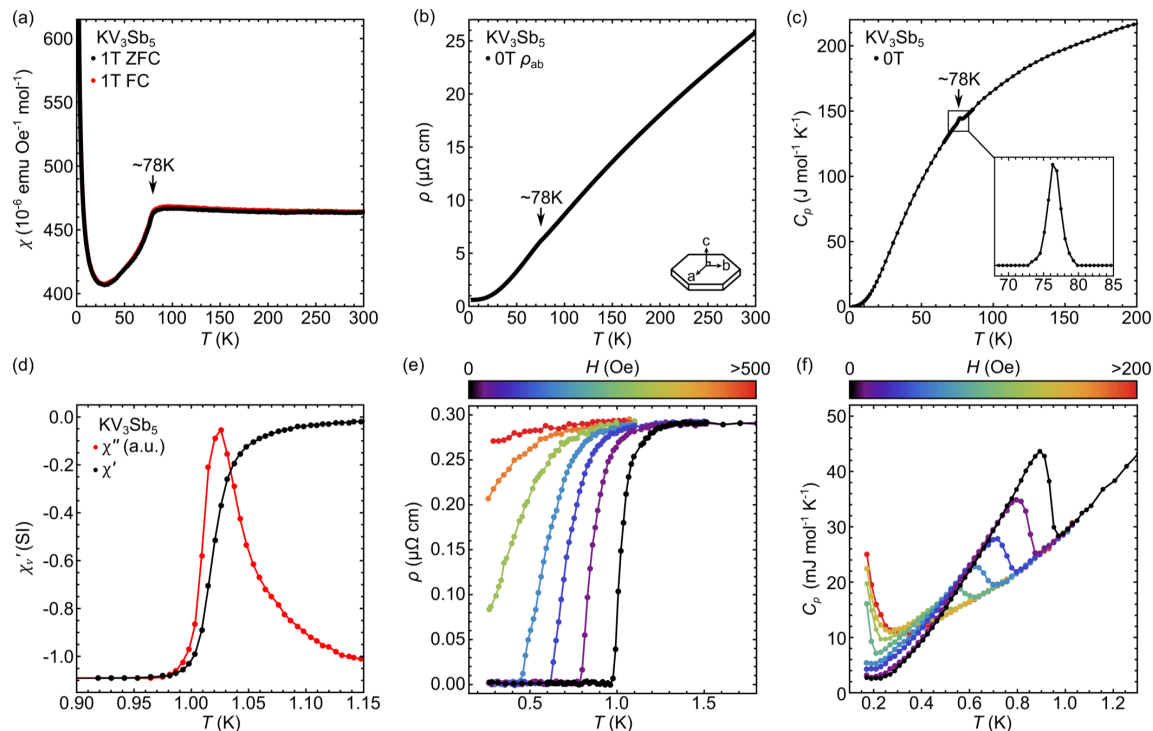


Figure 6-4: Bulk electronic measurements of KV_3Sb_5 , as we originally presented in ref [18], including the caption. **(a)–(c)** Susceptibility, electrical resistivity, and heat capacity showing behavior of stoichiometric single crystals above 2 K. All measurements show an anomaly at 78 K, coinciding with emergence of a charge density wave. Magnetization results indicate that KV_3Sb_5 is a Pauli paramagnet at high temperatures. As shown previously, the weak Curie tail at low temperature can be fit with a small concentration of impurity spins. Resistivity is low, indicating a high mobility metal. The λ -like anomaly in the heat capacity is shown, magnified, with a spline interpolation used to isolate the transition. **(d)–(f)** Susceptibility, electrical resistivity, and heat capacity measurements below 2 K highlight the onset of bulk superconductivity in KV_3Sb_5 . A well-defined Meissner state is observed in susceptibility, which coincides with the zero-resistivity state and a sharp heat-capacity anomaly.

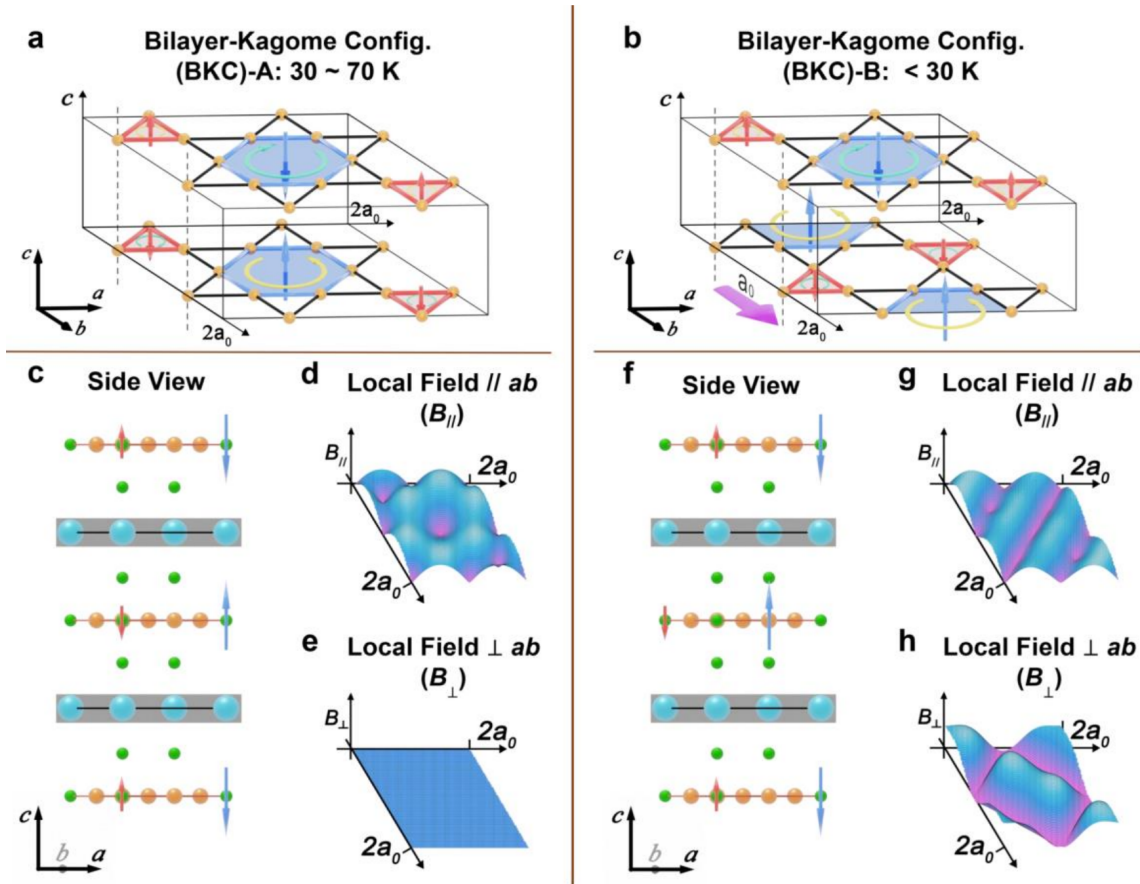


Figure 6-5: Diagrammatic representation of the orbital dipoles and local magnetic field in the kagome planes of CsV_3Sb_5 . figure is taken from Li Yu et al's paper, "Evidence of a Hidden Flux Phase in the Topological Kagome Metal CsV_3Sb_5 " [22]. (a) Schematic representation of the magnetic configuration of the vanadium kagome lattice between 30 K and 70 K . Circular arrows represent the effective orbital current loop, straight arrows represent the effective magnetic moment. (b) Schematic representation of the magnetic configuration of the vanadium kagome lattice below 30 K . (c) Side-view of the lattice diagram shown in (a), with Sb shown in green and Cs shown in blue. (d) Visualizations of the local magnetic field component parallel to the ab -plane between 30 K and 70 K . The local field in CsV_3Sb_5 has uniaxial symmetry along the c -axis. (e) Visualizations of the local magnetic field component perpendicular to the ab -plane between 30 K and 70 K . (f-h) Same as figures (c-e), but for the $T < 30$ K phase.

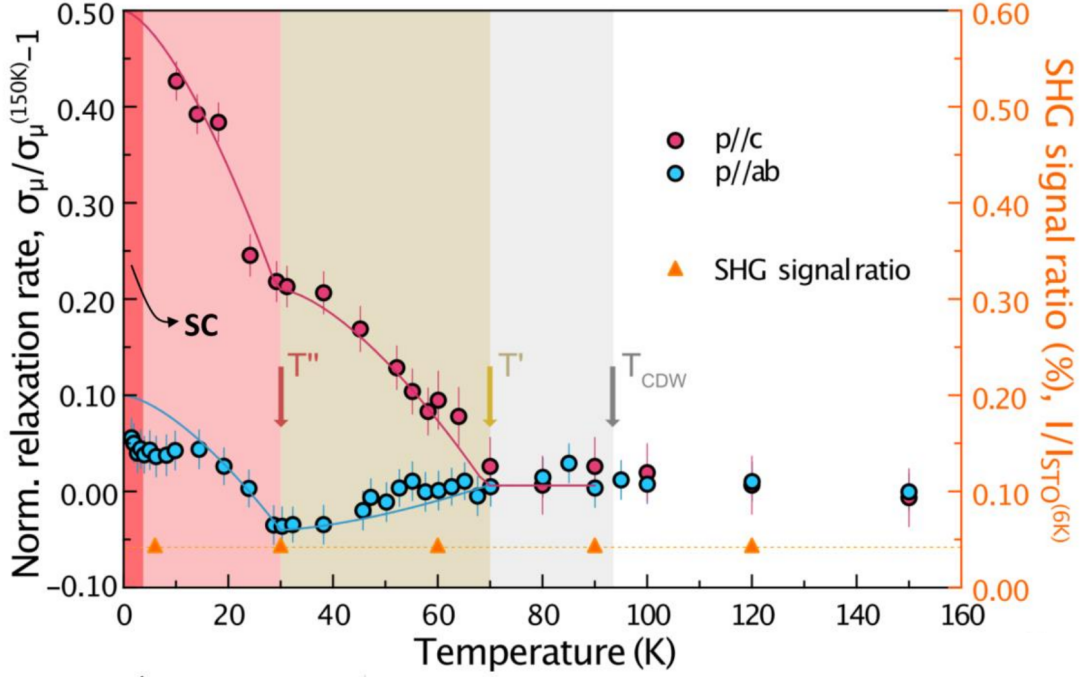


Figure 6-6: μ SR-based phase diagram for CsV_3Sb_5 . Figure is taken from Li Yu et al's paper, "Evidence of a Hidden Flux Phase in the Topological Kagome Metal CsV_3Sb_5 " [22]. Zero-field Gaussian relaxation rate σ_μ as a function of temperature. σ_μ is normalized to 150 K : $\sigma_{\text{norm}} = (\sigma_\mu - \sigma_\mu(150 \text{ K})) / (\sigma_\mu(150 \text{ K}))$. The value of $\sigma_\mu(150 \text{ K})$ is not given by Yu Et al in their paper. Red points represent the depolarization rate measured when the initial muon polarization is parallel to the crystallographic c -axis. Blue points represent the depolarization rate measured when the initial muon polarization is parallel to the crystallographic ab -plane. The orange triangles and the right-hand axis refer to second-harmonic generation measurements, details of which can be found in the original publication. Color regions correspond to the known electronic transitions of CsV_3Sb_5 . A charge density wave (CDW) sets in at $T_{\text{CDW}} \sim 95 \text{ K}$ a pair of secondary chiral transition in the CDW occur at $T' \sim 70 \text{ K}$ and $T'' \sim 30 \text{ K}$. A superconducting transition occurs at $T_{\text{SC}} = 2.5 \text{ K}$. [27]

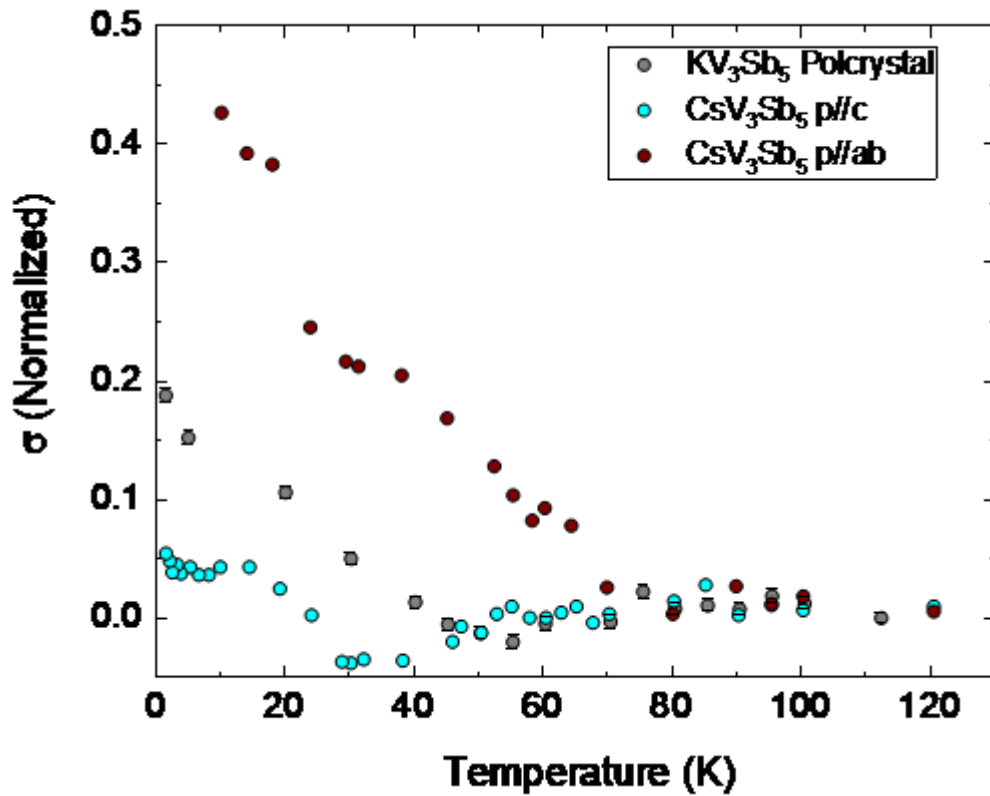


Figure 6-7: The normalized gaussian depolarization rate of polycrystal KV₃Sb₅ compared plotted with the single-crystal depolarization rates of CsV₃Sb₅ from figure 6-6. The KV₃Sb₅ data is normalized to 112 K and taken in transverse-field, while the CsV₃Sb₅ data is normalized to 150 K and taken in zero-field.

Chapter 7

Conclusions

In this thesis I have reviewed my work on several magnetically frustrated systems and contributed to the identification of their ground states.

First, I reviewed my work on NaYbO_2 and LiYbO_2 , which are three dimensional bond-frustrated magnets. NaYbO_2 is a quantum disordered magnet with a quantum critical point. It is the closest of the systems I've reviewed to being a quantum spin liquid. LiYbO_2 is a bipartite spin system undergoes incommensurate spiral order with two independent order parameters. This results in a novel "random phase bipartite incommensurate" phase. I analyse this system in the context of μSR and propose an original polarization function to describe the data.

Next, I reviewed my work on the iridates: Cu_2IrO_3 and $\text{Ag}_3\text{LiIr}_2\text{O}_6$. My μSR measurements showed that Cu_2IrO_3 has a magnetically inhomogeneous ground state. Our collaborators later found that this was due to charge state disorder in the system. My measurements on $\text{Ag}_3\text{LiIr}_2\text{O}_6$ showed that it is magnetically long-ranged ordered despite previous measurements suggesting it to be magnetically frustrated. This experiment highlights the role crystal quality can play in analyzing a QSL candidate, with disorder often masking signs of spin freezing or ordering.

Finally, I reviewed my work on KV_3Sb_5 . This was a metallic kagome system that was expected to be spin-frustrated. My μSR data showed an absence of local electronic magnetism in the sample, in defiance of bulk susceptibility showing a weak paramagnet. My AC susceptibility data also showed that KV_3Sb_5 superconducts

at 1 K. My results stimulated studies in the literature which found that the entire AV_3Sb_5 family has unusual physics, including a potential "chiral-flux phase."

The works covered in my thesis are broad and show the many possibilities of magnetism and QSL materials. Competing interactions in a system often result rich phase diagrams and novel physical phenomena. Magnetic frustration is one of the best examples of this, with there being multiple fields worth of different magnetic phenomena being generated from frustration.

This makes the search for a QSL difficult, as there are many possibilities and pitfalls one can encounter. Crystal defects can mask long-range order, charge-state disorder can introduce spin defects, and sometimes a bulk magnet might not have localized moments at all! None the less, each of these systems contains fascinating physics in their own right while also providing us with vital information that helps guide us towards synthesizing better QSL materials.